POLITECNICO DI TORINO

Master's Degree in Mechanical Engineering

Master's Degree Thesis

Modeling and Identification of an Experimental Test Bench for the study of Electrodynamic Phenomena

Supervisors

Prof. Nicola AMATI

Prof. Andrea TONOLI

Dr. Renato GALLUZZI

Dr. Eugenio TRAMACERE

Candidate

Lorenzo BOSICA

a.y. 2021/2022

Acknowledgements

I would like to express my gratitude to Professors Nicola Amati and Andrea Tonoli for involving me in this interesting, innovative and stimulating research. A dutiful thanks also to Dr. Eugenio Tramacere and Dr. Luis Castellanos for guiding and helping me in this tortuous project and, above all, for captivating and inspiring me.

A warm huge hug to all the friends who have shared this journey with me, those I have had the good fortune to meet here in Turin and those further afield that I always carry with me.

My most heartfelt thanks goes to my family for always supporting me, from the first day at elementary school up to now that I'm about to graduate in engineering. It is curious that from Atri, to L'Aquila up to Turin you continue to always be my greatest point of reference, my greatest source of inspiration.
I hope you are as proud of me as I am of you.

Sincerely, thank you
Lorenzo

Summary

The search for innovative and sustainable solutions in the field of mobility and transport has become one of the main protagonist of the last decade. In this sense, the Hyperloop concept is an interesting and emerging solution able to deliver speed and sustainability to transport people and cargo alike. Such a technology offers different advantages: high speed, low carbon emissions, weatherproof, low power consumption, low cost on long run and so on.

Despite this, from a technical point of view, some points are still open and the critical issues linked to the dynamics and the instability of the electrodynamic levitation system represent certainly a challenge for the Hyperloop technology.

In such a context, the work that has been carried out try to give a small and precious contribution to the problem. In particular, the main objective of the thesis is the modeling and the identification of an electro-mechanical device for the experimental study and the validation of theoretical models related to electrodynamic levitation phenomena.

The first part is dedicated to the description of the scale down model that simulated the vertical dynamics of the pod; the chapters that immediately follow resume and describe the multi-domain linear models used in the numerical simulation; the last part of the thesis contains all the experimental measurements. Finally, the fitting between the experimental results and numerical models have been described and a suitable observer able to work in parallel with the scale down model has been introduced.

The proposed work has been developed in the Politecnico di Torino in collaboration with the US company Hyperloop Transportation Technologies.

Table of Contents

List of Tables

List of Figures

Acronyms

BEMF

Back-electromotive force

CAN

Controller area network

CMP

Counter compare

DAC

Digital to analogue converter

DOF

Degree of freedom

EDB

Electrodynamic bearing

EDS

Electrodynamic suspension

EMS

Electromagnetic suspension

FEM

Finite element method

FFT

Fast Fourier Transform

FRF

Frequency response function

HEMS

Hybrid electromagnetic suspension

HTT

Hyperloop Transportation Technology

MIMO

Multiple Input Multiple Ouput

PDF

Probability density function

PM

Permanent magnet

PWM

Pulse-width modulation

SCM

Superconducting magnet

SISO

Single Input Single Ouput

VC

Voice coil

Chapter 1

Introduction

The main objective of this thesis work is the numerical modelling and the experimental identification of an electro-mechanical device with permanent magnets under electrodynamic phenomena. This physical scale model has been built in order to simulate the static behaviour and the vertical dynamics of an electrodynamically suspended rigid system translating along a track made of conductive material.

The following work is not self-contained and the researches carried out do not lead to stand-alone results but, on the contrary, it can be framed in a broader project that involves the American company ***H****yperloop* ***T****ransportation* ***T****echnology* (**HTT**) and the Italian technical university *Politecnico di Torino* for the study of the stability of electrodynamic levitation-based transport systems. The theoretical interest in the subject and the pragmatic need to develop innovative transport systems in line with current trends have led to a strong cooperation between the two institutions for the search for functional engineering solutions. For this reason, the test bench mentioned above has been built in order to put the problem of instability in evidence. On the other hand, numerical models capable of representing and predicting the related static and dynamic behaviour have been developed. Since the former has been thoroughly investigated in previous researches, the following thesis is mainly focused on the latter aspect, continuously oscillating between theoretical predictions and experimental discoveries.

1.1 Literature review

Electro**d**ynamic **s**uspension (**EDS**) is nothing new in scientific literature. Advantages and drawbacks related to this magnetic levitation technique have been extensively investigated in the field of rotodynamic and, in particular, for the **e**lectro**d**ynamic **b**earings (**EDB**). Numerical models as well as experimental validations can be found in different engineering researche, so that it is possible to inform about the intrinsic nature of dynamic instability of EDBs, solutions for active damping method and reliable numerical results [1].

Recently, the global railway transportation industry is moving towards the use of electrodynamic levitation aiming at reducing propulsion energy and achieving higher cruising speed [2]. Although one might think of extending the already achieved results of rotational dynamics to their translational counterpart, actually there is a large hole on understanding and predicting the instability phenomena associated with it: a great mismatch between theoretical studies and empirical evidence on this topic can be found in literature.

Generally speaking, the basic principle of EBS is a well-established knowledge and it can be represented by resorting to different numerical approaches. It is also clear that electrodynamic levitation-based systems require stabilization since they may present some instabilities. This is because the main acting forces depend on different motion parameters and decrease exponentially with the distance from the reference track. Even if it is possible to consider only the horizontal and vertical dynamics, one can immediately realize that the lift force can't be stabilized by only the counter effect of the gravity force and that the drag force tends to decrease with translational velocity; furthermore, the coupling of vibration modes and the consequent mutual influence in terms of stability is still unexplored.

Electrodynamic suspension systems are often thought to be intrinsically stable. This can be assumed to be a valid observation if static or steady-state conditions are respected continuously. However, under the influence of no steady-state conditions, a variety of factors, including damping mechanisms incorporated into the design, can perturbates the system and lead to unstable responses. *Francis Moon* has been discussed about the different type of instabilities of maglev system in his work [3]. In particular, he demonstrated that the instability is an increasing motion from the equilibrium position that is only interrupted by some non-linearities in the system.

The lack of information about instability phenomena on EDS system is a general problem to analyse that regards different type of magnetic levitation system, from the oldest up to the newest technologies. For this purpose, *Rote and Cai* presented in their work [4]. a review of the studies about the electrodynamic instability carried out during the second half of 1900, focusing on the main results reached both for large-scale vehicles and small-scale test benches. In the first case, dynamic instability has not been detected since in all cases oscillations due to the track irregularities showed a decreasing trend with time. The only instability detected was defined of "static" type since it was observed at low speed when the guidance force is not stiff enough to prevent the roll-lateral swing motion [5]. On the other hand, in contrast with the large-scale vehicles on linear test tracks, small scale models demonstrated an intrinsically underdamped behaviour of EDS system for a wide range of track configurations and vehicle design characteristics. However, the light damping introduced in the magnetic domain is not enough to ensure stability and it is linked the joule loss of energy in the guideway conductive materials. This has been demonstrated experimentally by using simple long current loops and pendulum-based model ([6], [7]). *Zhu at al.* [8] used a direct method to quantitative estimate magnetic stiffness and damping associated to EBS by means of laboratory experiences. It is worth to observe from those experiment that damping decreased with velocity up to negative values. In the same contest, theoretical models were proposed [9]. These were able to predict the presence of a negative damping above a certain speed but without any experimental evidence. This was because of the difficulty to measure the negative intrinsic damping force in presence of other sources of damping, such as aerodynamic, mechanical structural and eddy-current dissipating phenomena. However, an important observation for scale models was the fact that the magnetic forces, that are motion dependent, caused different types of instability in EDS system: this is the case, for example, of the existence of a yaw instability induced by drag-forces [10]. In general, in all those experiments, the presence of parallel damping phenomena prevented by well understanding the condition and the characteristic of EDS instability. This was valid, in particular, for large scale model where passive mechanism were present together with large magnets and stiff and nonlinear forces that tend to stabilize the system at higher speed.

In 1999 *Post and Ryutov* introduced the concept of the Inductrack as a simpler approach to magnetic levitation [11]. According to that theory, the electrodynamic suspension became fully passive technology that would only require the definition of an appropriate array of **p**ermanent **m**agnets (**PM**). Even in this contest, a theoretical representation of the Inductrack was proposed but the dynamic instability was overlooked and superficially discussed. In one of this work [12], *Richard Post* numerically predicted the existence of a small-growing oscillations at the natural frequency of the suspended mass. However, the presence of auxiliary wheels was enough to suppress the unwanted instability. In 2002, *General Atomics* carried out some experimental tests aiming at realizing a large-scale prototype able to work in safety conditions [13]. Unfortunately, no dynamic instability phenomena were detected like most of the previous large-scale experiences. This is probably because of the large air gap reached. However, it was clear that auxiliary stabilizing mechanism would be necessary, most of them concerning active viscous dampers, servo-controllers for added lift forces and a modulation of the phase of drive coils.

In 2002, *Storset and Paden* discussed about the influence of theoretical model assumptions on magnetic damping [14]. A difference between the finite and infinite track hypothesis was considered. In particular, finite track models were lauded for being computational advantageous, but it was highlighted a wrong representation of the energy loss from eddy currents, an important aspect linked to stability properties; on the other hand, infinite track models were defined as the continuous counterpart able to take into account the dissipation of energy in the magnetic equation. Despite this aspect regards a limited region around the PM pad, it was stated to be sufficient to ensure low damping and stable mechanical behaviour as experimental predict. At the same time, some necessary methods to increase damping have been proposed. For example, it was underlined the advantages on using both passive and dynamic dampers, whose performances were briefly and qualitatively analysed.

Recently, the Hyperloop paradigm mentioned by *SpaceX* in a white paper [15] has rekindled even more interest in electrodynamic suspension and its still unsolved technical issues. This has been a source of motivation not only for railway transportation industry but also for university and team students that, thanks to the well-known *Hyperloop Pod competition*, has currently the opportunity to deal with dynamic instabilities and other engineering related troubles. An interesting example in this sense is the *OrcaPod* from *Team Hyperloop India*, described in its design by *Pradhan and Katyayan* [16].

In 2020, a systematic approach to the instability of EBS systems has been proposed by *Galluzzi et al.* [17]. Numerical simulations both for one and two degrees of freedom levitating mechanical system have been carried out. It is worth to observe that in the first case it has been demonstrated that the system is dynamically unstable with the increasing of velocity and thus in the whole range of interest. It has been reported the related root locus plot in which it is possible to appreciate the dependence of the real part of mechanical poles with translating velocity, all aspects that suggest the effectiveness of the proposed numerical model on dealing with electrodynamic suspension.
summary, different numerical models of EBS systems can be found in literature as well as some common aspects related to electrodynamic instability in most of researches. It has been underlined the presence of intrinsic low magnetic damping, the stability under steady-state conditions, the decreasing of damping with velocity, the effect of non-linearities, geometry of guideway and magnetic pad and the dimension of the prototypes on the global behaviour of the system. Despite these considerations, a mismatch between theoretical predictions and experimental evidence is still present and the nature of electrodynamic instability phenomena needs to be further investigated.

1.2 State of art

The following thesis is part of a wider project involving *Hyperloop Transportation Technology* and *Politecnico di Torino*. The starting point of all the researches carried out can be identified in the paper "*A Multi domain Approach to the Stabilization of Electrodynamic Levitation Systems*" by *Galluzzi et al.* [17].

The multi-domain integrated numerical model developed allows for the representation of the intrinsic instability typical of electrodynamic suspension. In particular, since the model proposed is linear, it allows for the root locus analysis in order to detect the presence of poles with positive real part as function of velocity. The numerical simulation summarized in the paper demonstrate the effectiveness of the approach adopted but, as the literature review can suggest, an experimental validation might be necessary. Therefore, the whole project rapidly moved toward the realization of laboratory prototypes.

In "*Design and control of an experimental test system for a linear electrodynamic levitation device*" by *Fanigliulo* [18] the project and the realization of the small-scale test bench has been summarized. It consists of a copper ring rigidly attached to on aluminum turntable that is able to rotate inducing lift and drag forces on a fixed measuring stage. The general outline of the project, the characteristics of the layout, the bearings selection and the suspension design have been well highlighted in the different chapters of the thesis work.

In July 2022, the static validation of the integrated numerical model have been demonstrated by *Bo* and *Conchin Gubernati* ([19], [20]). Experimental drag and lift forces curves as a function of different airgaps and steady-state track velocity have been compared and matched with theoretical results for different type of *Hallback* arrays and guideway conductive materials. Considerations about the control strategies and the estimation of states of the system as well as the identification of the adopted active damper can be found in these reaserches.

Considering the current state of work, the validation of the dynamic behaviour of the model proposed by *Galluzzi et al.* is the missing link of the whole project. Thus, the following thesis comes in. The results that will be developed in the next chapters describe the identification procedure of the experimental test bench, the proper tuning of the numerical model and the choose of suitable observer able to work in parallel with the physical system. Once the multi-domain approach proposed at the beginning of the project will be validated, a reliable model able to represent the intrinsic unstable nature characterizing the vertical dynamics of a capsule moving along a conductive track could be found in literature: it could be an interesting starting point for improving current railway technologies or even a simple food for thought for more complex and sophisticated theoretical approaches; furthermore, the linearity of the approach and the presence of an active damper in the test bench will allow implementing different control and stability strategy, the analyses of which have already been started in the work of *Pakštys* [21].

Finally, the key word of the whole project sustained by HTT is the stability of electrodynamic levitation-based system, that can be appreciated thanks to the experimental test bench realized by researchers teams of *Politecnico di Torino* and whose static and dynamic behaviour have been identified in the current and past thesis works and scientific papers.

1.3 Thesis outline

The main guideline of this essay follows the identification and the modelling of the experimental test bench mentioned above as well as the definition of a suitable observer that can be used to implement future active control strategies. From the numerical point of view, all the necessary codes have been developed by using MatLab® and Simulink®; from the side of experimental measurements, *Texas LaunchXL-F281379D* and *dSpace MicrolabBox* microcontrollers have been extensively used. In particular, the former was involved in the active control the electromagnetic damper of the dynamic stage; the latter has become the main protagonist of the second part of the thesis dedicated to the analysis of state observers. Each of these microcontrollers work in *C language*, so that it has been required proper add on compilers to make possible reading the code written in MatLab® and Simulink®.

Along the main path of the research, different indirect and transversal knowledge have been required as well as lot of time has been spent to solve issues mainly regarding the set-up of the measurement equipment, the communication protocol between all the device involved, the search for proper instrument dedicated to signal processing, the definition of measurement strategies, the need to avoid intrinsic nonlinearities of the devices, the use of structural analysis and, in general, the overcoming of all those obstacles necessary to achieve the real objective of the thesis.

That being stated, researches carried out are summarized and organized in the current thesis as follows. *Chapter 2* contains a brief introduction to Hyperloop and general electrodynamic transport system, focusing mainly on the description of the components of the experimental test bench, from the static to the dynamic stage; in *Chapter 3* numerical models are summarized. In particular, equations related to levitation as well as electro-mechanical systems are deeply analyzed and instability conditions are highlighted. Furthermore, some state observers are introduced and described from a theoretical point of view; *Chapter 4* is fully dedicated to experimental measurements and numerical simulations. The identification of the main unknown parameters is described up to the fitting between the Frequency Response Functions; in *Chapter 5* a comparisons between the different state observers is discussed by resorting to numerical simulations. Experimental evidence are summarized to confirm the choose of the most reliable predicting model. A brief description of an active current control aiming to impose the optimal damping to the system is introduced. Finally, *Chapter 6* closes this thesis work underlining the main results achieved and encouraging for further studies.

Chapter 2

A test bench for electrodynamic suspension

Since their invention, magnetic levitation or Maglev trains have been subject of massive experimental studies. They have been commercially available only in the early 21st century and still nowadays they are objective of researches on various aspects, from the choose of the most convenient levitation system up to the controversial issue of dynamic stability.

From the point of view of the experimental research, it is worth to say that full-scale prototypes have been proved to be not suitable for detecting magnetic levitation phenomena and, in particular, dynamic instability [4]. This is because of the presence of unwanted real non-linearities and added damping effects, for example those linked to aerodynamic friction. All these aspects make experimental measurements difficult and prevent reliable results from being achieved. For these reasons, different scale physical models have been introduced in the past years.

In this contest, the main characteristics and the general design of the experimental test bench which is realized by *Politecnico di Torino* with the collaboration of *Hyperloop Transportation Technology* [18] is described in this chapter. It is important to underline that such a configuration allows to reproduce the vertical behaviour of electrodynamic levitation-based system, without getting information about the transversal or rotational motions. Thus, only the statics or the dynamics due to lift and drag forces can be detected..

In the author's opinion, in order to better understand and appreciate the working principle and the potentialities of the test bench, it should be clear the suspension technology to which this thesis is referring. Therefore, the first paragraph contains a short account on magnetic levitation, with particular attention to trains transport system.

2.1 Magnetic levitation

Magnetic levitation has been identified as a possible solution able to improve train transportation systems by now. It was pretty early on when one of the main goals became that of increasing the cruising speed. This fact slowly led to think of different solutions with respect to wheel transport which, due to the unavoidable inertia, had always put a limit on the maximum achievable speed. Thus, the first step was the removal of wheels and the introduction of different suspension technologies, among which the magnetic levitation system has emerged as the most convenient [22]. In fact, different advantages can be achieved: the absence of mechanical contact allows the reduction of vibrations and maintenance, the guideway don't let Maglev train to be derailed, the curves radius became smaller thanks to higher grades achieved, the load is well distributed so that the structural design can be lightened and so on. What is certain is that, thanks to magnetic levitation, trains have increased their speed. Currently, the world record belongs to *Shinkansen* L0 Series in Japan which reached 603 km/h on April 2015.

Nonetheless, a reasonable doubt can be raised: is it possible to achieve even higher speeds? In fact, one can note that another element introduces some limits to propulsion in addition to the friction between wheel and rail: this is the aerodynamic friction. In this contest, the "vactrain", firstly described by the pioneer *Robert Goddard* in 1900 and published by *Salter* then in 1972 [23], has been introduced as the creative idea of a magnetically levitated capsule in evacuated tubes that would allow theoretical speeds of thousands of kilometres per hour. By following what was only an idea at the time, nowadays the hyperloop transport concept is arousing more and more interest form public and companies as they see the possibility of overcoming the current technology limits.

2.1.1 Review of Maglev trains technologies

Magnetic levitation is a physical phenomenon that requires the variation of the magnetic flux in a volume. As it is well known from the theory of electromagnetism, this generates a ***b**ack-**e**lectromotive **f**orce* (**BEMF**). Thus, if the material is a conductive one, a current flow inside the same. Consequently, the interaction with a magnetic field will result in repulsive forces in the mechanical domain. So, if

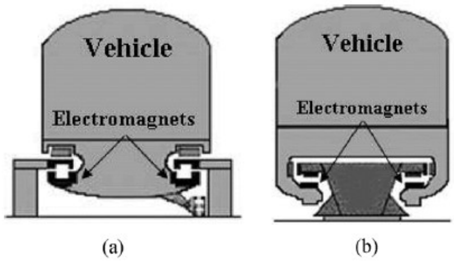

Figure 2.1: Electromagnetic suspension. a) Levitation and guidance integrated. b) Levitation and guidance separated.

in some way the guideway rail is made of conductive material and the source of the magnetic field is mounted on a well-shaped capsule or vice versa, a magnetic levitation transport system can be obtained.

Basically, there are three types of Maglev levitation technologies [24]:

1. ***E****lectro****m****agnetic* ***s****uspension* (**EMS**);
2. Electrodynamic suspension (EDS);
3. ***H****ybrid* ***e****lectromagnetic* ***s****uspension* (**HEMS**).

Typically, these technologies can easily be found in trains transport systems.

Electromagnetic suspension relies on the attraction force between rails made of conductive materials and electromagnets. Since this levitation principle is intrinsically unstable, EMS requires a proper control system that is able to guarantee a uniform air gap.
In the contest of electromagnetic suspension, it is possible to find two different technologies (figure 2.1): the levitation and guidance integrated type and the levitation and guidance independent type. Examples of the former are the *HSST* in Japan and the *UTM* in Korea; the *German Transrapid* is representative the latter instead. Generally speaking, a levitation and guidance integrated EMS is preferred at low speeds thanks to the reduction of power supply and the number of controllers; as cruise velocity increases, the second technology type becomes more favorable because of its design simplicity, even if at an higher cost. Let observe that electromagnetic suspension can work even if no relative speed is present between bogie and rail.

Electrodynamic suspension is based on repulsive force between the guideway track and the capsule. In order to achieve the levitation, a relative velocity is required. It means that this is a fully passive and stable suspension technology. On the other hand, it should be observed that wheels are necessary at low speeds

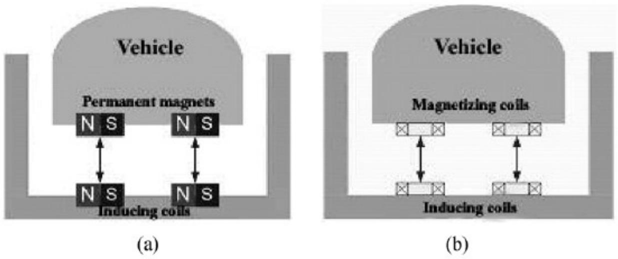

Figure 2.2: Electrodynamic suspension. a) Permanent magnets; b) Superconductive magnets.

and dynamic instability phenomena at higher and higher relative velocities are still unknown. From a design point of view, the guideway can be made up of inducing coils or conducting sheets; the bogie can implement permanent or **s**uper**c**onducting **m**agnet (**SCM**) instead (figure 2.2). Example of the latter one is the Japanese *Shinkansen L0 Series* mentioned above; on the other hand, no commercial trains with PM are present nowadays, but the *Inductrack project* in USA and the Hyperloop challenge are trying to develop such a technology.

Hybrid electromagnetic suspension implements permanent magnet partly used with electromagnets (figure 2.3). This allow the reduction of electric power since for a certain values of air gap, the PM is able to support the train alone. One of the drawbacks of this levitation technology is linked to the fact that amplitude of current control signals would need to be larger than that of traditional EMS one since permanent magnet are permeable like air.

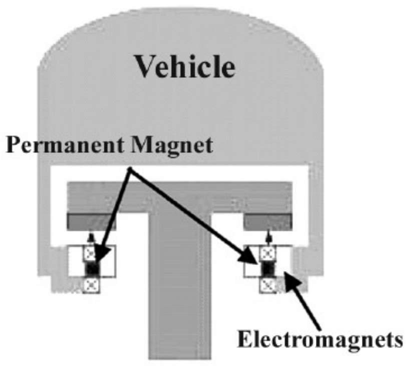

Figure 2.3: Hybrid electromagnetic suspension.

2.1.2 The hyperloop concept

Hyperloop is an electrodynamic suspension train moving at speeds of order of thousands of kilometers per hour inside ideally vacuum tubes (figure 2.4). Although this technology was presented by *Elon Musk* [15] as an air-suspended capsule, the technical and economic advantages related to the electrodynamic levitation prevailed, especially for being passive system at high speeds. Furthermore, what was at the beginning a single translating capsule, it has been transformed into a bogie - pod system to increase dynamic stability.

From a physical point of view, the new version of hyperloop should exploit inductrack concept: a passive levitation system that employs special arrays of PM [12]. The relative velocity between the pod and the guideway makes the magnetic flux of the array to vary inducing eddy current in the track itself. The interaction with permanent magnet produces a strong lift force. Compared with other magnetic levitation technologies, the ratio between lift and drag forces is greater and, moreover, neither cooling system nor complex control circuits are required. Currently, hyperloop is a technology under development about which nothing can yet be concluded. This is no more than a matter of speculation and massive scientific researches. Not only the innumerable advantages mainly related to eco-sustainability and time saving on travels are discussed, but also some drawbacks are highlighted. The investment costs are one of these for sure. They were estimated a price tag of *7 billion* dollars, but historically large infrastructure projects always exceeded their budget. In fact, the economist *UC Berkeley* has predicted a cost of *100 billion* dollars [25]. On the other hand, even the aspect of comfort has been pointed out, mainly questioning about the noisy of compressor fans and the poor atmosphere and scenery expected inside steel tubes. Furthermore, the maintenance of vacuum has been considered expensive and not foregone.

Anyway, whatever the ending of this project will be, a major scientific effort is needed as things stand now.

Figure 2.4: Reproduction of an ideal Hyperloop transport technology.

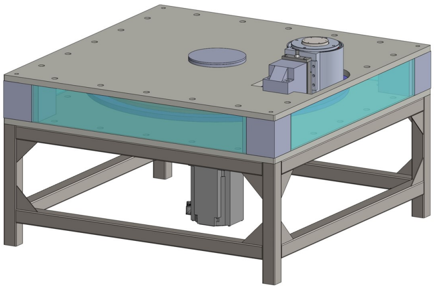

(a)

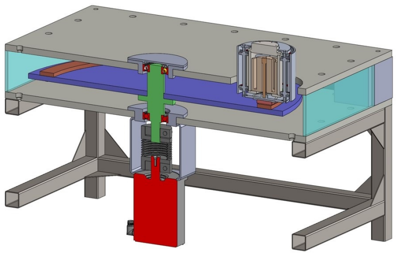

(b)

Figure 2.5: Experimental test bench. a) Isometric view. b) Cross-section view.

2.2 Test bench layout

The test bench used in this work to validate the integrated models under analysis (*Galluzzi et al.* [17]) is a scale model suitable for simulating the vertical dynamics of translating masses suspended electrodynamically via inductrack: this is the case of the hyperloop technology.

Although the following thesis is mainly focused in the dynamic study, it has been seemed appropriate to report a description of the test bench to better understand how the electrodynamic suspension has been simulated. Generally speaking, some indispensable elements can be found in the scale model realized (figure 2.5):

1. Halbach array;
2. Main bench;
3. Quasi-static measuring device;
4. Dynamic measuring device.

In particular, all the elements required to simulate the guideway track are installed in the main horizontal bench; the two measuring devices, on the other hand, simulate the suspended capsules, obviously integrating appropriate data acquiring tools and a permanent magnet facing the guideway. Basically, the electrodynamic suspension requires a relative motion between the track and the bogie. In order to reproduce this condition, one of the meters (depending on whether one want to perform a quasi-static or dynamic analysis) is attached to the stator while the guideway track in the main bench is set in motion. One can observe that this is exactly the contrary of what happens in real life, where the capsule moves along a fixed rail. However, no physical differences are present between the two cases and the motion mechanism control system is significantly simpler.

Configuration	Feature	Symbol	Value
	Number of pole pairs	N_P	1
N45UH NdFeB	Number of magnet per pole pair	N_m	8
	Magnet side length	a_m	12.7mm
	Magnet in-plane depth	d_m	63.5mm

Table 2.1: Halbach array's parameters.

The applied constrains and the measurements instruments are configured to detect information related to the motion along only one direction. It means that from a quasi-static point of view the test bench make possible to analyse lift and drag forces; from a dynamical point of view, the general behaviour related to the vertical dynamics is the only that can be explored, without any information about transversal or rotational effects. These observations are crucial to have a great comprehension of the configuration of the measuring stages.

2.2.1 Halbach array

An *Halbach array* is a particular arrangement of oriented permanent magnets which allows the magnetic field to be strengthen along one face of the array itself. Thus, the magnetic flux results in a sinusoidal spatial distribution.

It was precisely the Halbach array that made it possible to implement permanent magnets in levitation trains. Before its invention, the presence of PM in suspended vehicles was always rejected as they were considered to have a unsuitable weight – lift force ratio.

A general scheme of a 45° Halbach adopted in this thesis work is shown in figure 2.6. It consists of *9* permanents magnets with square cross-section of *12.7* x *12.7* mm and a length of *63.5 mm* [19]. In table 2.1 some characteristic parameters of the array are collected.

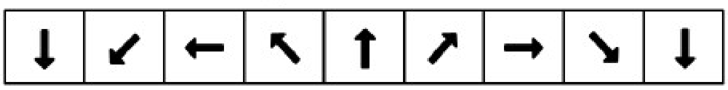

Figure 2.6: 45° Halbach array configuration.

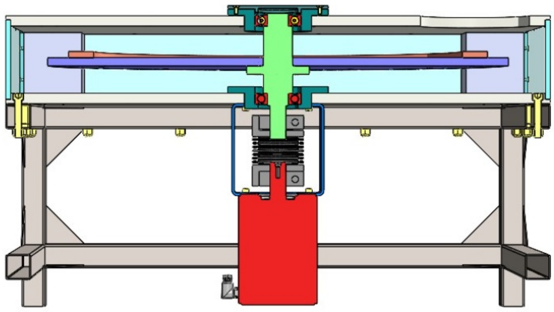

Figure 2.7: Cross-section of the main bench. Courtesy of Dr. A. Bonfitto, Eng.E.C. Zenerino and A. D'Oronzo.

2.2.2 Main bench

In figure 2.7 it is possible to appreciate a cross section of the main test bench and its characteristic components.

Firstly, one can immediately notice the presence of a copper ring attached to an aluminum disk: this is the element that must simulate the guideway track. For this purpose, the aluminum turntable rotates around its axis with a certain angular speed. The peripheral velocity reached close to the copper track is representative of the relative speed required for the electrodynamic suspension. It's clear that in real life the capsule runs along a straight path, while the rail is simulated by a circular guideway in the test bench. Thus, a control of the curvature of the copper ring should be required. In order to get a physical similarity, rotary system diameters as well as elements thicknesses value have been properly designed [18]. Despite careful technical design, complications related to the manufacturing process led to the realization of imperfect components. This is, for example, the copper ring whose surface is not perfectly flat. Irregularities along the guideway have been experimentally studied by *Bo A.* [19]. Their average deviation as a function of the angular position on the track is shown in figure 2.8.

Moveable parts of the main bench are enclosed in a case made up of two square aluminum plate with a side length of *1300 mm*, separated by four spacers placed at the corners. This envelope is then completed by as many transparent rectangular panels made of PVC that allow for a view of the guideway track. All the fixed parts rest on a welded frame which ultimately constitutes the stator.

The rotational power is provided by an electric motor (*Kollmorgen AKM74L* [26]) placed at the bottom of the horizontal bench and connected to a rigid shaft by means of a torsional joint. An appropriate flange realizes then the link with the center of the aluminum turntable. Obviously, a pair of rolling bearings have been chosen and suitable housing have designed to minimize energy losses. The electric motor is then controlled thanks to a *Kollmorgen AKD inverter* [27].

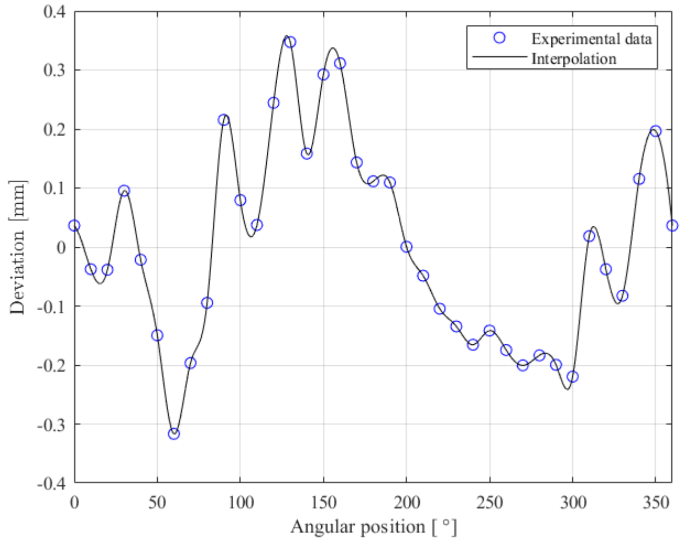

Figure 2.8: Copper track irregularities.

Finally, a hole of suitable size is obtained from the upper aluminum square plate. This is the point in which the quasi-static and dynamic measuring stages, mounted via sledge holder, can communicate with the copper ring track making the scale simulation of the electrodynamic suspension possible.

2.2.3 Quasi-static measuring device

The quasi-static measuring stage can be liked to a triangular cantilever structure that supports the magnetic pad, as shown in figure 2.9.

The key elements of this measuring device are the load cells: these allow the drag and lift forces to be detected. It is interesting to focus on the position of cells themselves, that is neither obvious nor causal. In fact, the complexity of magnetic phenomena as well as the irregularities of all components, from the magnetic pad to the copper track, make the real resultant electrodynamic force to have the direction more complex than the theoretical expected and not easily uncoupling in its main components. This is why one of the load cells is placed at the top of the meter, while the other is set to be near the magnetic pad along the direction of the relative velocity. Furthermore, a pair of horizontal and vertical flexible hinges have been introduced to connect the load cells with the permanent magnet array. In this way, a better decoupling of the lift and drag forces could be obtained.

When only the motion along the vertical direction is considered, electrodynamic quasi-static behaviour is mainly influenced by two parameters, respectively identified in the relative velocity and in the air gap value. The first variable can be imposed

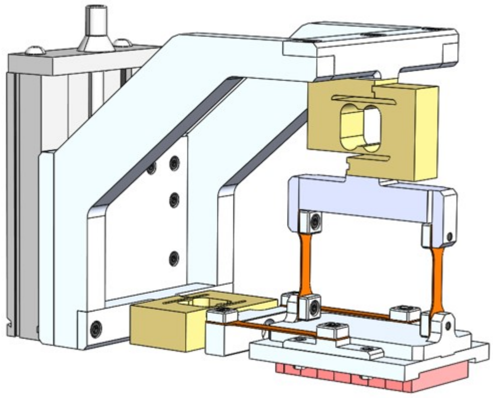

Figure 2.9: Quasi-static measuring device.

in the current test bench by acting on the inverter controller of the electric motor; the distance between the Halbach array and the copper track can be controlled by resorting to a micromectric linear stage. This one basically consists of a micrometric screw which by rotating allows the entire quasi-static meter to be raised and lowered with displacement in the order of hundredth of millimetre.

As already stated in *Chapter 1* (§1.2), the quasi-static validation of the electrodynamic suspension models under analysis has been done in previous works ([19], [20]). Here, only the results in terms of lift and drag curves as a function of the relative velocity and air gap values have been reported (figure 2.10). These graphs refer to the *45°* Halbach array configuration since this is the only magnet arrangement studied in the dynamic analysis summarized in this thesis.

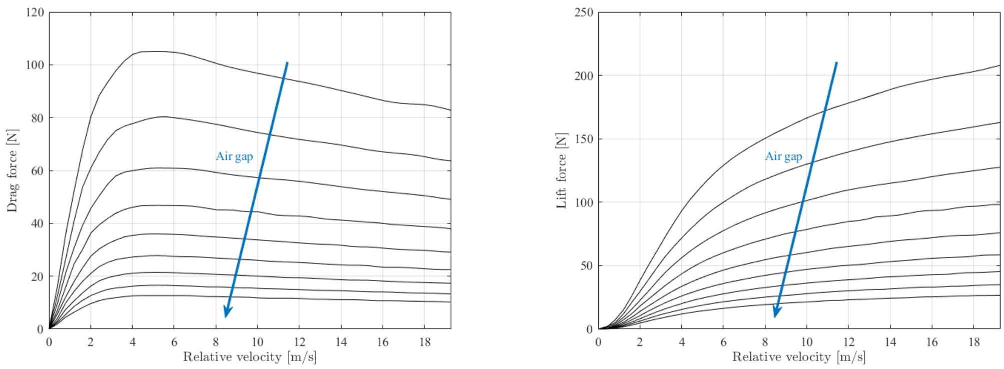

(a) **(b)**

Figure 2.10: Quasi-static experimental results. a) Drag force. b) Lift force. The row show the increasing effect of air gap.

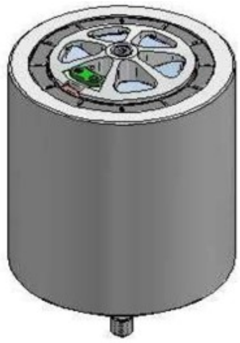

Figure 2.11: Voice coil linear actuator.

2.2.4 Dynamic measuring device

The dynamic measuring device (figure 2.12) is an electro-mechanical dynamic damper consisting of three main parts:

1. Stator;
2. Unsprung mass;
3. Sprung mass.

Furthermore, in order to both control and damp the system, a ***v**oice **c**oil* (**VC**) *linear actuator* [28] has been introduced (figure 2.11).

As it is possible to understand from the figure above, the copper coils are wrapped around an aluminum mover that can slide linearly thanks to a guide housed in the magnetic case. If a current flow in the windings, just the presence of magnets allows the generation of a force: in this sense, the voice coil makes the dynamic measuring device actively controlled. On the other hand, it is clear that this actuator requires a relative movement between the mover and the magnetic stator to properly work and, consequently, these must be mounted on separate parts of the dynamic measuring device.

The stator consists of two holed aluminum disks connected by means of a series of vertical beams. Each of these elements presents a proper shaped slotted housing useful to mount spring elements. The stator is rigidly attached to the welded frame via sledge holder. On the other hand, the mechanical link with the unsprung mass is realized thanks to eight parallel cantilever springs. The arrangement of the connection points between the two parts is such as to prevent from any possible large movement except the vertical one. This is why springs are arranged into two parallel groups of four elements circumferentially placed. In this way, neither transversal nor rotational movements of the dynamic measuring device are allowed.

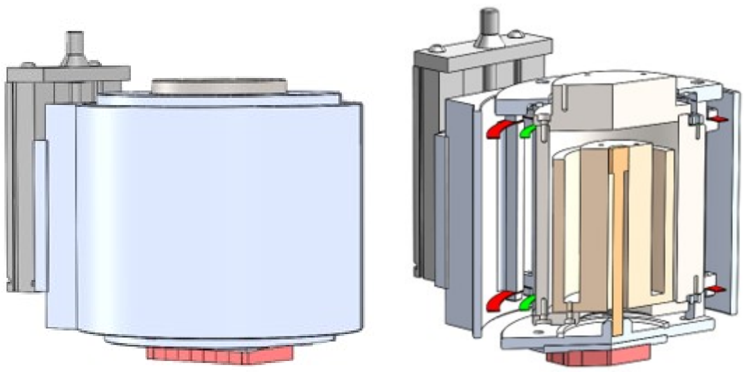

(a) (b)

Figure 2.12: Dynamic measuring device. a) Isometric view. b) Cross-section view.

The unsprung mass should simulate the bogie of hyperloop and it is the part of the dynamic measuring stage which has the permanent magnets facing the track and, so, this is directly subjected to the lift electrodynamic force. From a design point of view, the unsprung mass is similar to the stator: two aluminum plates connected by means of four vertical beams. By focusing attention on the bottom disk, then it is possible to note the presence of the Halbach array on surface facing the copper track and the mover of the voice coil in the opposite one. It is worth to observe that the unsprung mass is attached to the stator by a series of springs: this structural damping is irrelevant compared to the electromagnetic one introduced by the voice coil and can be neglected; on the other hand, if the voice coil is not activated and the system behave as a single block mass, the damping of the spring can influence electromagnetic suspension phenomena and prevent from instability. However, their presence is necessary to keep this dynamic device in position.

Finally, the sprung mass should simulate the pod of hyperloop and it is a ferromagnetic core containing the voice coil stator. To better close the magnetic field lines, this massive block should be covered on the top by a ferromagnetic cap. Although this was foreseen by the initial design, in practise it was necessary to add some shims to prevent the mover from hitting the ferromagnetic cap itself and guarantee in any case a minimum closure of the magnetic field. These shims, made of rigid polymeric material, have a thickness of about *11* mm and has been made through 3D printing.

If the quasi-static stage aim to detect the lift and drag forces through load cells, in the dynamic measuring one it is interesting to evaluate the accelerations involved. This is why, two *PCB accelerometers* have been rigidly connected to the sprung and unsprung masses.

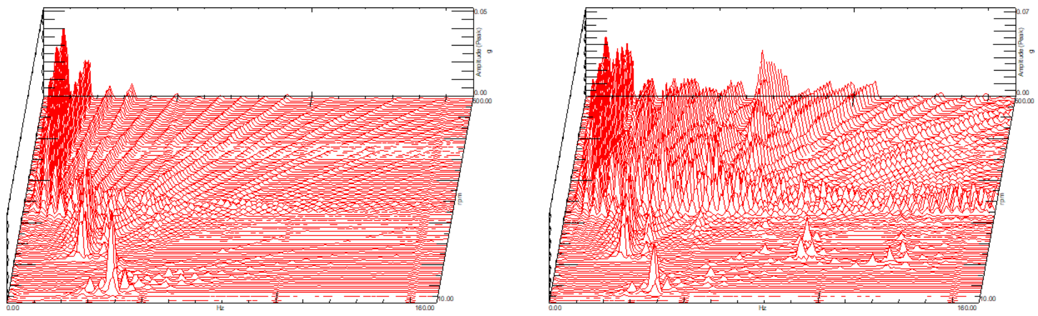

(a) **(b)**

Figure 2.13: Dynamic measuring device. a) Isometric view. b) Cross-section view.

Once the conditioning of acceleration signals is performed, it is possible to mechanically query the system and obtain different receptances. For example, in the figure 2.13 it is shown a cascade plot of the electro-mechanical device described above: curves refer to the frequency transform of the accelerations measurement of both sprung and unsprung masses during the transient from initial configuration up to a steady state velocity. It is worth to observe the presence of peaks close to frequencies multiple of the rotational speed of the rotor and the increasing of the maximum value when the levitation condition is reached. Frequency transform have been computed each increasing of *5* rpm.

Chapter 3

Numerical models and theoretical background

The importance of a suitable numerical model is the possibility to predict the phenomenon represented. It's clear that proper physical laws must be chosen as well as experimental validation should be required.

Among all the possible theoretical models, certainly those that enjoy the property of linearity are preferred. In fact, the superimposition of effects allows a state space representation and a root locus study. The former is the starting point to implement different control strategies; the latter simplify the search for instability conditions. On the other hand, it is worth to note that complex real phenomena always introduce what mathematically appear as nonlinearities. Nevertheless, if the dynamic analysis can be restricted around the equilibrium configuration, excellent results could also be achieved by resorting to linearly simplified equations.

In the following chapter, the numerical models used to represent the dynamic measuring device of the bench under analysis are summarized. These are liner integrated multi-domain models since mechanical and electromagnetic domains are intertwined with each other. Suitable theoretical representations of the electrodynamic suspension, the voice coil system and the mechanical parts of the dynamic stage have been proved necessary. Therefore, these are separately discussed before the introduction of the global integrated model.
Finally, the last section of the chapter is dedicated to a description of the main state observers that are expected to replicate the test bench in real time.

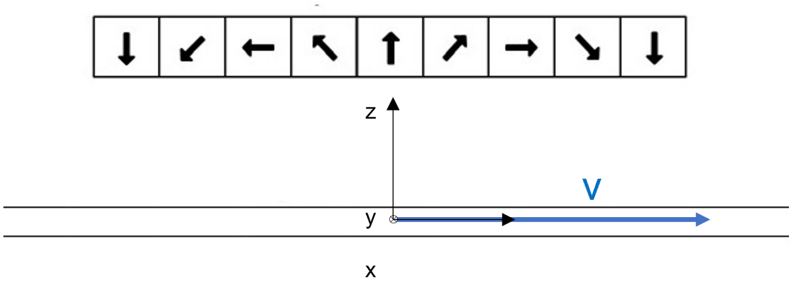

Figure 3.1: Schematirc representation of the bidimensional electrodynamic suspension.

3.1 Electrodynamic suspension

Different numerical models related to electrodynamic suspension can be found in literature according to the technological type considered (§2.1.1). Here, the Inductrack approach is widely explored since the dynamic measuring device under analysis wants to reproduce an Halbach array moving along a guideway made of conductive material.

Thus, let us consider a permanent magnet placed closed to a track moving with velocity $\mathbf{v} = \{v, 0\}^T$ (figure 3.1). Once a proper reference frame is fixed, this bidimensional problem can be studied by resorting to Maxwell's equations [14]

$$\begin{cases} \nabla \times \mathbf{H} &= \mathbf{J} + \dot{\mathbf{D}} \\ \nabla \times \mathbf{E} &= -\dot{\mathbf{B}} \\ \nabla \cdot \mathbf{B} &= 0 \\ \nabla \cdot \mathbf{E} &= \rho_q \end{cases} \tag{3.1}$$

being $\mathbf{H}$ the magnetic field intensity, $\mathbf{B}$ the magnetic flux density, $\mathbf{E}$ the electric field intensity, $\mathbf{D}$ the electric flux density, $\mathbf{J}$ the current density and ρ_q the volume charge density. All vectorial parameters belong to $\mathbb{R}^2$ since only the transversal motion is considered and, so, the component along *y-axes* is keep constant. This system of equations is completed by constitutive laws written for homogeneous and isotropic linear materials

$$\begin{cases} \mathbf{B} &= \mu \mathbf{H} \\ \mathbf{D} &= \epsilon \mathbf{E} \\ \mathbf{J} &= \sigma \mathbf{E} \end{cases} \tag{3.2}$$

where μ is the magnetic permeability, ϵ is the dielectric constant and σ is the track conductivity.
In order to solve the electromagnetic problem, proper border conditions must be introduced. Different regions with different material properties are present, from the permanent magnet up to the track, so that continuity conditions are required too. Furthermore, border effects are implicitly neglected since the in-plane depth of the Halbach geometry exploited in this work has a larger length than others characteristic dimensions.

It is worth to observe that neither charges nor active currents can be detected for the case proposed. Furthermore, the low track relative speeds introduce negligible frequency variation so that time-derivatives can be deleted from the equations without losing precision in the model. In this context, the Faraday's law and the Gauss' law become redundant. By introducing the magnetic vector potential $\mathbf{A}$, it is possible to simplify the system 3.1 as follows

$$\begin{cases} \nabla \times \mathbf{H} & = \sigma(\mathbf{v} \times \mathbf{B}) \\ \nabla \times \mathbf{A} & = \mathbf{B} \end{cases} \tag{3.3}$$

where the expression of current density $\mathbf{J}$ has been rearranged taking into account the related constitutive law (3.2) and by considering a Lorentz term to reproduce the electrodynamic interaction effect inside the guideway.

Finally, the resultant electrodynamic forces acting on the mechanical domain can be computed by resorting to the Maxwell stress tensor.

$$[\sigma] = \frac{1}{4\pi}\left(\mathbf{E} \otimes \mathbf{E} + \mathbf{H} \otimes \mathbf{H} - \frac{|\mathbf{E}|^2 + |\mathbf{H}|^2}{2}\mathbf{I}\right) \tag{3.4}$$

being $\mathbf{I} \in \mathbb{R}^2$ the identity matrix.

It is clear that such a physical problem can not be solved analytically and requires a ***f**inite **e**lement **m**ethod* (**FEM**) approach. Since the main objective of this Chapter is fully development of a linear integrated model with suitable state space representation, such an analysis has not been performed. Anyway, it is possible to appreciate some interesting numerical results from the paper of *Galluzzi et al,* [17].Here, color maps are shown to give an idea of the magnetic flux and eddy currents distributions for an aluminum guideway in stationary conditions. As it is expected, induced currents tend to appear with stronger intensity closed to the track surface facing the permanent magnet.

3.1.1 Lumped-parameter approach

The Maxwell's equations lead to a complete and precise representation of the electrodynamic levitation phenomena but, on the other hand, the related model is

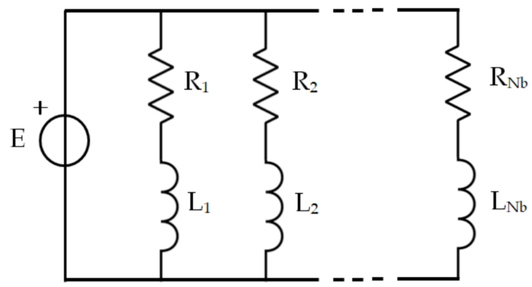

Figure 3.2: Electric parallel circuit.

non-linear and not trivially combinable with mechanical quantities. An equivalent and approximated approach which can easily fulfill these requirements is that proposed by *Galluzzi et al,* [17]. Here, the main idea is the possibility of modelling the electrodynamic suspension by introducing an electrical parallel of N_b branches (figure 3.2) able to reproduce the current behaviour inside the guideway track. If specific resistance R_k and inductance L_k values are assigned to each branch k of the circuit and proper number N_b is carefully choose, a good approximation of the exact electrodynamic suspension can be obtained.

In this context, the Maxwell's partial-differential equations are substituted by N_b ordinary first-order equations of the type

$$L_k \frac{di_k}{dt} + R_k i_k + E = 0 \qquad k = 1, 2...N_b \tag{3.5}$$

being E the back-electromotive force and i_k the current flowing in the k_{th} branch. The simplicity of the previous formula is however followed by the need to better specify i_k and E terms.

A first observation is that the electric parallel of branches is simulating a moving system, i.e. the guideway track. Therefore, the current term should be correct taking into account that it is referred to a moving (rotating) reference frame. If ω is the characteristic frequency, then it is possible to resort to the complex notation and write

$$i_k = i_{k,r} e^{j\omega t} \qquad k = 1, 2...N_b \tag{3.6}$$

being $i_{k,r}$ the current flowing in the k_{th} branch as seen by an observer rigidly connected to the moving track itself and, generally, composed of a direct and quadrature component with respect to the excitation source.

$$i_{k,r} = i_{k,d} + j i_{k,q} \qquad k = 1, 2...N_b \tag{3.7}$$

On the other side of the formula 3.4, the back-electromotive force E should be stated. By remembering the Faraday's law, this is the time-derivative of magnetic flux linkage λ.

$$E = \frac{d\lambda}{dt} \tag{3.8}$$

It is well known that the magnetic field associated to an Halbach array is an exponential function of the air gap z and it has a sinusoidal-type spatial distribution with amplitude Λ_0 and pole pitch ratio or wavelength equal to

$$\gamma = \frac{N_m a_m}{2\pi} \tag{3.9}$$

where all the parameters appearing in the equation are summarized in **??**. If the track is moving with relative speed equal to v, than it is possible to express the magnetic flux linkage as follows

$$\lambda = \Lambda_0 e^{j\frac{v}{\gamma}} e^{\frac{z_{PM}}{\gamma}} \tag{3.10}$$

being z_{PM} the air gap between the permanent magnets array and the copper track. It is worth to observe that the ratio v/γ coincides with the characteristic frequency ω introduced above to represent the term $i_{k,r}$.

By knowing the expression of the current i_k and the back-electromotive force E, the differential equation 3.5 can be properly rearranged. In particular, it is possible to derive two expression for the direct and quadrature components of the current so that for the k_{th} branch it results

$$\begin{cases} \frac{di_{k,d}}{dt} & = -\frac{R_k}{L_k} i_{k,d} + \omega i_{k,q} - \frac{1}{L_k}\left(\frac{\partial\lambda}{\partial z_{PM}} \dot{z}_{PM}\right) \\ \frac{di_{k,q}}{dt} & = -\frac{R_k}{L_k} i_{k,q} - \omega i_{k,d} - \frac{1}{L_k}\left(\Lambda\omega\right) \end{cases} \tag{3.11}$$

A system of $2k$ equations is thus obtained.

Finally, the resultant electrodynamic forces acting on the mechanical domain can be computed by resorting to a power balance equation. Assuming the superimposition of the N_b branches, the drag and lift forces can be expressed by

$$\begin{cases} F_{drag} & = \frac{\Lambda_0^2}{\gamma} e^{-\frac{2z_{PM}}{\gamma}} \sum_{k=1}^{N_b} \left(\frac{\omega/\omega_{k,p}}{L_k\left(1+\omega^2/\omega_{k,p}^2\right)}\right) \\ F_{lift} & = \frac{\Lambda_0^2}{\gamma} e^{-\frac{2z_{PM}}{\gamma}} \sum_{k=1}^{N_b} \left(\frac{\omega^2/\omega_{k,p}^2}{L_k\left(1+\omega^2/\omega_{k,p}^2\right)}\right) \end{cases} \tag{3.12}$$

where $\omega_{k,p}$ is the ratio R_k/L_k, i.e. the pole of the k_{th} branch. It is worth to observe that the lift and drag forces are related respectively to the direct and quadrature component of the current. In the following work, only the lift force is of interest for sure. If m_0 is a trial mass of the magnetic pad, an ultimate differential equation can be written in the mechanical domain by resorting to the Newton law.

$$m_0 \ddot{z}_{PM} = F_{lift} - m_0 g \tag{3.13}$$

being g the gravity acceleration.

The system of $2N_b$ equations of the type 3.11 together with the relation 3.12 and the mechanical equation 3.13 represent a numerical model of an electrodynamic suspension characterized by a permanent magnet and a continuous conductive material guideway. Although it is simpler than integrating Maxwell's equations, unfortunately this system is nonlinear so that it can not be easily used to analyze the vertical dynamics.

3.1.2 Linearized lumped-parameter approach

The lumped-parameter approach discussed in the previous section allows a representation of the electrodynamic suspension but it has still non-linear. For a preliminary analysis of the dynamic instability of electrodynamic suspension, which is what is discussed in this thesis, a linearization could be useful. It is worth to note the non-linearity is directly linked to the expression of the magnetic flux linkage (3.9) which exponentially depends on the air gap z_{PM} and whose time-variation is intrinsically linked to the relative speed v. Thus, in the hypothesis of small displacements, it is possible to linearized the flux linkage amplitude around a vertical displacement $z_{PM,0}$ for a given relative velocity v, so that

$$\bar{\Lambda} = \lambda_0 e^{\frac{z_{PM,0}}{\gamma}} - \frac{\lambda_0}{\gamma} e^{\frac{z_{PM,0}}{\gamma}} (z_{PM} - z_{PM,0}) \tag{3.14}$$

Hence, the k_{th} system of equations 3.11 can be rewritten as

$$\begin{cases} \frac{di_{k,d}}{dt} &= -\frac{R_k}{L_k} i_{k,d} + \omega i_{k,q} + \frac{\Lambda_0}{\gamma L_k} e^{\frac{z_{PM,0}}{\gamma}} \dot{z}_{PM} \\ \frac{di_{k,q}}{dt} &= -\frac{R_k}{L_k} i_{k,q} - \omega i_{k,d} + \frac{\omega \Lambda_0}{\gamma L_k} e^{\frac{z_{PM,0}}{\gamma}} (z_{PM} - z_{PM,0}) - \frac{\omega \Lambda_0}{L_k} e^{\frac{z_{PM,0}}{\gamma}} \end{cases} \tag{3.15}$$

Finally, the resultant electrodynamic lift force acting on the mechanical domain is rearranged as follows

$$\bar{F}_{lift} = -\sum_{k=1}^{N_b} \left(\frac{\Lambda_0^2}{\gamma L_k} e^{\frac{2z_{PM,0}}{\gamma}} + \frac{2\Lambda_0}{\gamma} e^{\frac{z_{PM,0}}{\gamma}} i_{k,d} \right) \tag{3.16}$$

Again, the vertical dynamics can be explored by assigning a trivial mass m_0 to the magnetic pad and writing the related Newton's law, quite similar to the equation 3.13 but now whit a linearized lift force.

The system of $2N_b$ equations of the type 3.14 together with the relation 3.15

N° []	$R_k[\omega]$	$L_k[H]$	$\omega_{p,k}[rad/s]$
1	25.28	0.1084	233.17
2	257.79	0.1799	1432.4

Table 3.1: Lumped-parameter model parameters for modelling the electrodynamic interaction between an Halbach array and a copper track.

and the mechanical equation 3.13 represent a numerical linear model of an electrodynamic suspension, once the number of branches have been properly chosen. This result can be achieved by tuning the linearized lift forces as a function of the air gap z and the relative speed v to the experimental curve obtained during the quasi-static tests (figure 2.10). However, such a analysis has been carried out by *Pakštys* [21]. Here, related results are just summarized and discussed. In particular, it is worth to underline that the value of the flux linkage amplitude Λ_0 is important to derive the electromagnetic pole frequency of the branches and obtain a precise representation of the magnetic flux linkage. On the other hand, since the main goal of the thesis is to study the vertical dynamics and not to get the correct electromagnetic representation of the levitation system, it is possible to chose any theoretically possible value for the amplitude Λ_0. This is because the lift force is dependent on the ratio between the inductance and resistance of the k_th branch rather than the absolute values: in this sense, the amplitude of the magnetic flux linkage is irrelevant. Finally, a value of $\Lambda_0 = 1Wb$ and a number of $k = 2$ branches have been considered enough to fit the numerical and experimental lift and drag force curves. Furthermore, in the table 3.1 all the characteristic parameters of the electrodynamic suspension linearized model are collected. The guideway track has been considered to made of copper material.

3.1.3 State space representation

The vertical dynamics around the equilibrium air gap $z_{PM,0}$ of an electrodymical suspended mass m_0 with permanent magnet moving along a track made of a conductive material with velocity v can be modelled by resorting to the following system of differential linear equations

$$\begin{cases} \frac{di_{1,d}}{dt} & = -\omega_{1,p} i_{1,d} + \omega i_{1,q} + \frac{\Lambda_0}{\gamma L_1} e^{-\frac{z_{us,0}}{\gamma}} \dot{z}_{PM} \\ \frac{di_{1,q}}{dt} & = -\omega_{1,p} i_{1,q} - \omega i_{1,d} + \frac{\omega\Lambda_0}{\gamma L_1} e^{\frac{-z_{PM,0}}{\gamma}} z_{PM} \\ \frac{di_{2,d}}{dt} & = -\omega_{2,p} i_{2,d} + \omega i_{2,q} + \frac{\Lambda_0}{\gamma L_2} e^{-\frac{z_{PM,0}}{\gamma}} \dot{z}_{PM} \\ \frac{di_{2,q}}{dt} & = -\omega_{2,p} i_{2,q} - \omega i_{2,d} + \frac{\omega\Lambda_0}{\gamma L_2} e^{-\frac{z_{PM,0}}{\gamma}} z_{PM} \\ \ddot{z}_{PM} & = \quad \frac{f_{PM}}{m_0} - \frac{2\Lambda_0}{\gamma m_0} e^{\frac{-z_{PM,0}}{\gamma}} i_{1,d} + \frac{2\Lambda_0}{\gamma m_0} e^{-\frac{z_{PM,0}}{\gamma}} i_{2,d} \end{cases} \tag{3.17}$$

which can be also rewritten so that only first-order differential equations appear

$$\begin{cases} \frac{di_{1,d}}{dt} & = -\omega_{1,p} i_{1,d} + \omega i_{1,q} + \frac{\Lambda_0}{\gamma L_1} e^{\frac{-z_{PM,0}}{\gamma}} \dot{z}_{PM} \\ \frac{di_{1,q}}{dt} & = -\omega_{1,p} i_{1,q} - \omega i_{1,d} + \frac{\omega\Lambda_0}{\gamma L_1} e^{-\frac{z_{PM,0}}{\gamma}} z_{PM} \\ \frac{di_{2,d}}{dt} & = -\omega_{2,p} i_{2,d} + \omega i_{2,q} + \frac{\Lambda_0}{\gamma L_2} e^{-\frac{z_{PM,0}}{\gamma}} \dot{z}_{PM} \\ \frac{di_{2,q}}{dt} & = -\omega_{2,p} i_{2,q} - \omega i_{2,d} + \frac{\omega\Lambda_0}{\gamma L_2} e^{-\frac{z_{PM,0}}{\gamma}} z_{PM} \\ \dot{v}_{PM} & = \quad \frac{f_{PM}}{m_0} - \frac{2\Lambda_0}{\gamma m_0} e^{-\frac{z_{PM,0}}{\gamma}} i_{1,d} - \frac{2\Lambda_0}{\gamma m_0} e^{-\frac{z_{PM,0}}{\gamma}} i_{2,d} \\ v_{PM} & = \quad \dot{z}_{PM} \end{cases} \tag{3.18}$$

being f_{PM} an external force applied to the permanent magnet (or in general to the trial mass m_0).

Since irregularities of track itself can introduce excitation to the system, a more correct description of the electrodynamic suspension is the following

$$\begin{cases} \frac{di_{1,d}}{dt} & = -\omega_{1,p} i_{1,d} + \omega i_{1,q} + \frac{\Lambda_0}{\gamma L_1} e^{\frac{-z_{PM,0}}{\gamma}} \dot{z}_{PM} \\ \frac{di_{1,q}}{dt} & = -\omega_{1,p} i_{1,q} - \omega i_{1,d} + \frac{\omega\Lambda_0}{\gamma L_1} e^{-\frac{z_{PM,0}}{\gamma}} z_{PM} - \frac{\omega\Lambda_0}{\gamma L_1} e^{-\frac{z_{PM,0}}{\gamma}} z_{in} \\ \frac{di_{2,d}}{dt} & = -\omega_{2,p} i_{2,d} + \omega i_{2,q} + \frac{\Lambda_0}{\gamma L_2} e^{-\frac{z_{PM,0}}{\gamma}} \dot{z}_{PM} \\ \frac{di_{2,q}}{dt} & = -\omega_{2,p} i_{2,q} - \omega i_{2,d} + \frac{\omega\Lambda_0}{\gamma L_2} e^{-\frac{z_{PM,0}}{\gamma}} z_{PM} - \frac{\omega\Lambda_0}{\gamma L_2} e^{-\frac{z_{PM,0}}{\gamma}} z_{in} \\ \dot{z}_{in} & = \quad \dot{z}_{in} \\ \dot{v}_{PM} & = \quad \frac{f_{PM}}{m_0} - \frac{2\Lambda_0}{\gamma m_0} e^{-\frac{z_{PM,0}}{\gamma}} i_{1,d} - \frac{2\Lambda_0}{\gamma m_0} e^{-\frac{z_{PM,0}}{\gamma}} i_{2,d} \\ v_{PM} & = \quad \dot{z}_{PM} \end{cases} \tag{3.19}$$

It is worth to observe that any disturbances associated to the geometry of the guideway enter the system in terms of velocity and require an additional trivial equation for the added unknown variable z_{in}. Moreover, the weight and the mean value of the levitation force xan be considered perfectly balanced, so that it is possible to neglect their contribution by focusing only on the effect of the deviation from the equilibrium configuration.

The presence of a mass allows for the computation of the value of $z_{PM,0}$ that satisfies the equilibrium within the speed range of interest. In static condition, the lift force matches the weight force and the levitation air gap is obtained as

$$z_{PM,0}(\omega) = -\frac{\gamma}{2} ln \left(\frac{m_0 g \gamma}{\lambda_0^2 \Gamma(\omega)} \right) \tag{3.20}$$

being

$$\Gamma(\omega) = \sum_{k=1}^{N_b} \left(\frac{\omega^2/\omega_{k,p}^2}{L_k \left(1 + \omega^2/\omega_{k,p}^2\right)} \right) \tag{3.21}$$

The unknown variables can be collected in a state vector of the type

$$\{Z\}_{EDS} = \{i_{1,d}, i_{1,q}, i_{2,d}, i_{2,q}, z_{in}, \dot{z}_{PM}, z_{PM}\}^T \tag{3.22}$$

while the input of the system can be identified in the parameters appearing in the vector

$$\{U\}_{EDS} = \{\dot{z}_{PM,in}, f_{PM}\}^T \tag{3.23}$$

Since the final goal of the whole project will be a passenger comfort analysis, the main output of interest can be identified in the acceleration, so that the output vector is

$$\{Y\}_{EDS} = \{\ddot{z}_{PM}\}^T \tag{3.24}$$

Finally, the electrodynamic suspension model so obtained is a 2 *Input* - 1 *Output* system which allows for the following state-space representation

$$\begin{cases} \left\{\dot{Z}\right\}_{EDS} & = [A]_{EDS} \{Z\}_{EDS} + [B]_{EDS} \{U\}_{EDS} \\ \{Y_{EDS}\} & = [C]_{EDS} \{Z\}_{EDS} + [D]_{EDS} \{U\}_{EDS} \end{cases} \tag{3.25}$$

being $[A]_{EDS}$ the dynamic matrix, $[B]_{EDS}]$ the input gain matrix, $[C]_{EDS}]$the output gain matrix and $[D]_{EDS}$ the direct link matrix. All the expression of these operators can be consulted in the Appendix A1.

3.1.4 Preliminary root locus analysis

In order to carry out a preliminary root locus analysis of the electrodynamic suspension, a trial mass of $m_0 = 20.18Kg$ has been considered. Once all the parameters of system 3.18 have been fixed (table 3.2), the dynamic stability of the system can be studied as a function of the velocity of the guideway track at the reference equilibrium air gap z_{p0}.

The levitated trial mass so considered is characterized by 7 **d**egrees **o**f **f**reedom (**DOF**), thus 2 pairs of complex conjugated electrodynamic poles, 1 pole associated to the irregularities effect and 1 pair of complex mechanical pole can be computed.

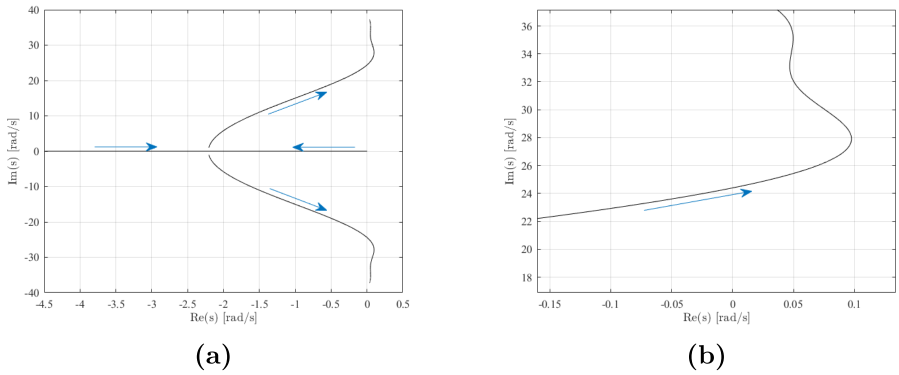

Figure 3.3: Root locus. a) Mechanical pole. b) Zoom-in view.

Since the dynamic instability takes place in the mechanical domain, only the latter poles are shown in the root locus plot of figure 3.9. It is worth to observe that the increasing of the relative speed v drive the curve to cross the imaginary axis before to collapse close to the natural frequency. Therefore, poles can assume positive real part and bring the system to a dynamic instability.

Although the model considered has not yet been experimentally validated, it should however be borne in mind that this is able to perfectly represent the electrodynamic levitated dynamic measuring instrument in the absence of an active contribution by the voice coil. By considering values assumed by the main parameters, the instability would occur at a velocity of $v = 4.77 m/s$ which, being the copper mean radius equal to 0.47m, corresponds to a spin speed of the rotor of $\Omega = 97 rpm$: basically, the test bench should always work in instability condition since the velocity needed to balance the weight forces is greater than $v = 140 m/s$. On the other hand, the instability cannot be appreciated neither from figure 2.13 nor experimentally. This is because in the real system there are some spring elements between ground and dynamic stage which have a small but no-zero damping effect. Therefore, once the integrated numerical models have been experimentally validated, the sub-matrices referable to the state space equations 3.19, in addition to a correction concerning the springs, will constitute an excellent numerical approximation of the dynamic measurement device in the absence of active work by the electric actuator.

$\Lambda_0[Wb]$	$\gamma[1/rad]$	$m_0[Kg]$	$\omega_{p,k}[rad/s]$
1		0.0162	20.16

Table 3.2: Electrodynamic suspension parameters.

3.2 Voice coil actuator

The voice coil actuator is an electromagnetic device that is able to supply an active force when a current different from zero flows inside its windings. This is due to the presence of permanent magnets facing the inner surface of the hollow circular case, which generate a radial spatial distributed constant magnetic field. Having established that the direction of the flowing active current is circumferential and that of the magnetic flux is radial, it is possible to state that the average Lorentz's force is directed along the axis of the voice coil mover.

It is worth to observe that the presence of a constant magnetic field also influences the electric domain. This is not only for a kind of a complex mutual inductance between the ferromagnetic core material and the copper coils, but also because the movement of the mover during the active actuation causes part of the windings to leave the magnetized space generating a variation of the magnetic flux. As it is now well known, this is associated with the appearance of a back-electromotive force in the electrical domain. Furthermore, this BEMF causes current to flow in the circuits to which, again in the mechanical domain, a force directed in the opposite direction to the speed is associated. This suggests a sort of passive viscous electromagnetic friction

In general, the voice coil actuator under analysis is a complex device to be modelled. This is for different reasons:

1. The fact that the windings can leave the magnetized space inside the case is a fundamental requirement for the correct operation of the actuator, but it introduces non-negligible border effects. Furthermore, it is not possible to exclude the variation of some representative electromechanical quantities with the offset (i.e. the displacement of the VC);

2. Inductance properties should take into account the geometry of the copper coils as well as the effect related to both the aluminum frame and permeability of the permanent magnets;

3. Both the active force supplied and the back-electromotive force involve also the aluminum frame since it is made of a conductive material;

4. A kind of non-neglegible static friction characterizes the dynamic contact between the mover and the related housing;

5. High flowing active currents dissipate lot of energy because of the Joule effect increasing the temperature and introducing a further variation of the electric quantities (especially the resistance).

In practice, all these aspects prevent the model to be linear. Thus, a great approximation have been required.

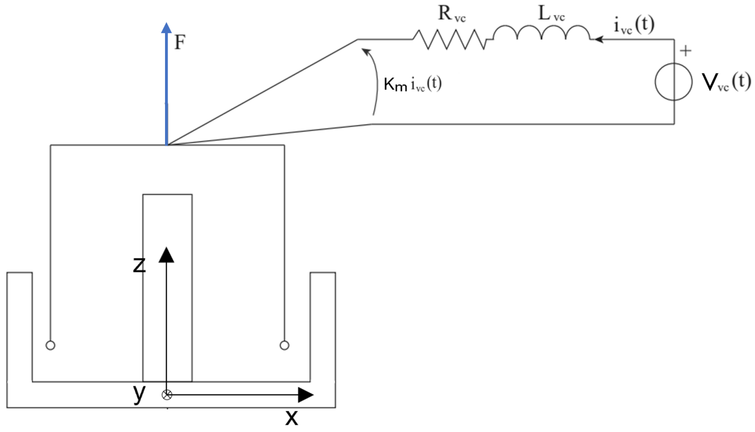

Figure 3.4: Schematic representation of the voice coil actuator.

3.2.1 Mechanical domain

Let us introduce and define the mechanical voice coil constant K_m as the active force $F_{vc,A}$ provided by the device itself for a current of $i_{vc} = 1A$ flowing in its windings. It depends mainly on the geometry and the material of the mover as well as the intensity of the magnetic field generated by the ferromagnetic core of the envelope. The value of the mechanical voice coil constant is provided by the manufacturer [28] and allows the following relation to be written

$$F_{vc,A} = K_m(z_{vc}, T) \cdot i_{vc} \tag{3.26}$$

being i_{vc} the active current flowing in the copper coils, T the temperature of the system and z_{vc} the offset-displacement of the mover.

The force described in equation 3.27 can be defined as the active contribution of the voice coil. On the other hand, a sort of electromagnetic friction is exerted by the device even if the active voltage is equal to zero, as long as there is a relative movement between windings and magnets. This effect can be seen as a passive force $F_{vc,P}$ generally dependent on the relative speed $\dot{z}_{vc}$, the excitation frequency ω, the mover offset z_{vc} and the temperature T.

If the moving trial mass is globally equal to m_0 and the reference frame of figure 3.4 is considered, previous considerations allow to write a mechanical equation of the type

$$m_0\ddot{z} = K_m(z_{vc}, T) \cdot i_{vc} + F_{vc,P}(\dot{z}_{vc}, z, \omega, T) - m_0 g \tag{3.27}$$

which is clearly a non-linear second order differential equation.

The previous model can be linearized if, for example, it is possible to consider small oscillations around a pre-set offset z_{vc}, to neglect the effect of the increasing of temperature, to work at low frequency and mean current value and to restrict the frequency range of interest. Under these hypotheses, the voice coil can be modelled by resorting to the following numerical linear equation

$$m_0\ddot{z} + c_{vc}v = K_m i_{vc} - m_0 g \tag{3.28}$$

being c_{vc} the constant electromagnetic damping.
It is worth to say that the hypotheses introduced above are not so limiting, perhaps except for the offset and temperature dependence. However, even in this case it is possible to point out the fact that the voice coil behaves as a mechanical low-pass filter, whereby large displacement never manifest themselves in practice. Furthermore, if the duration of the excitation is small enough or a new thermal equilibrium is reached, the effect of the temperature can be neglected.

In conclusion, equation 3.28 can be considered a reliable linear model to characterizing the behaviour of the voice coil actuator in the mechanical domain.

3.2.2 Electric domain

The electrical behavior of the voice coil changes depending on whether the mover is inserted or not in the magnetic case. In the latter case, it is not difficult to recognize that the mover alone can be assimilated as a pure RL circuit, so that the electric equation become

$$L_{vc}(T)\frac{di_{vc}}{dt} + R_{vc}(T)i_{vc} = V \tag{3.29}$$

being L_{vc} the inductance of the coil geometry, R_{vc} the resistance of the windings and V the applied voltage.

When the mover is even partially inserted in its envelope, the contribution due to the interaction with the constant magnetic field as well as the presence of aluminum parts should be considered. In this context, a more understandable electric model can be obtained if the response due to the windings only is separated from that concerning all the remaining effects. In the first case, by following what has been done in the mechanical domain, it is possible to introduce an electric voice coil constant K_e, This quantity can be defined as the back-electromotive force ΔV_{BEMF} induced by the magnetic field inside the windings when the relative speed is equal to $\dot{z}_{vc} = 1m/s$. This is the only contribution due to the copper coils and it depends mainly on the geometry and the material of the mover as well as the intensity of the magnetic field generated by the ferromagnetic core of the envelope. The value of the electric voice coil is provided by the manufacturer [28] and, as a first approximation, it can be assumed equal to the mechanical constant K_m. Thus, the following relation can be written

$$\Delta V_{BEMF} = K_m(z_{vc}, T) \cdot \dot{z}_{vc} \tag{3.30}$$

On the other hand, the effect related to the interaction whit the ferromagnetic core and the alluminum parts of the mover is too complex to model dealing with linear equations. Strong non-linearities characterize the mutual influence between windings and other parts of the voice coil and the possibility that the relative motion can change the geometric configuration to be analyzed further complicate the analyzes which, obviously, would require the integration of Maxwell's laws (3.1) with a finite element approach. Since the main goal of this thesis is not the modeling of such an actuator, all these effects are summarized in a general unknown voltage counter-acting effect ΔV_{others}.

If the mover is considered to partially stay inside its magnetic case, previous considerations allow to write an electric equation of the type

$$L_{vc}(T)\frac{di_{vc}}{dt} + R_{vc}(T)i_{vc} + K_m(z_{vc}, T) \cdot \dot{z}_{vc} + \Delta V_{others}(\dot{z}_{vc}, z, \omega, T) = V \tag{3.31}$$

which is clearly a non-linear equation with unknown parameters.

A first step to try to make the previous equation available is to neglect the term related to the counter-acting voltage effects of aluminum parts and ferromagnetic core during the relative motion (i.e. to model the actuator as an RL circuit). The following equation is thus obtained

$$L_{vc}(T)\frac{di_{vc}}{dt} + R_{vc}(T)i_{vc} + K_m(z_{vc}, T) \cdot \dot{z}_{vc} = V \tag{3.32}$$

It is clear that the removal of the term ΔV_{others} from the equation 3.31 lead to a wrong model which is not able to represent the electrical behavior of the voice coil at all. Furthermore the strong depence on the temperature make the equation non-linear.

A possible solution to increase the efficiency of the model 3.32 is to introduce a more complex characterization of the inductance $L_{vc,m}$ that depends on the relative speed $\dot{z}_{vc}$, the excitation frequency ω, the mover offset z_{vc} and the temperature T, so that it is possible to write

$$L_{vc,m}(\dot{z}_{vc}, z, \omega, T)\frac{di_{vc}}{dt} + R_{vc}(T)i_{vc} + K_m(z_{vc}, T) \cdot \dot{z}_{vc} = V \tag{3.33}$$

Let observe that such a complex parameter is dictated by an experimental evidence. In particular, without taking into account the effect related to other elements of the voice coil and keeping constant R and K_m, the inductance apparently appear to vary with frequency, temperature and offset if one try to estimate it. This is clearly not certain.

Starting from the previous equation, a linearization can be performed on the hypotheses of small oscillations around a pre-set offset z_{vc}, neglegible effect of the increasing of temperature, low frequency and mean current value and limited frequency range of interest.Thus, a more accurate model can be obtained

$$\bar{L}_{vc}\frac{di_{vc}}{dt} + R_{vc}i_{vc} + K_m\dot{z}_{vc} = V \tag{3.34}$$

being $\bar{L}_{vc}$ a fictitious average value of inductance which should improve the accuracy of the results.

Contrary to what has been seen for the mechanical domain, the linear model derived for the electrical one is largely approximate. Although the voice coil behaves like an electric low-pass filter and both the assumptions of small oscillations and negligible variation with frequency can be respected, the linearized RL model is too simple to describe the complex behaviour of the actuator. Moreover, the effect of the increasing of the temperature on electric quantities is stronger, especially for the resistance R.

3.2.3 State space representation

The vertical dynamics of a voice coil actuator with a moving mass m_0 can be approximated by resorting to the following system of differential linear equations

$$\begin{cases} \ddot{z}_{vc} & = -g - \frac{c_{vc}}{m_0}\dot{z}_{vc} + \frac{K_m}{m_0}i_{vc} \\ \frac{di_{vc}}{dt} & = \quad \frac{V}{\bar{L}_{vc}} - \frac{R_{vc}}{\bar{L}_{vc}}i_{vc} + \frac{K_m}{\bar{L}_{vc}}\dot{z}_{vc} \end{cases} \tag{3.35}$$

which can be also rewritten so that only first-order differential equations appear and a generic external force f_{vc}, including the weight, is considered

$$\begin{cases} \dot{v}_{vc} & = \frac{f_{vc}}{m_0} - \frac{c_{vc}}{m_0}v_{vc} + \frac{K_m}{m_0}i_{vc} \\ v_{vc} & = \dot{z}_{vc} \\ \frac{di_{vc}}{dt} & = \frac{V}{\bar{L}_{vc}} - \frac{R_{vc}}{\bar{L}_{vc}}i_{vc} + \frac{K_m}{\bar{L}_{vc}}v_{vc} \end{cases} \tag{3.36}$$

The equilibrium configuration can be studied, so that the dynamic analysis can refers only to oscillation around the mean position. Since the system can be perturbed by means of external forces and applied voltage, it is preferred to separate the two effect. In particular, if only external forces are applied, the equilibrium configuration is described by the following results

$$\begin{cases} v_{vc,0} & = 0 \\ i_{vc,0} & = 0 \end{cases} \tag{3.37}$$

while if only applied voltage is exciting the system, it results

$$\begin{cases} v_{vc,0} & = 0 \\ i_{vc,0} & = \frac{V}{R} \end{cases} \tag{3.38}$$

In both case, the equilibrium position can be computed numerically by resorting to an integration of the equations 3.36.

The unknown variables can be collected in a state vector of the type

$$\{Z\}_{vc} = \{v_{vc}, z_{vc}, i_{vc}\}^T \tag{3.39}$$

while the input of the system can be identified in the parameters appearing in the vector

$$\{U\}_{vc} = \left\{f_{vc}, \frac{1}{R}\right\}^T \tag{3.40}$$

Since the final goal of the whole project will be a passenger comfort analysis, the main output of interest can be identified in the acceleration, so that the output vector is

$$\{Y\}_{vc} = \{\ddot{z}_{vc}\}^T \tag{3.41}$$

Finally, the voice coil actuator model so obtained is a 2 *Input* - 1 *Output* system which allows for the following state-space representation

$$\begin{cases} \left\{\dot{Z}\right\}_{vc} & = [A]_{vc}\,\{Z\}_{vc} + [B]_{vc}\,\{U\}_{vc} \\ \{Y\}_{vc} & = [C]_{vc}\,\{Z\}_{vc} + [D]_{vc}\,\{U\}_{vc} \end{cases} \tag{3.42}$$

being $[A]_{vc}$ the dynamic matrix, $[B]_{vc}$ the input gain matrix, $[C]_{vc}$ the output gain matrix and $[D]_{vc}$ the direct link matrix. All the expression of these operators can be consulted in the Appendix A.

Let reflect for a while on the written equations. These refer to a voice coil mover moving inside an infinitely long magnetized space without neither border effects nor influence of other parts made of conductive material. In fact, as said in the previous section, the electric model is incorrect. On the other hand, considering the objectives of the whole project, this modelling error is not so harmful since the system should be current controlled. Let note that from a mechanical point of view, the interaction between voltage and current in the electric domain is not noticeable since only the absolute value of the current enter the mechanical system as an external force. So, the model will not be electrically correct, but may adequately represent the dynamics of interest. The presence or absence of the *RL* approximated model is purely arbitrary and does not influence the fitting between the numerical and experimental frequency responses to which the next chapter aims.

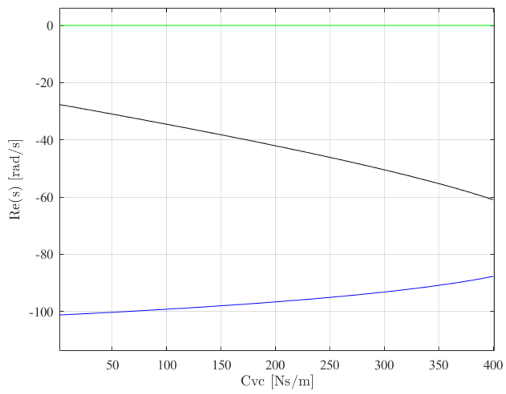

Figure 3.5: Variation of the real part of the poles of voice coil system with increasing electromagnetic damping.

However, the electrical equation will not be eliminated here and in the continuation of the thesis. This is because the modeling complexity of the voice coil was one of the last to be analyzed in this work. Furthermore, during experimental identifications, the system was excited by input voltage. Therefore in the numerical simulations it has been tried to replicate this condition. In order to do that, an equation capable of converting voltage into current, whatever it was, has been required.

3.2.4 Preliminary root locus analysis

In order to carry out a preliminary root locus analysis of the voice coil actuator, the values of parameters of interest (table 3.3) have been taken from previous thesis works ([19], [20]). Once a trial mass of $m_0 = 16.45Kg$ has been considered, the dynamic stability of the system can be studied as a function of the electromagnetic damping. This condition is fully equivalent to analyzing the system when damping is actively added by means of current control.

The actuator model so considered is characterized by 3 degrees of freedom, thus 1 real electrical pole and 1 pair of real mechanical poles can be computed. Note that the imaginary part is always zero since no stiffness property is present in the model. Thus, the root locus is useless ant the study of the variation of the real part of the poles with the damping is preferred, as shown in figure 3.5. It is worth to observe that even in case of zero electromagnetic damping, the system if always dynamically stable. Hence, the voice coil introduces no instability into the system, but on the contrary it contributes to the stabilization of the dynamic measuring device.

$L_{vc}[mH]$	$R_{vc}[\omega]$	$c_{vc}[Ns/m]$	$K_m[N/A]$	$m_0[Kg]$
11.1	1.43	207	25	16.45

Table 3.3: Voice coil parameters.

3.3 Dynamic measuring device

The dynamic measuring device consists mainly of a suspended part and no-suspended part connected by means of springs elements. In particular, the former is also called *sprung mass* while the latter is referred as *unsprung mass* since it is attached to the stator.

Referring to the figure 2.12, it is possible to note that spring elements are lighter and less stiff that the massive and rigid suspended and no-suspended parts for sure. From a mechanical point of view, it means that the natural frequencies associated to the vertical oscillation modes, which involve a relative motion between sprung and unsprung mass, are much lower if compared to the internal structural vibrations of each components. In the general scheme of the project, just the vertical dynamics is of interest since it is involved in passenger comfort analysis. This is why the dynamic measuring device can be modelled as a 2-DOFs mechanical system, as depicted in figure 3.6 where it is possible to identify the presence of two masses m_s and m_{us}. These values correspond to the masses of the sprung and unsprung parts respectively plus an half contribute (as a first approximation) of the spring elements for each. These two body are then connected by a massless spring-damper series k_s and c_s. Finally, the no-suspended part of the measuring device is attached to the stator via the elastic element k_{us} as well as an additional damper c_{us}

It is worth to observe that the unsprung stiffness k_{us} corresponds to equivalent value referred to the elastic contribution $K_{us,el}$ of a single unsprung spring element. The same can be said for the sprung stiffness k_s which can be thus computed starting from a value $K_{us,el}$ referred to a single sprung spring component. Since elastic elements form two series of eight parallel springs, the following relations can be written

$$k_{us} = 8 \times k_{us,el} \tag{3.43a}$$

$$k_s = 8 \times k_{s,el} \tag{3.43b}$$

The k_{us} and k_s terms can be computed numerically by considering the first deformation mode and tuning the obtained value via experimental tests.

The damping terms include the structural one related to the springs as well as the electromagnetic viscous friction c_{vc} introduce by the voice coil actuator. If the damping of a single unsprung and sprung element can be referred respectively as

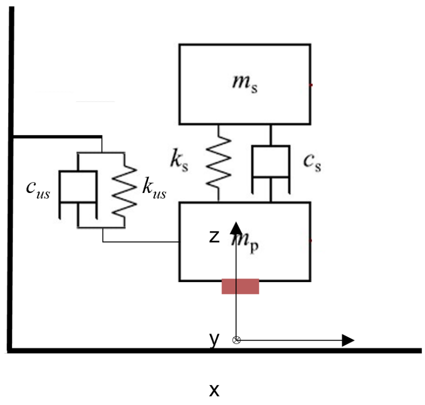

Figure 3.6: Schematic representation of the dynamic measuring device as a 2DOF mechanical system.

$c_{us,el}$ and $c_{s,el}$, then it results

$$c_{us} = 8 \times c_{us,el} \tag{3.44a}$$
$$c_s = 8 \times c_{s,el} + c_{vc} \tag{3.44b}$$

It is noteworthy that the electromagnetic friction is an order of magnitude greater than the equivalent damping of the springs.

3.3.1 Configuration space

The unknown quantities of the mechanical system under analysis can be identified in the displacement of the unsprung and sprung mass. Therefore, the configuration vector $\{q\}$ can be expressed as

$$\{q\} = \{z_{us}, z_s\}^T \tag{3.45}$$

In order to get the mechanical equations, it is possible to resort to the Lagrangian approach

$$\frac{d}{dt}\left(\frac{\partial \mathcal{L}}{\partial \dot{q}}\right) - \frac{\partial \mathcal{L}}{\partial q} + \frac{\partial \mathcal{F}}{\partial \dot{q}} = \mathcal{Q}_i \tag{3.46}$$

being $\mathcal{Q}$ the generalized i_{th} force, $\mathcal{F}$ the Rayleigh dissipation function and $\mathcal{L}$ the lagrangian operator, This latter is defined as the difference between the Kinetic $\mathcal{T}$ energy and the potential $\mathcal{U}_p$ energy, so that

$$\mathcal{L} = \mathcal{T} - \mathcal{U}_p \tag{3.47}$$

Once the Lagrangian equations are solved, a system of linear equations is automatically obtained. This is because, the relations 3.46 intrinsically refer to the hypotheses of small displacements, which is crucial to get a linear representation of the stiffness as well as damping contribution of the spring elements. On the other hand, the considerations on the linearity of the electromagnetic viscous friction are the same as previously discussed and, therefore, the same conclusions apply. Here, the effects of temperature and frequency are also negligible. Mechanical equations in the configuration space can be obtained by making the relation 3.46 explicit for each of the variable contained in the vector 3.45, operation that requires the computation of the energetic terms. The related easy expressions are shown below

$$\mathcal{T} = \frac{1}{2}m_{us}\dot{z}_s^2 + \frac{1}{2}m_{us}\dot{z}_{us}^2 \tag{3.48a}$$

$$\mathcal{F} = \frac{1}{2}c_s\left(\dot{z}_s - \dot{z}_{us}\right)^2 + \frac{1}{2}c_{us}\dot{z}_{us}^2 \tag{3.48b}$$

$$\mathcal{U}_p = \frac{1}{2}k_s\left(z_s - z_{us}\right)^2 + \frac{1}{2}k_{us}z_{us}^2 \tag{3.48c}$$

$$\mathcal{Q} = f_{us}z_{us} + f_{us}z_{us} \tag{3.48d}$$

being f_{us} and f_s the external forces acting respectively on the unsprung and sprung mass, including the active contribution of the voice coil.

By substituting equations 3.48 to the 3.46 and considering the relation 3.47, the mechanical equations finally can be written in the configuration space as

$$\begin{cases} m_{us}\ddot{z}_{us} \quad & +(c_s + c_{us})\dot{z}_us \quad -c_s\dot{z}_s \quad +(k_s + k_{us})z_{us} \quad -k_sz_s \quad = \quad f_{us} \\ \quad m_s\ddot{z}_s & -c_s\dot{z}_us \quad +c_s\dot{z}_s \quad -k_sz_{us} \quad +k_sz_s \quad = \quad f_s \end{cases} \tag{3.49}$$

or in a more compact matrix form as

$$[M]\{\ddot{q}\} + [C]\{\dot{q}\} + [K]\{q\} = \{f\} \tag{3.50}$$

where $[M]$ the mass matrix, $[C]$ the damping matrix, $[K]$ the stiffness matrix and $\{f\}$ the vector of external forces. All the expression of these operators can be consulted in the Appendix A.

3.3.2 Voice coil influence

It is interesting to neglect for a while the presence of the voice coil actuator and in general the effect of damping, dealing with the equivalent undamped system

$$[M]\{\ddot{q}\} + [K]\{q\} = \{f\} \tag{3.51}$$

If the homogeneous equation is considered and the eigenvalues problem is carried out, the following natural frequencies can be computed

$$\omega_n = \sqrt{\frac{1}{2}(\omega_s^2(1+\alpha) + \omega_{us}^2)\left[1 \pm \sqrt{1 - \frac{4\omega_s^2\omega_{us}^2}{(\omega_s^2(1+\alpha) + \omega_{us}^2)^2}}\right]} \tag{3.52}$$

being $\omega_{us} = \sqrt{k_{us}/m_{us}}$ the natural frequency of a single degree of freedom system with stiffness k_{us} mass, being $\omega_s = \sqrt{k_s/m_s}$ the natural frequency of a single degree of freedom system with stiffness k_s mass and $\alpha = m_s/m_{us}$ the ratio between the sprung and unsprung mass.

On the other end, the active contribution of the voice coil can be made explicit. In the mechanical domain, this interaction results in a pair of opposite force acting to the two body. Assuming that a positive value of the current generate a positive force on the sprung mass and a negative one on the unsprung mass, the system 3.49 can be rewritten as

$$\begin{cases} m_{us}\ddot{z}_{us} + (c_s + c_{us})\dot{z}_u s - c_s\dot{z}_s + (k_s + k_{us})z_{us} - k_s z_s + K_m i_{vc} = f_{us} \\ m_s\ddot{z}_s - c_s\dot{z}_u s + c_s\dot{z}_s - k_s z_{us} + k_s z_s - K_m i_{vc} = f_s \end{cases} \tag{3.53}$$

or in a more compact matrix form as

$$[M]\{\ddot{q}\} + [C]\{\dot{q}\} + [K]\{q\} + [K_m]i_{vc} = \{f\} \tag{3.54}$$

where $[K_m]$ is a 2×1 matrix that enter the contribution of the current in terms of force into mechanical equations. As written, the system 3.55 requires knowing the value of the current in order to be solved. Otherwise, it is necessary to introduce an appropriate electrical model thus moving to a multi-domain approach. The linear equation 3.34 discussed in the previous section is one of the possible solution that can be implement.
Note that the equivalent undamped system now results

$$[M]\{\ddot{q}\} + [K]\{q\} + [K_m]i_{vc} = \{f\} \tag{3.55}$$

The study of the poles require to specify if the electric current is a given input or not. This is an important requirement because in this case natural frequencies coincide with those of 3.52. In the contrary, the electric behaviour can introduce stiffness and damping and poles can reveal to have always a no-zero imaginary part.

3.3.3 State space representation

The vertical dynamics around the equilibrium configuration of the electromechanical dynamic measuring device can be modelled by resorting to the following system of differential linear equations

$$\begin{cases} \ddot{z}_{us} & = -\frac{(c_s+c_{us})}{m_{us}}\dot{z}_{us} + \frac{c_s}{m_{us}}\dot{z}_s - \frac{(k_s+k_{us})}{m_{us}}z_{us} + \frac{k_s}{m_{us}}z_s - \frac{K_m}{m_{us}}i_{vc} + \frac{f_{us}}{m_{us}} \\ \ddot{z}_s & = \frac{c_s}{m_s}\dot{z}_u s - \frac{c_s}{m_s}\dot{z}_s + \frac{k_s}{m_s}z_{us} - \frac{k_s}{m_s}z_s + \frac{K_m}{m}{}_s i_{vc} + \frac{f_s}{m_s} \\ \frac{di_{vc}}{dt} & = \frac{K_m}{\bar{L}_{vc}}\dot{z}_{us}) - \frac{K_m}{\bar{L}_{vc}}\dot{z}_s - \frac{R_{vc}}{\bar{L}_{vc}}i_{vc} + \frac{V}{\bar{L}_{vc}} \end{cases} \tag{3.56}$$

which can be also rewritten so that only first-order differential equations appear

$$\begin{cases} \dot{v}_{us} & = -\frac{(c_s+c_{us})}{m_{us}}\dot{z}_{us} + \frac{c_s}{m_{us}}\dot{z}_s - \frac{(k_s+k_{us})}{m_{us}}z_{us} + \frac{k_s}{m_{us}}z_s - \frac{K_m}{m_{us}}i_{vc} + \frac{f_{us}}{m_{us}} \\ v_{us} & = \quad \dot{z}_{us} \\ \dot{v}_s & = \quad \frac{c_s}{m_s}\dot{z}_u s - \frac{c_s}{m_s}\dot{z}_s + \frac{k_s}{m_s}z_{us} - \frac{k_s}{m_s}z_s + \frac{K_m}{m\ \ s}i_{vc} + \frac{f_s}{m_s} \\ v_s & = \quad \dot{z}_s \\ \frac{di_{vc}}{dt} & = \quad \frac{K_m}{L_{vc}}\dot{z}_{us} - \frac{K_m}{L_{vc}}\dot{z}_s - \frac{R_{vc}}{L_{vc}}i_{vc} + \frac{V}{L_{vc}} \end{cases} \tag{3.57}$$

The presence of spring elements allows for the computation of the values of $\{q\}$ and i_{vc} which satisfy the equilibrium. Generally, the linear actuator is required to balance the weight force, so that the oscillations refers to the following values

$$\begin{cases} z_{us,0} & = \frac{(m_{us}+m_s)g}{k_{us}} \\ z_{s,0} & = \quad 0 \\ i_{vc,0} & = \quad \frac{m_s g}{K_m} \end{cases} \tag{3.58}$$

It must be stressed that actually the system of equations 3.57 doesn't work if the unsprung spring is deformed of the quantity $z_{us,0}$ since strong non-linearities would appear. Thus, it is necessary a levitation force to restore the equilibrium position (i.e. the electrodynamical lift force).

The unknown variables can be collected in a state vector of the type

$$\{Z\}_{EM} = \{\dot{z}_{us}, z_{us}, \dot{z}_s, z_s, i_{vc}\}^T \tag{3.59}$$

while the input of the system can be identified in the parameters appearing in the vector

$$\{U\}_{EM} = \{f_{us}, f_s, V\}^T \tag{3.60}$$

corresponding to external forces applied respectively to the unsprung and sprung mass and the applied voltage.
Since the final goal of the whole project will be a passenger comfort analysis, the main output of interest can be identified in the acceleration, so that the output vector is

$$\{Y\}_{EM} = \{\ddot{z}_{us}\ddot{z}_s\}^T \tag{3.61}$$

Finally, the electromechanical model so obtained is a 3 *Input* - 2 *Output* system which allows for the following state-space representation

$$\begin{cases} \left\{\dot{Z}\right\}_{EM} & = [A]_{EM}\{Z\}_{EM} + [B]_{EM}\{U\}_{EM} \\ \{Y\}_{EM} & = [C]_{EM}\{Z\}_{EM} + [D]_{EM}\{U\}_{EM} \end{cases} \tag{3.62}$$

being $[A]_{EM}$ the dynamic matrix, $[B]_{EM}$ the input gain matrix, $[C]_{EM}$ the output gain matrix and $[D]_{EM}$ the direct link matrix. All the expression of these operators can be consulted in the Appendix A4.

The electric equation can also be neglected from the system 3.57 since it is rough approximated as has said in the previous chapter.

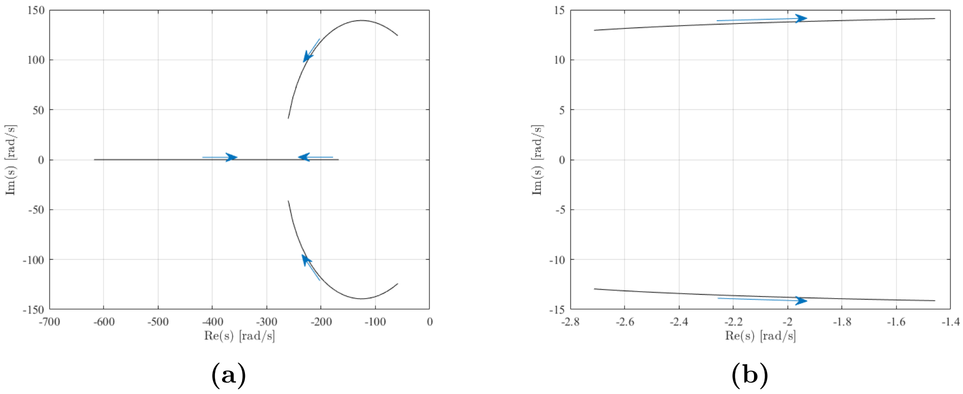

Figure 3.7: Root locus. a) Sprung mass mechanical poles. b) Unsprung mass mechanical poles.

3.3.4 Preliminary root locus analysis

In order to carry out a preliminary root locus analysis of the mechanical measuring device, the values of parameters of interest (table 3.4) have been taken from previous thesis works ([19], [20]). Once unsprung and sprung mass have been set respectively to $m_{us} = 3.73Kg$ $m_s = 16.45Kg$, the dynamic stability of the system can be studied as a function of the electromagnetic damping. This condition is fully equivalent to analyzing the system when damping is actively added by means of current control.

The dynamic stage so considered is characterized by 5 degrees of freedom, thus 1 real electrical pole and 2 pair of complex mechanical poles can be computed. These are shown in the root locus plot of figure 3.7. It is worth to say that mechanical poles have always no-zero imaginary part and even in case of zero electromagnetic and structural damping, the system is always dynamically stable. This result is not surprising since the dynamic measuring device is a mechanical damper and the geometry has been chosen so to balance the instability due to the electrodynamic suspension.

$k_{us}[N/m]$	$k_s[N/m]$	$c_{us}[Ns/m]$	$c_s[Ns/m]$	$m_{us}[Kg]$	$m_s[Kg]$
4216	2200	0	207	3.73	16.45

Table 3.4: Mechanical parameters.

3.4 Electrodynamical levitated electromechanical system

A permanent magnet rigidly attached to the dynamic measuring stage as well as a relative motion with respect to a guideway track make possible the electrodynamic levitation of the device itself. This is the case replicated in the experimental test bench described in *Chapter* 2.

The physics analyzed and described in previous sections allow the modelling of this particular condition. Under assumptions of small displacements around an equilibrium configuration, constant temperature, narrow frequencies window and considering a strong approximation that simplifies the electric behavior of voice coil,it is possible to obtain a linearization of the representation of the electrodynamic levitation electromechanical system by suitably combining the matrices collected in appendix A. Therefore, a state space representation is immediately available and a root locus analysis can be easily performed.

3.4.1 State space representation

The vertical dynamics around the equilibrium configuration of the electrodynamical levitated dynamic measuring device can be modelled by resorting to the following system of differential linear equations

$$
\begin{cases}
\frac{di_{1,d}}{dt} & = -\omega_{1,p} i_{1,d} + \omega i_{1,q} + \frac{\Lambda_0}{\gamma L_1} e^{\frac{-z_{PM,0}}{\gamma}} \dot{z}_{PM} \\
\frac{di_{1,q}}{dt} & = -\omega_{1,p} i_{1,q} - \omega i_{1,d} + \frac{\omega\Lambda_0}{\gamma L_1} e^{-\frac{z_{PM,0}}{\gamma}} z_{PM} - \frac{\omega\Lambda_0}{\gamma L_1} e^{-\frac{z_{PM,0}}{\gamma}} z_{in} \\
\frac{di_{2,d}}{dt} & = -\omega_{2,p} i_{2,d} + \omega i_{2,q} + \frac{\Lambda_0}{\gamma L_2} e^{-\frac{z_{PM,0}}{\gamma}} \dot{z}_{PM} \\
\frac{di_{2,q}}{dt} & = -\omega_{2,p} i_{2,q} - \omega i_{2,d} + \frac{\omega\Lambda_0}{\gamma L_2} e^{-\frac{z_{PM,0}}{\gamma}} z_{PM} - \frac{\omega\Lambda_0}{\gamma L_2} e^{-\frac{z_{PM,0}}{\gamma}} z_{in} \\
\dot{z}_{in} & = \quad \dot{z}_{in} \\
\ddot{z}_{us} & = -\frac{(c_s+c_{us})}{m_{us}} \dot{z}_{us} + \frac{c_s}{m_{us}} \dot{z}_s - \frac{(k_s+k_{us})}{m_{us}} z_{us} + \frac{k_s}{m_{us}} z_s - \frac{K_m}{m_{us}} i_{vc} + \\
 & \quad + \frac{f_{us}}{m_{us}} - \frac{2\Lambda_0}{\gamma m_{us}} e^{-\frac{z_{us,0}}{\gamma}} i_{1,d} + \frac{2\Lambda_0}{\gamma m_{us}} e^{-\frac{z_{us,0}}{\gamma}} i_{2,d} \\
\ddot{z}_s & = \quad \frac{c_s}{m_s} \dot{z}_u s - \frac{c_s}{m_s} \dot{z}_s + \frac{k_s}{m_s} z_{us} - \frac{k_s}{m_s} z_s + \frac{K_m}{m\ \ s} i_{vc} + \frac{f_s}{m_s} \\
\frac{di_{vc}}{dt} & = \quad \frac{K_m}{\bar{L}_{vc}} \dot{z}_{us} - \frac{K_m}{\bar{L}_{vc}} \dot{z}_s - \frac{R_{vc}}{\bar{L}_{vc}} i_{vc} + \frac{V}{\bar{L}_{vc}}
\end{cases}
\tag{3.63}
$$

which can be also rewritten so that only first-order differential equations appear

$$\begin{cases}
\frac{di_{1,d}}{dt} & = -\omega_{1,p}i_{1,d} + \omega i_{1,q} + \frac{\Lambda_0}{\gamma L_1}e^{\frac{-z_{PM,0}}{\gamma}}\dot{z}_{PM} \\
\frac{di_{1,q}}{dt} & = -\omega_{1,p}i_{1,q} - \omega i_{1,d} + \frac{\omega\Lambda_0}{\gamma L_1}e^{-\frac{z_{PM,0}}{\gamma}}z_{PM} - \frac{\omega\Lambda_0}{\gamma L_1}e^{-\frac{z_{PM,0}}{\gamma}}z_{in} \\
\frac{di_{2,d}}{dt} & = -\omega_{2,p}i_{2,d} + \omega i_{2,q} + \frac{\Lambda_0}{\gamma L_2}e^{-\frac{z_{PM,0}}{\gamma}}\dot{z}_{PM} \\
\frac{di_{2,q}}{dt} & = -\omega_{2,p}i_{2,q} - \omega i_{2,d} + \frac{\omega\Lambda_0}{\gamma L_2}e^{-\frac{z_{PM,0}}{\gamma}}z_{PM} - \frac{\omega\Lambda_0}{\gamma L_2}e^{-\frac{z_{PM,0}}{\gamma}}z_{in} \\
\dot{z}_{in} & = \quad \dot{z}_{in} \\
\ddot{z}_{us} & = -\frac{(c_s+c_{us})}{m_{us}}\dot{z}_{us} + \frac{c_s}{m_{us}}\dot{z}_s - \frac{(k_s+k_{us})}{m_{us}}z_{us} + \frac{k_s}{m_{us}}z_s - \frac{K_m}{m_{us}}i_{vc} + \\
& \quad + \frac{f_{us}}{m_{us}} - \frac{2\Lambda_0}{\gamma m_{us}}e^{-\frac{z_{us,0}}{\gamma}}i_{1,d} + \frac{2\Lambda_0}{\gamma m_{us}}e^{-\frac{z_{us,0}}{\gamma}}i_{2,d} \\
v_{us} & = \quad \dot{z}_{us} \\
\dot{v}_s & = \quad \frac{c_s}{m_s}\dot{z}_u s - \frac{c_s}{m_s}\dot{z}_s + \frac{k_s}{m_s}z_{us} - \frac{k_s}{m_s}z_s + \frac{K_m}{m\ _s}i_{vc} + \frac{f_s}{m_s} \\
v_s & = \quad \dot{z}_s \\
\frac{di_{vc}}{dt} & = \quad \frac{K_m}{\bar{L}_{vc}}\dot{z}_{us} - \frac{K_m}{\bar{L}_{vc}}\dot{z}_s - \frac{R_{vc}}{\bar{L}_{vc}}i_{vc} + \frac{V}{\bar{L}_{vc}}
\end{cases} \tag{3.64}$$

It is worth mentioning that the first four equations of the system 3.64 model the 2-branches electric parallel reproducing the electrodynamic suspension via linearized lumped-parameter approach. Furthermore, the perturbation introduced by irregularities of the guideway track are considered by the $\dot{z}_in$ term whose integral enters the system as a new unknown state variable z_in and which influences directly the dynamics both of the currents $i_{i,d}$ and $i_{i,q}$ and the unsprung mass. It should be recalled that in the previous system $\omega_{i,p}$ is the pole of the i_{th} branch of the electric parallel while ω is the characteristic frequency of the elecrodynamic force depending on the relative velocity between the dynamic measuring device and the track (i.e. the rotor speed of the experimental test bench). The system 3.64 is an integrated multi-domain model where the lift force, expressed as a combination of the quadrature component of the currents associated to the electric parallel, ensures the link between the electrodynamic suspension domain and the mechanical one; on the other hand, thanks to the voice coil constant, the interaction between the electric and mechanical domains become possible. Again, it must be stressed that the last equation related to an RL circuit can be neglected without lose of information detrimental for the experimental validation and identification of the model.

The equilibrium position $z_{us,0}$ is the one that let the unsprung springs to work around the rest condition. Moreover, the external excitements f_{us} and f_s don't include the weight forces acting on the two masses of the mechanical system as well as the mean value of the voltage V that allow the voice coil to balance the weight itself is not considered. Thus, oscillations refer to the equilibrium configuration.

The unknown variables can be collected in a state vector of the type

$$\{Z\} = \{i_{1,d}, i_{1,q}, i_{2,d}, i_{2,q}, z_{in}, \dot{z}_{us}, z_{us}, \dot{z}_s, z_s, i_{vc}\}^T \tag{3.65}$$

while the input of the system can be identified in the parameters appearing in the vector

$$\{U\} = \{\dot{z}_i n, f_{us}, f_s, V\}^T \tag{3.66}$$

corresponding to external forces applied respectively to the unsprung and sprung mass and the applied voltage.
The final goal of the whole project will be a passenger comfort analysis and the current control of the bench which can be carried out also numerically thanks to the integrated model just defined. Obviously, this requires an experimental validation that can be performed by comparing the frequency response functions defined as the ratio between accelerations and current. Therefore, the main output of interest can be identified in the following output vector is

$$\{Y\} = \{\ddot{z}_{us}\ddot{z}_s i_{vc}\}^T \tag{3.67}$$

Finally, the electrodynamical levitation electromechanical model so obtained is a 4 *Input* - 3 *Output* system which allows for the following state-space representation

$$\begin{cases} \left\{\dot{Z}\right\} & = [A]\{Z\} + [B]\{U\} \\ \{Y\} & = [C]\{Z\} + [D]\{U\} \end{cases} \tag{3.68}$$

being $[A]$ the dynamic matrix, $[B]$ the input gain matrix, $[C]$ the output gain matrix and $[D]$ the direct link matrix. All the expression of these operators can be consulted in the Appendix A5.

3.4.2 Preliminary root locus analysis

In order to carry out a preliminary root locus analysis of the electrodynamical levitated electromechanical system, the values of parameters of interest (table 3.2, 3.3 and 3.4) have been taken from previous thesis works ([19], [20]). Once unsprung and sprung mass have been set respectively to $m_{us} = 3.73Kg$ $m_s = 16.45Kg$, the dynamic stability of the system can be studied both as a function of the guideway track velocity and the electromagnetic damping, i.e. the two conditions which, according to what has been said previously, mainly affect the dynamic stability of the system.

The integrated multi-domain model so considered is characterized by 10 degrees of freedom, thus 2 pair of complex conjugated electrodynamic suspension poles, 1 pole related to the irregularities state variable, 1 electric pole associated to the electric actuator and 2 pair of complex mechanical poles can be computed. In particular,in figure 3.8a sprung and unsprung poles are plotted for increasing speed values and for a damping coefficient equal to 207Ns/m.

The root locus of the unsprung mass is placed at higher real part values. It is

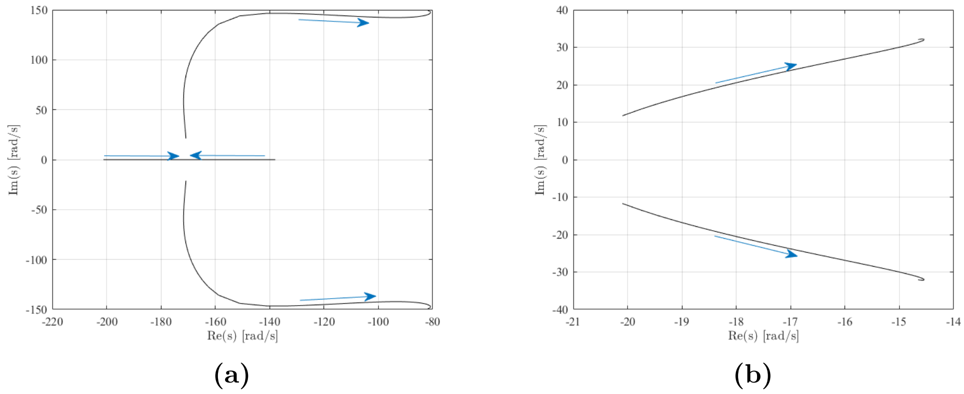

Figure 3.8: Root locus. a) Sprung mass mechanical poles. b) Unsprung mass mechanical poles.

interesting to note that the trend is quite similar to figure 3.3 but it seems to be rigidly shifted on the left. This is due to the presence of electromagnetic as well as structural damping. Practically, the dynamics of the unsprung mass turns out to be stable in the entire speed range of interest. On the other hand, the sprung mass has imaginary natural poles without negative real part. These have an higher modulus if compared with the same of the not unsprung mass. This is because the measuring device under analysis is a mechanical damper that stabilized the suspended body itself. In both case, the increasing of speed pushes the real part towards the imaginary axis.

In figure 3.9 the mechanical poles dependence on the (electromagnetic) damping is reported for a given velocity of 500rpm (24.61m/s). It should be mentioned that as the $c_[vc]$ coefficient increases, the real parts of the poles of the unsprung mass become greater in modulus with a positive effect for the dynamic stability. At the same time, the poles of the sprung mass take on a non-zero real part which tends to cross the imaginary axis as damping increases. Then, the dynamic stabilization of the system appear to be not trivial since the presence of a damper has both a positive and negative effect on the dynamic behaviour or the unsprung and sprung mass respectively. Therefore, an optimal damping c_opt value should be exist.

3.5 State observers

A state observer is a mathematical object capable of providing an estimate of the states of interest of a plant, usually running in parallel with the real system in a microprocessor [29]. The importance of an observer is linked to the possibility of

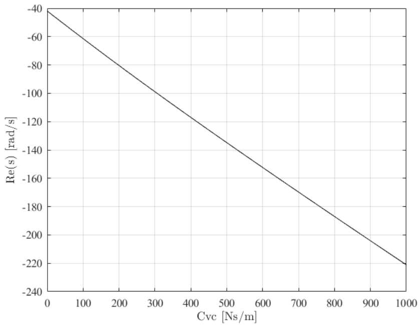

(a)

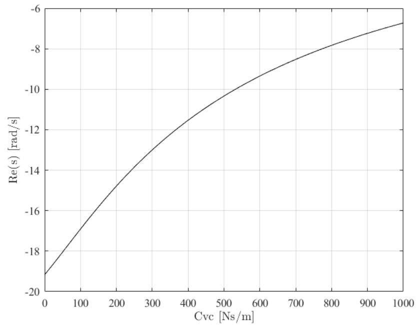

(b)

Figure 3.9: Variation of the real part of the poles of the integrated system with increasing electromagnetic damping.. a) Sprung mass mechanical pole. b) Unsprung mass mechanical pole.

having a reference against which to evaluate the error within a control system and introduce active signals directly proportional to the estimated states into the plant. In this sense, the term *model-based control* can be used.

The mathematical relations that rule the behaviour of a state observer can be derived starting from the state space representation matrices ($[A]$, $[B]$, $[C]$ and $[D]$) of the system analyzed. It is clear that if the model related to the plant is correct, the state observer give a true computation of the state variables $\{Z\}$ of interest. Generally, the identification of the real system is affected by a certain degree of approximation. This is why the available state space matrices ($[A]_o$, $[B]_o$, $[C]_o$ and $[D]_o$) are affected by uncertainty and the estimate of state variables $\{\hat{z}\}$ is consequently not totally correct. This is what happens for the case under study.

In order to increase the efficiency of a state observer, the continuous comparison between the real measured variables $\{ Y\}$ and the estimated numerical ones $\{\hat{Y}\}$ is useful. Thus a gain matrix $[K]_o$ is introduced which multiplies the error committed by correcting the equation of states at each cycle, so that it results

$$\begin{cases} \left\{\hat{Z}(t+1)\right\} & = [A]_o \left\{\hat{Z}(t)\right\} + [B]_o \{U(t)\} + [K]_o(Y(t) - \hat{Y}(t-1)) \\ \left\{\hat{Y}(t)\right\} & = [C]_o \left\{\hat{Z(t)}\right\} + [D]_o \{U(t)\} \end{cases} \tag{3.69}$$

being $\hat{U}\}$ the usual input vector of the plant. Let note that the system 3.69 contains an implied discretization since the model should be implemented in a microcontroller which works in a finite way.

An example useful to understand how a state observer works is schematized in figure **??** [29]. Here the *regulator* definition refers to the fact that the variable $\{\hat{Z}\}$ is used to derive an active control signal for the plant by means of $[K]_c$ and $[B]_c$

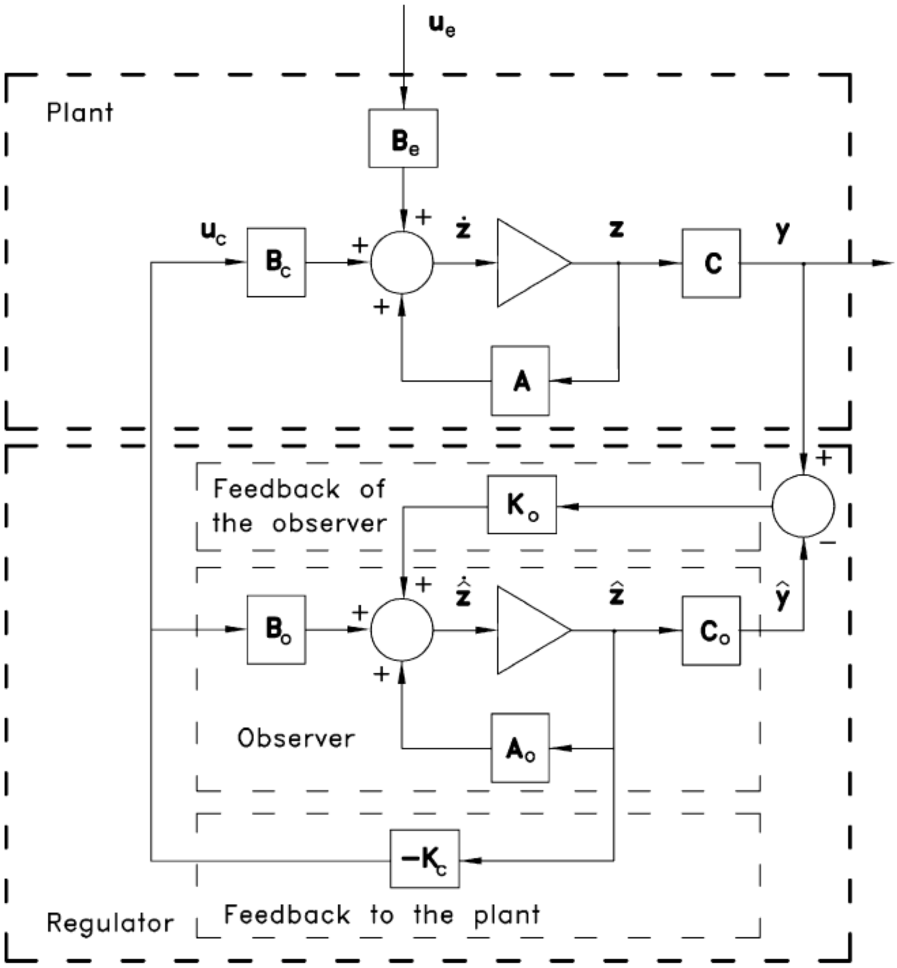

Figure 3.10: Schematic representation of a plant and a regulator working in parallel.

matrices. Moreover, it should be noted that the system represented doesn't have a direct link relation between input and output signals. So, this figure is purely introduced to show the working principle of an observe
Finally, the observability condition must be satisfied. This implies that the observability matrix defined as

$$[O] = \left[C_o^T, \quad A_o^T C_o^T \left(A_o^T \right)^2 C_o^T, \quad \cdots, \quad \left(A_o^T \right)^{n-m} C_o^T \right]^T \tag{3.70}$$

where n is the number of state variables and m is the number of outputs, must have maximum rank (i.e. rank equal to n).

For the case under analysis, the definition of a suitable observer can be used to estimate the relative velocity between the sprung and unsprung mass

$$\Delta v = v_s - v_{us} \tag{3.71}$$

In this way, it could be possible to act on the real plant by giving a force proportional $f_{c,a}$ to the speed (i.e. a damping force) that allow the electrodynamical levitated electromechanical device to work in the optimal dynamic condition. This objective can be achieved if the system is current controlled and if the active value is set to be

$$i_{c,a} = \frac{(c_{opt} - c)\Delta\hat{v}}{K_m} \tag{3.72}$$

according to the equation 3.27. Let note that this value can be positive or negative depending on the difference between the wanted damping and the actual one.
In the following sections the main state observers studied are discussed.

3.5.1 RL observer

It should be recalled that in the equation 3.34 only the state variables i_{vc} and Δv appear as well as the input V. Since in the experimental test bench, the current $\bar{i}_{vc}$ and voltage $\bar{V}$ values are both measured, it is possible to give an immediate estimate of the relative velocity $\Delta\hat{v}$ by means an RL type observer. Strictly speaking, the latter cannot be defined a state observer since it is a simple algebraic equation.

Then, the RL observer model can be written as

$$\Delta\hat{v} = \frac{1}{K_m}\left(\bar{V} - \bar{L}_{vc}\frac{d\bar{i}_{vc}}{dt} - R_{vc}\bar{i}_{vc}\right) \tag{3.73}$$

It should be stressed that the previous equation has been derived starting from a strong approximation and linearization of the real complex electric behaviour of the voice coil. Moreover even a correction gain matrix $[K]_0$ is not present in the model. So the RL observer could not properly work since it has been built starting from a wrong model without considering a real-time comparison between the real and estimated state variables. On the other hand, such an observer is really simple and the measuring signals related to the accelerations of sprung and unsprung mass are not required in the equation 3.73. If both inductance $\bar{L}_{vc}$ and resistance $\bar{L}_{vc}$ as well as the computation of the discrete time-derivative of the current are accurate, a *sensorless model-based control* will be available. These aspects make the RL observer worth studying solution.

3.5.2 Standard Kalman filter

The Kalman filter is a data fusion algorithm which is able to predict the behaviour of a real plant by combining the information coming from the numerical model with those obtained from experimental measurements. A Kalman filter estimates the **p**robability **d**ensity **f**uncion (**PDF**) of the state variable rather than its discrete value. In particular, it is assumed that PDFs are of Gaussian type so that the computation requires to know the variances and covariances. The appropriate tuning of these quantities allows the Kalman filter to improve the approximation of the state variables of interest. From a mathematical point of view, it takes the form of a state observer [30].

Generally, the behaviour of a real plant differs from that of numerical model because of the presence of some errors in:

1. State space matrices;
2. Measurements;
3. Computation process.

Thus, the state space representation of the discrete real system can be written in a more correct way as

$$\begin{cases} \{Z(t+1)\} &= [A]_o\{Z(t)\} + [B]_o\{U(t)\} + [Q(w)] \\ \{Y(t)\} &= [C]_o\{Z(t)\} + [D]_o\{U(t)\} + [R(v)] \end{cases} \tag{3.74}$$

being $[Q(w)]$ and $[R(v)]$ the covariance matrices related to the noise on process and measurements respectively. A Kalman filter algorithm assumes that noises are of white type and uncorrelated with each other. So, $[Q(w)]$ and $[R(v)]$ appear as pure diagonal matrices whose i_{th} element is the square of the noise quantity w_i and v_i associated to the i_{th} state and output respectively.

For the case under study, the kalman filter can be modelled as

$$\begin{cases} \left\{\hat{Z}(t+1)\right\} &= [A]\left\{\hat{Z}(t)\right\} + [B]\{U(t)\} + [K]_{kf}(\{Y(t)\} - \{\hat{Y}(t)\}) \\ \left\{\hat{Y}(t)\right\}_{kf} &= [C]_o\left\{\hat{Z(t)}\right\} \end{cases} \tag{3.75}$$

where $[A]$ and $[B]$ are the dynamic and input gain matrices related to the electrodynamical levitated eletromechanical system as reported in Appendix A4 and $[C]_o$ the output gain matrix of the observer which gives as outputs both the estimated relative velocity $\Delta\hat{v}$ and the current $\hat{i}_{vc}$ collected in the vector $\{Y\}_{kf}$, The $[K]_{kf}$ term is the Kalman gain matrix which can be derived by means of the minimization of the following cost function

$$J_{cost} = \sum_{k=1}^{\infty}\left(\{Z(k)\}^T[Q(w)]\{Z(k)\} + \{U(n)\}^T[R(v)]\{U(k)\}\right) \tag{3.76}$$

The ratio between the w_i and v_i quantities determines how much the filter can trust the measurements rather than the numerical model: this is because the updating of the state variables in the algorithm foresees a fusion or product between the Gaussian of the estimated variable and that of the measurement signals.

The output vector $\{\hat{Y}\}$ of the state space system 3.75 can be expressed as a function of the state variables and the input vectors

$$\begin{cases} \left\{\hat{Z}(t+1)\right\} & = [A]\left\{\hat{Z}(t)\right\} + [B]\left\{U(t)\right\} + [K]_{kf}(Y(t) - [C]\left\{\hat{Z}(t)\right\} - [D]\left\{\hat{U}(t)\right\}) \\ \left\{\hat{Y}(t)\right\}_{kf} & = [C]_{kf}\left\{Z\hat{(t)}\right\} \end{cases} \tag{3.77}$$

being $[C]$ and $[D]$ are the output gain and the direct link matrices related to the electrodynamical levitated eletromechanical system as reported in Appendix A4. By rearranging the system, it is possible to write that

$$\begin{cases} \left\{\hat{Z}(t+1)\right\} & = ([A] - [K]_{kf}[C])\left\{\hat{Z}(t)\right\} + ([B] - [K]_{kf}[D])\left\{U(t)\right\} \\ \left\{\hat{Y}(t)\right\}_{kf} & = [C]_{kf}\left\{Z\hat{(t)}\right\} \end{cases} \tag{3.78}$$

By introducing $[A]_{kf}$ and $[B]_{kf}$ matrices so that it results

$$[A]_{kf} = [A] - [K]_{kf}[C] \tag{3.79a}$$
$$[B]_{kf} = [B] - [K]_{kf}[D] \tag{3.79b}$$

the Kalman filter observer equations can be finally obtained

$$\begin{cases} \left\{\hat{Z}(t+1)\right\} & = [A]_{kf}\left\{\hat{Z}(t)\right\} + [B]_{kf}\left\{U(t)\right\} \\ \left\{\hat{Y}(t)\right\}_{kf} & = [C]_{kf}\left\{Z\hat{(t)}\right\} \end{cases} \tag{3.80}$$

being $[A]_{kf}$ the Kalman dynamic matrix, $[B]_{kf}$ the Kalman input gain matrix and $[C]_{kf}$ the Kalman output gain matrix. The state observer so the defined is a 4 *Input* - 2 *Output* system of order 10.

The Kalman filter thus obtained is a standard result of the Kalman filtering theory. It is an algorithm able to manage the errors in the numerical models providing a better estimate of the relative speed compared to the same calculated by means of the RL observer. Moreover, a rejection of the measured noise is inherently carried out. On the other hand, the presence of both electric and mechanical disturbances can't be detected since the Kalman filter relies on a rigid numerical model that is defined since the beginning. For the same reason, it should be noted that state space matrices are computed for a given track velocity, so that the estimation during transients which involve a variation of the relative speed between pod and guideway can lead to bad estimation.

3.5.3 Extended Kalman filter

An extended version of the Kalman filter can be obtained by introducing in the state space model an other state variable together with its characteristic equation

$$\begin{cases} \{Z(t+1)\} & = [A]_o \{Z(t)\} + [A]_{aug} i(t)_{aug} + [B]_o \{U(t)\} + [Q(w)] \\ \{Y(t)\} & = [C]_o \{Z(t)\} + [C]_{aug} i(t)_{aug} + [D]_o \{U(t)\} + [R(v)] \\ \frac{d}{dt} i_{aug}(t) & = i_{aug}(t) + w_{aug} \end{cases} \tag{3.81}$$

being i_{aug} the so-called augmented state variable with characteristic noise w_{aug} and $[Q(w)]$ and $[R(v)]$ the covariance matrices related to the noise on process and measurements respectively in the sense described in previous section. The $[A]_{aug}$ and $[C]_{aug}$ terms are the column vectors of the $[A]$ and $[C]$ operators respectively, precisely those referred to the current state. In fact, these can be expressed as

$$[A]_{aug} = \{A\}_{i,10} \qquad i = 1 \ldots 10 \tag{3.82a}$$

$$[C]_{aug} = \{C\}_{i,10} \qquad i = 1 \ldots 10 \tag{3.82b}$$

The variable i_{aug} is an augmented state which enter the electrodynamical levitated electromechanical system as a current and whose dynamics is characterized by an asymptotic exponential trend. In this way, the i_{aug} can simulate all disturbances and errors of the models as well as predict sudden disturbances acting on the system. By properly tuning the noise w_{aug}, the velocity of this prediction can be improved.
It is interesting to observer that an augmented state that enter the main system in terms of force lead to an observable system. This explain why $[A]_{aug}$ and $[C]_{aug}$ has been obtain considering the elements which multiply the current state.
The system 3.84 can be rearranged so that the i_{aug} term is included in a new extended state vectors

$$\begin{cases} \left\{ \begin{matrix} \{\dot{Z}\} \\ \left\{\frac{d}{dt} i_{aug}\right\} \end{matrix} \right\} & = \begin{bmatrix} [A]_o & [A]_{aug} \\ 0 & 1 \end{bmatrix} \left\{ \begin{matrix} \{Z(t)\} \\ \{i(t)\}_{aug} \end{matrix} \right\} + [B]_o \{U(t)\} + [Q(w), w_{aug}] \\ \{Y(t)\} & = \begin{bmatrix} [C] & [C_{aug}] \end{bmatrix} \left\{ \begin{matrix} \{Z(t)\} \\ \{i_{aug}(t)\} \end{matrix} \right\} + [D]_o \{U(t)\} + [R(v)] \end{cases} \tag{3.83}$$

By introducing a more compact notation, it results

$$\begin{cases} \{Z(t+1)\} & = [A]_d \{Z(t)\}_d + [B]_o \{U(t)\} + [Q(w)]_d \\ \{Y(t)\} & = [C]_d \{Z(t)\}_d + [D]_o \{U(t)\} + [R(v)] \end{cases} \tag{3.84}$$

Since the extended state variable takes into account the effect of perturbation (included forces), it is possible to reduce the size of the input vector considering only the voltage applied. Then, by introducing the submatrices

$$[B]_d = \{B\}_{i,4} \qquad i = 1\dots 10 \tag{3.85a}$$
$$[D]_d = \{D\}_{i,4} \qquad i = 1\dots 10 \tag{3.85b}$$

it is possible to write

$$\begin{cases} \{Z(t+1)\}_d & = [A]_d \{Z(t)\}_d + [B]_d \{U(t)\}_d + [Q(w)]_d \\ \{Y(t)\}_d & = [C]_d \{Z(t)\}_d + [D]_d \{U(t)\}_d + [R(v)]_d \end{cases} \tag{3.86}$$

where $\{U(t)\}_d$ and $[R(v)]_d$ take into account only the voltage input and, thus, they contain the usual elements that ensure the voltage to enter the system.

Ones defined that the augmented system 3.86 is observable, the standard Kalman algorithm procedure can be applied, but in this case with an augmented variable that take into account all the perturbation. This is why it is possible to refers the Extended Kalman filter only to the electromechanical subsystem. Thus, by substituting to $[A]_o, [B]_o, [C]_o, and[D]_o$ matrices the $[A]_{EM}, [B]_{EM}, [C]_{EM}, and[D]_{EM}$ in Appendix A.3 respectively and introducing the extended variable in the same why done before, the following system can be written

$$\begin{cases} \left\{\hat{Z}(t+1)\right\}_d & = [A]_{EM,d} \left\{\hat{Z}(t)\right\}_d + [B]_{EM,d} \{U(t)\}_d + \\ & = +[K]_{ekf}(Y(t)_d - [C]_{EM,d} \left\{\hat{Z}(t)\right\}_d - [D]_d \left\{\hat{U}(t)\right\}_d) \\ \left\{\hat{Y}(t)\right\}_{ekf} & = [C]_{ekf} \left\{\hat{Z(t)}\right\}_d \end{cases} \tag{3.87}$$

being $[C]_{ekf} and \left\{\hat{Y}(t)\right\}_{ekf}$ the $[C]_{kf} and \left\{\hat{Y}(t)\right\}_{kf}$ terms introduce in the previous section but with a different subscript to underlinde that this system is referred to an Extended Kalman Filter; $[A]_{EM,d}, [B]_{EM,d} and [C]_{EM,d}$ are the augmented electromechanical matrices As the previous case, the relative velocity and the current are the output of the observer and the extended Kalman gain can be computed as the minimization of the cost function so defined

$$J_{cost} = \sum_{k=1}^{\infty} \left(\{Z(k)\}_d^T [Q(w)]_d \{Z(k)\}_d + \{U(n)\}_d :^T [R(v)]_d \{U(k)\}_d \right) \tag{3.88}$$

With the same procedure seen before, it is possible to express the system 3.87 in a more compact form by collecting the different terms dealing finally with a system of the type

$$\begin{cases} \left\{\hat{Z}(t+1)\right\}_d & = [A]_{ekf} \left\{\hat{Z}(t)\right\}_d + [B]_{ekf} \{U(t)\}_{ekf} \\ \left\{\hat{Y}(t)\right\}_{ekf} & = [C]_{ekf} \left\{\hat{Z(t)}\right\}_d \end{cases} \tag{3.89}$$

being

$$[A]_{ekf} = [A]_{EM,d} - [K]_{ekf}[C]_{EM,d} \tag{3.90a}$$
$$[B]_{ekf} = [[B]_{EM,d} - [K]_{ekf}[D]_d, [K]_{ekf}] \tag{3.90b}$$
$$\tag{3.90c}$$

and the state vectors

$$\left\{\hat{Z}(t)\right\}_d = \{\dot{z}_{us}, z_{us}, \dot{z}_s, z_s, i_{vc}, i_{aug}\}^T \tag{3.91a}$$
$$\left\{\hat{U}(t)\right\}_{ekf} = \{\{\hat{U}(t)\}_d, \{Y(t)\}_d, \}^T = \{V_{plant}, \ddot{z}_{us,plant}, \ddot{z}_{s,plant}, i_{vc,plant}\}^T \tag{3.91b}$$
$$\left\{\hat{Y}(t)\right\}_{ekf} = \{\Delta v_{extimated}, i(t)_{extimated}\}^T \tag{3.91c}$$

Chapter 4

Experimental measurements and identification

The prediction of numerical models can be affected by some uncertainties. This is generally because building a theoretical representation of the phenomenon has a need for the introduction of various simplifying hypothesis. If on the one hand these allow to obtain linear and generalizable solutions, on the other hand they can also lead to over neglect the effect of complex physics.
In order to improve the reliability of a numerical model, a suitable idea can be that of comparing theoretical results with experimental evidences of prototypes. In this sense, it could prove crucial to calculate the **F**requency **R**esponse **F**unction (**FRF**) which is a full-fledged identity card of a system able to describe its behaviour in the frequency domain.

Based on these observations, in this *Chapter* the model of the electrodynamical levitated system under analysis is identified and experimentally validated. This has been required setting up a working measuring strategy, wondering about the most convenient input excitation signals and focusing on the output of interest. In addition, the identification of the main parameters that make up the numerical equations is discussed as these have proved useful for obtaining first attempt values from which to start for the curve fitting of the frequency response functions.
In such a context, this *Chapter* can be considered as the meeting point between the experimental measurements carried out using the test bench presented in *Chapter* 2 and the numerical simulations of the models described in *Chapter* 3.

4.1 Experimental measurements

Experimental measurements require a well-defined action plan, from setting up the equipment necessary to let the test bench work properly to the definition of signal processing methods and extraction of the information of interest. This is why, in this section the attention is only focused on the experimental side of the identification procedure.

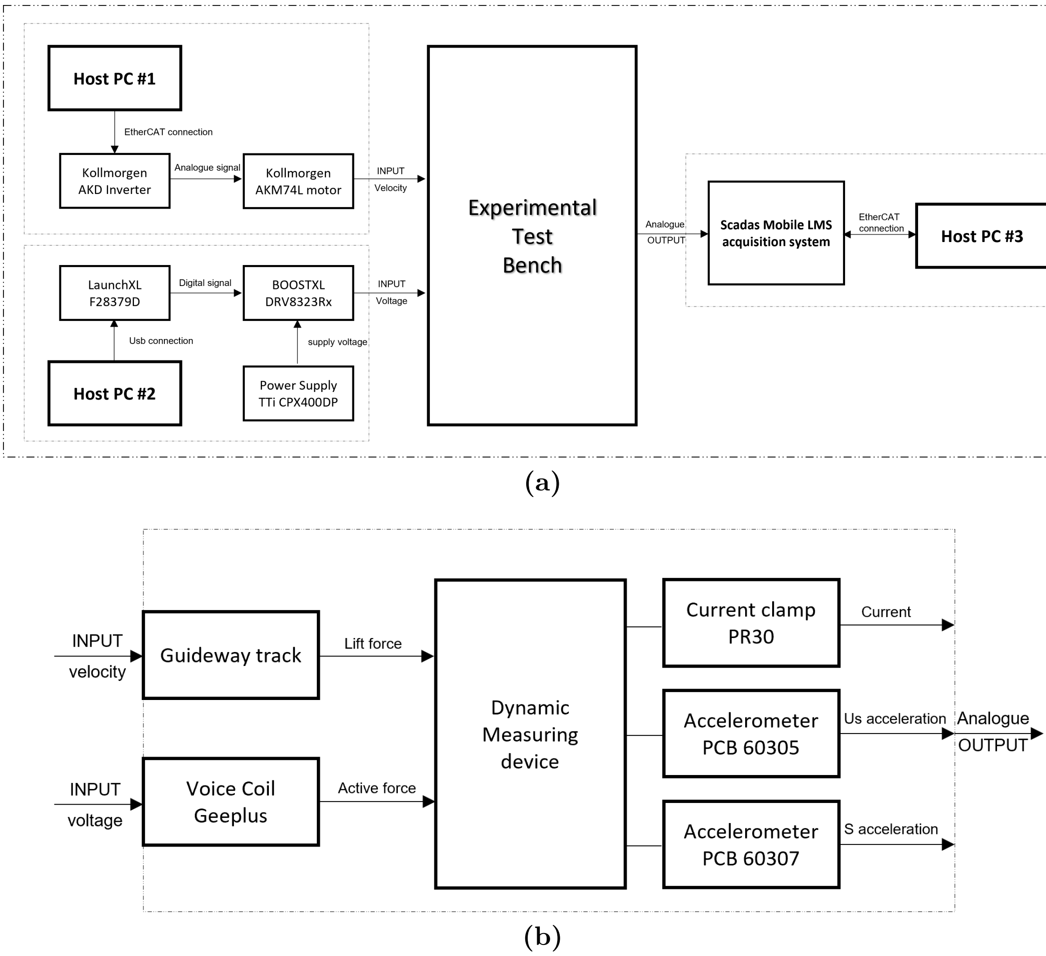

Figure 4.1: Schematic representation of the measuring and open loop control strategy. a) General measuring and control chain. b) Zoom-in on the dynamic measuring device.

4.1.1 Measuring and control strategy

A schematic diagram of the measuring and control strategy adopted for the case study is shown in figure 4.1.

The number of *Host PCs* needed from the set up is equal to three, but in practice the monitoring of both the electric motor and the voice coil has been entrusted to a single computer.

The *Host PC* n.1 is responsible for controlling by means of *Kollmorgen WorkBench 2.10.0.7363* the *Kollmorgen AKD* inverter which in turn drives the *Kollmorgen AKM74L* motor. The working speed range exploited goes from 450 up to $600rpm$. In order to reduce the time test, an acceleration of $5rpm/s$ and a deceleration of $2rpm/s$ have been established. The latter is smaller than the former since the presence of a drag force helps to brake the copper track. It is worth to say that lower velocities have not been considered because of the extreme reduction of the equilibrium air gap needed to balance the weight force of the dynamic measuring device. Furthermore, this decrease in lift force is accompanied by an increase in drag force and, consequently, in energy losses and in temperature, so that the experimental validation of the electrodynamic suspension could have been invalidated. On the other hand, higher speeds have not been imposed for safety purpose since the design rotational velocity of the copper ring is about $750rpm$.

The *Host PC* n.2 manage the input signals which excite the dynamic device starting from a constant voltage power supply. This task is fulfilled by means of *LaunchXL-F28379D Texas instrument*, the microprocessor of the measuring chain, and implies also the prior building and deploying of a script program in *C language*. To be more precise, all codes have been written via Simulink®, while the translation into the language required by the launchpad was done thanks to special extensions.

The *Host PC* n.3 is connected to *Scadas Mobile LMS acquisition system* via *EtherCat communication*. Thank to the *Simcenter TestLab Signature acquisition* interface, it can receive and save the desire output signals.

4.1.1.1 Open loop voltage control

During experimental tests, the dynamic stage has been controlled in open loop by imposing a reference voltage value. All the input signal generation phases which lead from the power supply to the excitation of the device itself have been managed by *LaunchXL-F28379D* instrument at the working frequency of $f_{LP,s} = 20KHz$.

In order to enforce the desired voltage value, a power supply and a system capable of manipulating this constant power signal have been required. The first task has been fulfilled by implementing in the test bench a *TTi CPX400DP* Power Supply with constant voltage of $12V$ and maximum released current of $6.5A$. These values are justified respectively by considering previous experimental activities and

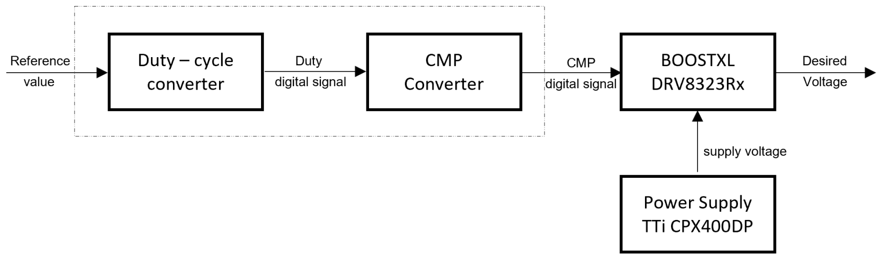

Figure 4.2: Block diagram related to the conversion of the reference voltage value into the CMP input.

the maximum admissible current of voice coil windings.

On the other hand, it is clear that a power supply alone does not allow to control a linear actuator as it is able to give a constant voltage value and a current which will consequently varies according to the impedance of the circuits of the chain. This is why a *BOOSTXL-DRV8323Rx* has been introduced between the voice coil and the launchpad. This is basically an extension module of the *LaunchXL-F28379D* that outputs the desired voltage signal by means of an *H - bridge*. Therefore, the launchpad should provide the related *Duty - cyle* properly converted into **c**ounter co**mp**ar (CMP) signal.
Figure 4.2 schematizes the main steps in a sequential manner for a better understanding. It is worth to note that the wanted voltage value V is used to calculate the time the *H - bridge* switches are closed with respect of the characteristic period of the so called ePWM module (i.e. CMP input). In particular, it results

$$CMP = \left(V\frac{100}{24} + 50\right)\frac{PWM_{CounterPeriod}}{100} \tag{4.1}$$

where 24V is twice the value of 12V given by the power supply. This is because the *H - bridge* works in a double legs way so that even negative voltage can be provided. Consequently, if the switches are closed for half of the characteristic period then the voltage signal is zero. This explains the presence of "50" in the previous formula.
The result obtained from 4.1 let the *BOOSTXL-DRV8323Rx* compute the **p**ulse-**w**idth **m**odulation (**PWM**), that is the square-type signal whose mean value is equal to the desired voltage. Anyway, the part of the script program that allows PWM signal calculation was derived from previous work ([18], [19], [20]).

Finally, experimental output acquired from the test bench are the results of a series of input sent to the voice coil and managed via an open loop voltage control.

4.1.1.2 Input signals

The script program executed by the launchpad has been compiled so that the dynamic measuring device could receive three fundamental input:

1. Load reliever signal;
2. Chirp signal;
3. Sinusoidal signal.

All listed input are voltage analogue excitations, as discussed in the previous subsection.

The load reliever is a step input signal with final value V_0 which balance the weight force of the sprung mass. Numerically this is

$$V_0 = \frac{1}{R_{vc}} \left(\frac{m_s g}{K_m} \right) \tag{4.2}$$

From a theoretical point of view, feeding the voice coil with such a voltage should indifferently guarantees the suspension of the sprung body for each offset. In this sense, the equilibrium position seems to be indeterminate. Experimentally activities have refuted this observation since the mechanical constant of the voice coil is actually lightly-dependent on the offset so that the equilibrium position depends on the combination of both the final value of the step signal and the local value assumed by Km.

On the other hand, in the static equations also the spring elements must be involved. This fact has made the estimation of the load reliever not foregone since the deformation of the springs introduces auxiliary forces which contribute to the weight balancing. As a consequence, the sprung mass can be lifted for voltage values smaller than the theoretical expected one; larger values may push the body slightly away from the wanted position. In both case, the springs are pre-stressed and the offset changes resulting in a system which doesn't work around its equilibrium configuration. Therefore, it can't be modelled by resorting to linear equations of *Chapter* 3 without introducing errors.

Experimentally, a value of $10.5V$ has been imposed. This is an approximation by excess of the theoretical expected voltage V_0 since it wants to take into account for the increasing of the resistance R_{vc} due to the Joule effect.

The chirp signal is a sinusoidal-type voltage signal $V_{chirp}(t)$ whose frequency increase linearly over time so that it results

$$V_{chirp}(t) = V_{chirp,0} sin(2\pi \alpha_{chirp} t^2) \tag{4.3}$$

being $V_{chirp,0}$ the amplitude of the input and α_{chirp} the coefficient of time growth of the frequency

$$\alpha_{chirp} = \frac{f_{chirp,max} - f_{chirp,min}}{\Delta t_{chirp}} \tag{4.4}$$

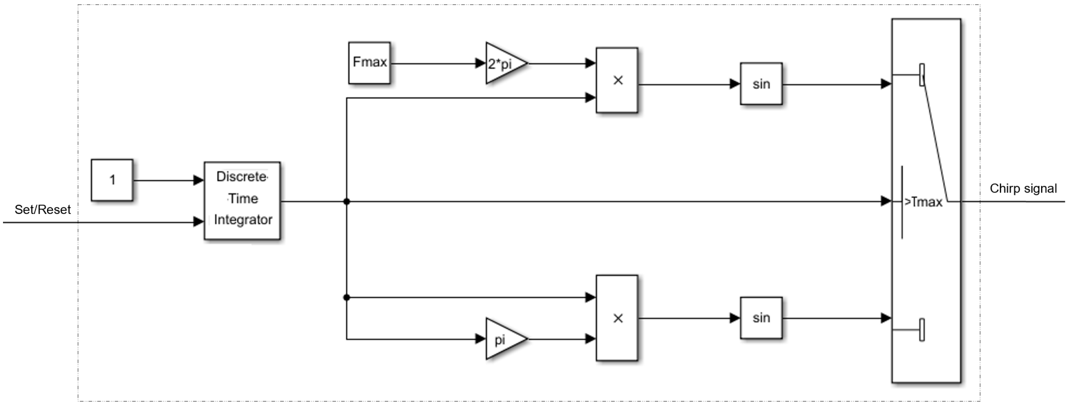

Figure 4.3: Block diagram for the generation of the discrete chirp signal. Note the presence of a switch block: when the maximum frequency is reached at the target time, this operator switches to a sinusoidal discrete signal with a constant frequency equal to Fmax.

where Δt_{chirp} t is the characteristic chirp time required to reach the maximum frequency $f_{chirp,max}$ starting from the initial one $f_{chirp,min}$.
The chirp signal is the solution adopted to explore the dynamic stage behaviour at different frequencies. It is worth to say that the classic impact test involved on these occasions turns out to be inefficient because the system under analysis is quite massive.
The function written before can't be deployed in a microprocessor, such as the *LaunchXL-F28379D*, which works in a finite way. The discretization of the equation 4.3 was performed using a counter module which simulates the time variable t by increasing the counter value by one unit for each work cycle. A *square operator* as well as a *sine-wave module* have been then combined as shown in figure 4.3 in order to replicate the function 4.3 in a finite way. Finally, the counter reset signal is driven by a *not* operator applied to the chirp input enable.

The script program generated for the case study allows to define the initial frequency $f_{chirp,min}$ and the maximum one reached $f_{chirp,max}$ as well as the characteristic chirp time Δt_{chirp}; moreover it is possible to chose in real time the value of the amplitude $V_{chirp,0}$ of the chirp signal. Generally, the Δt_{chirp} should be a compromise between a fast excitation that doesn't raise the coils temperature excessively and the possibility of revealing narrow resonances or anti-resonances; on the other hand, the amplitude $V_{chirp,0}$ should generate output signals in which the deviation induced by the noise is negligible without however leading the system to perform large displacements which could introduce non-linearity in the parameters. Experimental activities have revealed the values collected in the table 4.1 to be

$f_{chirp,max}[Hz]$	$f_{chirp,min}[Hz]$	$\Delta t_{chirp}[s]$	$V_0[V]$	$V_{chirp}[V]$
1	50	50	10.5	0.75

Table 4.1: Mechanical parameters.

suitable for the case analyzed.

A simplified version of the chirp voltage signal is the mono-frequency counterpart

$$V_{sin}(t) = V_{sin,0} sin(2\pi f_{sin} t) \tag{4.5}$$

being $V_{sin,0}$ and f_{sin} the amplitude and the characteristic frequency of the sinusoidal signal respectively.
This type of input has been introduced to understand how some system parameters would varied with frequency. In fact, the related output is a sinusoidal type signal too. Therefore, is relatively easier identify the wanted quantity via analytical formula.
As the previous case, the function 4.5 must be discretized too. This task has been fulfilled in a similar way to what is shown in figure 4.3, but whitout varying the frequency since it has been imposed in real time.

The voltage signal has been acquired directly from a **d**igital to **a**nalogue **c**onverter (**DAC**) pin of the launchpad and post-processed via *Scadas Mobile LMS acquisition system*.

4.1.1.3 Output signals

It should be recalled that the main goal of the whole project is the passenger comfort analysis of an electrodynamic levitation-based transport system depending also on the dynamic stability. In addition to the intrinsic behavior of the system, it should be remembered that it is possible to add active damping if one switches to active current control and the estimated relative velocity obtained from any observers is reliable. Therefore, it should be clear why the following output have been preferred among the signal acquires:

1. unsprung acceleration;
2. sprung acceleration;
3. current;

In particular, the accelerations have been sensed thanks to two *PCB Piezotronics* accelerometers screwed onto the upper aluminum plates of the sprung and unsprung masses respectively; the third signal has been detected by means of a current clamp

Measuring instrument	**Type**	**Gain sensitivity**	**max value**
Accelerometer	60305	12.95 mV/g	4g
Accelerometer	60307	12.64 mV/g	4g
Current clapm	PR30	100 mV/A	15A

Table 4.2: Measuring instruments and data acquisitions parameters.

PR 30 directly from the supply cable of the voice coil. All listed output are analogue voltage acquisitions whose sensitivity gain are collected in table 4.2.

Acquired signals have been managed by the combos *Scadas Mobile LMS acquisition system* and Simcenter TestLab Signature acquisition. The former is the hardware device that inherently converts, filter and process data from transducers into digital ones so these can be displayed analyzed, and stored in a computer (i.e. *Host PC*) n.3; the latter is the data acquisition software.
The setup of the measuring equipment has been a crucial point of the experimental tests, which led to spending time in order to get meaningful results. This process has involved mainly *Siemens* software in clearly define not only the sensitivity gains but also the acquisition ranges of sensed signals. In fact smaller upper limits could cause channel saturation while larger limits imply poor resolution. In table 4.2 chosen ranges can be consulted.

One of the most important measuring parameter which has been carefully discussed is the sampling frequency f_s. According to the Nyquist theorem, it should be at least twice the maximum signal frequency. Since the ultimate goal of the project is a human comfort analysis, the frequency range of interest spans from 0 up to $30Hz$ and, consequently, f_s should be set at least to $60Hz$. On the other hand, although a $30Hz$ oscillation can be detected, in practice the resolution is so low as to have poor output signals. This is why a safety factor on the sampling frequency should be expected.
For the case study, a value of $40KHz$ has been chosen. This may seem too high value which also risks dirtying acquired signals with high-frequency noises from the launchpad. Actually this happens and it has required filter action in post-processing activity. Nevertheless, a very large value was chosen for the resolution frequency because in the first tests, aimed at determining the electromagnetic damping of the voice coil only, the presence of dry friction generated acceleration signals with strong variations in a short time. In this case, small values of f_s have lead to poor output resolutions. In is worth to say that the effect of dry friction is not revealed in the levitating *2-DOFs* system because of the presence of a cushion of vibration due to the irregularities of the copper track. Anyway, the sampling frequency has

been set at $40KHz$ also in this case knowing that, thanks to the rapidity of tests, the amount of memory occupied by stored data would not have been worrisome.

In the end, once the acquired data have proved to be physically and mathematically acceptable, it has been possible to proceed with the identification of the integrated model representing the electrodynamical levitated electromechanical system.

4.1.2 Parameter estimation

The estimation of all those unknown parameters on which the numerical model is based is a crucial step for the fitting of the integrated equations with the experimental test bench. The word "estimation" is not a random choice: since the total number both of degrees of freedom and uncertain variables is large enough, it could be hard trying to match directly the experimental and numerical FRFs. A more convenient proceeding way has been that of carrying out a rough estimation of the unknown parameters in such a way as to have suitably starting trial values which have been subsequently tuned. It must be stressed that the reliability of the quantities found depends on how much the system does not deviate from linearity since the numerical models, chosen to describe the test bench, are based on this strong assumption. Furthermore, to simplify the estimation procedure, the disassembly and reassembly of the mechanical measuring device has been allowed in order to obtain more convenient configurations according to the parameter to be analysed. It is worth to say that in this context all experimental activities have been carried out without turning on the electric motor which drives the copper track, i.e. the electrodynamical levitated electromechanical system has been turned into a $3 - DOFs$ electromechanical system (2 mechanical and 1 electrical degrees of freedom) with the unsrpung mass resting on the ground. This is because the quantities relating to the electrodynamic suspension model carried out by *Pakštys* have been assumed to be correct [21].

That said, the unknown parameters for which a first attempt estimation has been provided are the following:

1. Voice coil constant;
2. Sprung and unsprung mass;
3. Sprung and unsprung stiffness;
4. Voice coil electromagnetic damping;
5. Voice coil resistance;
6. Voice coil inductance.

Domain	Parameter	Value
Electromechanical	K_M	$25 N/A$
Mechanical	m_{us}	$3.73 Kg$
	m_s	$16.45 Kg$
	k_{us}	$4216 N/m$
	k_s	$2200 N/m$
	c_{vc}	$207 Ns/m$
Electric	R_{vc}	1.43Ω
	L_{vc}	$11.1 mH$

Table 4.3: Characteristic model parameters from previous works.

The nominal as well as the estimated quantities given in previous thesis works ([18], [19], [20]) are collected in the table 4.3.

It must be stressed again the fact that the some estimation provided in the following subsections have to be understood as something that should make the fitting between FRFs curve easier and nothing more.

4.1.2.1 Voice coil constant

The nominal value of the *GeePlus* voice coil constant is provided by the manufacturer. This data has been considered reliable and for this reason the value as indicated in the table 4.3 has been used in the experimental identification procedure. Despite this, it has been regarded as interesting to evaluate the behaviour of such a variable.

From the available datasheet [28], the force exerted by the voice coil as a function of the displacement is provided, as reported in figure 4.4a where the previous parameter has been normalized with respect of its maximum value. In the same graph, it is shown a rough experimental evaluation of the force supplied for different mover offset. This trend has been obtained by evaluating the weight force exerted by the voice coil for a given voltage. Anyway, this estimation is so rough that it's not worth looking into further.

Beyond the absolute value, it is interesting to note how the mechanical voice coil constant varies in a non-linear way with the offset. On the other hand, there is a large range of displacements where the variation is negligible. Since the maximum value of the oscillations has been always lower than $30mm$ in the working condition analyzed, the K_m parameter has been assumed to be constant. The consequent error later have proved to be negligible.

It is also noteworthy the variation of the voice coil constant with the temperature.

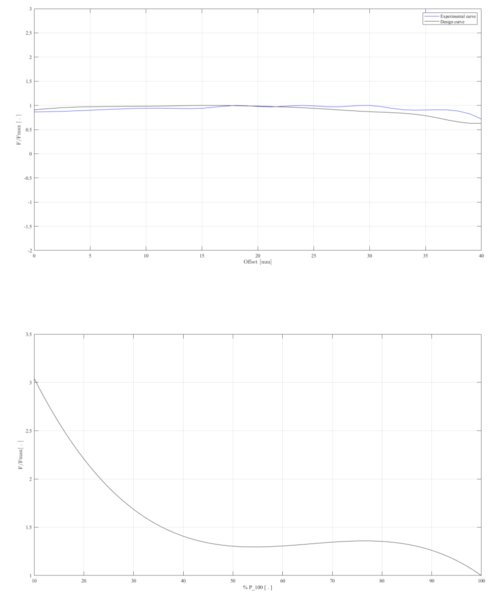

(a)

Figure 4.4: Voice coil constant. a) offset dependency. The blue line refers to the estimated parameter; the black line refers to the datasheet information. b) Temperature dependency.

The available datasheet provides information of the peak force at different percentage of the variable P_{100} defined as the continuous excitation power at which the coil attains the temperature of 120°C with the part mounted to a massive heatsink at 120°C. How it is possible to appreciate from figure 4.4, the temperature dependency is strong and cannot be neglected if the time duration of a test involving the voice coil is too long, especially in case of high currents.

4.1.2.2 Sprung and unsprung mass

The sprung and unsprung mass have been evaluated by simply weighing the various components of the dynamic device. In order to accomplish with this objective, the measuring stage has been dis-mounted, the mass of each single part has been assessed and finally summed to get the searched values. It is worth to say that even the weight of screw elements have been considered in the computation. Furthermore, as a first approximation, the masses of the springs have been distributed equally among the parts involved in the connection.

The nomenclature of each component of the dynamic measuring device is reported in figure 4.5 while the related mass values are collected in table 4.4.

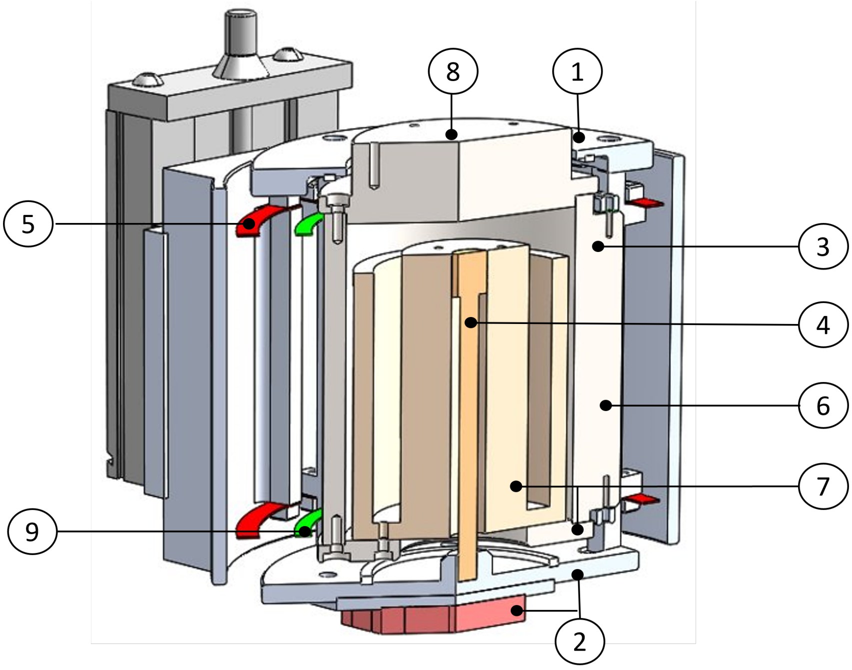

Figure 4.5: Description of the main parts of the dynamic measuring device. 1) Top alluminum plate; 2) bottom alluminum plate plus magnetic pad; 3) vertical alluminum beams; 4) voice coil mover; 5) unsprung spring; 6) ferromagnetic core; 7) voice coil magnetic case; 8) ferromagnetic cap. 9) sprung spring.

Unsprung mass		**Sprung mass**	
N°	**Mass [Kg]**	**N°**	**Mass [Kg]**
1	0.46	6	5.44
2	2.52	7	7.48
3 (x4)	0.512	8 2.84	
4	0.66	9(x8)	0.036
5 (x8)	0.09	-	-
	4.2		15.82

Table 4.4: Mass values. Screws mass is included in the total sprung and unsprung mass.

4.1.2.3 Sprung and unsprung stiffness

The sprung and unsprung stiffness have been evaluated by means of an impact test. This is a quite popular identification procedure for the estimation of mechanical systems frequency response functions since the Fourier Transform of an impulse tends to be constant so that each vibration mode can be equally excited.

The impact test has required the use of an instrumented hammer directly connected to *Scadas Mobile LMS acquisition system*. This is basically an hammer with a force transducer in its head that sense the generated impulse. This latter is then converted into an analogue voltage signal. From the point of view of the software, the introduction of the related sensitivity gain as well as a proper calibration of the instrumented hammer have been taken into account. Furthermore, the output has been given directly in terms of frequency response function so that stiffness values k_i have been computed considering the frequency $\bar{w}_{n,ki}$ associated to the resonance peak by resorting to the following formula

$$k_i = \bar{m}_{ki} \times \bar{w}_{n,ki}^2 \tag{4.6}$$

being $\bar{m}_{ki}$ a mass value that has yet to be defined.

In order to properly manage the equation 4.5, some considerations about the stiffness measuring and estimation procedure should be discussed, starting from the design and assembly features. In figure 4.6a), springs appear to be arranged circumferentially. As it has been described in *Chapter* 2, the unsprung elements (red ones) connect the stator and not suspended body while the sprung springs (green ones) are the only mechanical link between the two mass. From a structural point of view, these elastic elements can be assimilated to arc-shaped beams partially clamped at both ends. The word "partially" is not casual: the admissible relative vertical motion between the sprung and unsprung mass allows a relative macro-displacements between the extreme clamping constraints of each sprung springs; the same could be state for unsprung springs since a vertical relative macro-movement between the not suspended body and the stator is possible. Furthermore, it is worth to note the screw connection that keep in position each ends of the elastic elements in their housing allows a macro-rotation around the vertical direction as well as small compliance constraints in all other ones.

An other consideration regards the computation of the stiffness from the natural frequency obtained thanks to the impact test mentioned above. In fact, spring elements under analysis are continuous body and, so, they have theoretically a infinite number of natural frequencies depending also on the type of deformation considered. Even if this apparent obstacle can be overcome by stating that only the first flexural mode shape are considered, an more intricate problem still remains unsolved. This regards the mass value $\bar{m}_{ki}$ that should be considered in the computation of the sprung and unsprung stiffness starting from the knowledge of

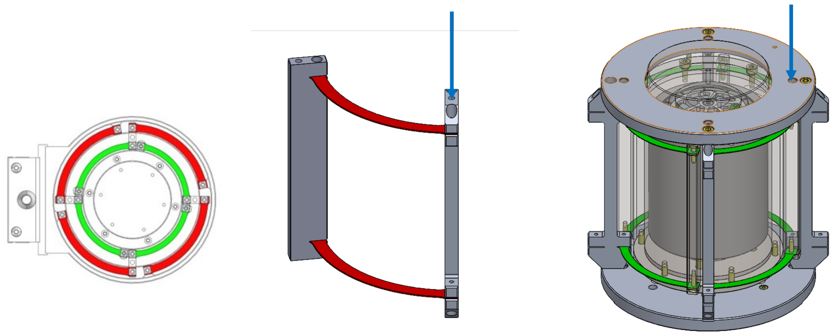

(a) **(b)** **(c)**

Figure 4.6: Subsystem configuration for the estimation of the springs stiffness. The blu lines show the point in which both the impulse has been applied and the accelerometer placed. a) Springs arrangement. b) Subsystem used for the estimation unsprung stiffness. c) Subsystem used for the estimation of the sprung stiffness.

the first natural frequency $\bar{w}_{n,ki}$. In fact, the 4.5 is a typical equation of a single degree of freedom system with lumped mass and stiffness. This expression can be extended to a multi-degrees of freedom system if it is possible to ensure great difference between inertial and elastic properties of its different parts. Actually, this is the case of the dynamic measuring device where the two bodies are more rigid and massive than the springs elements. In this sense, one could think to substitute the values of m_{us} and m_s for $\bar{m}_{ki}$ in order to get k_{us} and k_s respectively via equation 4.5. If this is theoretically correct, from an experimental point of view this is practically impossible since the elastic elements are so deformed because of the high bodies mass that they are not free of vibrating. On the other hand, considering springs alone cannot be the correct way forward. In this case it is difficult to replicate the specific constraints of the dynamic measuring device and, moreover, the mass is distributed in such a way that the 4.5 equation can lead to erroneous results.

In this context, the solution to the problem has been found by disassembling the system and reassembling it according to different configurations. In particular, for the estimation of the unsprung and sprung stiffness the systems shown in figure 4.6b and 4.6c have been used respectively. Starting from the dynamic measuring device, a precise subsystem has been derived which is made of the two aluminum plates and the four vertical beams of the not suspended body. The mass of such a substructure, that can be computed thanks to the values collected in table 4.4, allows to maximize the lumped mass attached to springs without an excessive pre-stress of the same.

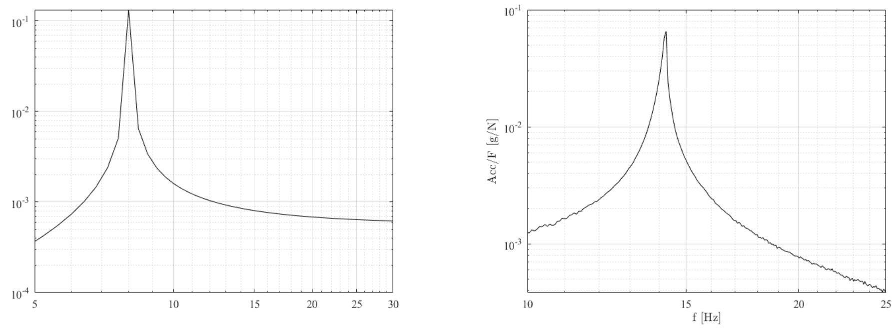

(a) **(b)**

Figure 4.7: Frequency response function of the spring elements. a) Sprung spring. b) Unsprung spring.

In a first case, this subsystem has been connected to the stator by means of only the unsprung elastic elements; in a second case, the same has been connected to the massive ferromagnetic core (which has thus played the role of ground) via sprung springs. In this way, two SDOF-type systems have been derived, the impact test have been applied to this configurations and the FRFs have been obtained, as shown in figure 4.7. It should be mentioned that the frequency response function related to the configuration of figure 4.7b has been computed numerically since free oscillations has been acquired in the time domain. This has no particular meaning but is linked to the fact that previous incorrect measurements have required the acquisitions to be carried out again, by which time the impact test bench had already been decomposed.

Starting from the FRFs, the natural frequencies $\bar{w}_{n,ki}$ have been detected and the stiffness values computed via equation 4.5. All results are summarized in table 4.5.

Simultaneously with experimental measurements, numerical simulations have been carried out to in order to have reference theoretical values. The software *Ansys* has been widely used to define FEM model. To be more precise, the springs have been modeled with four-node plate elements. At one of the end of the body

$Type$	$\bar{\omega}_{n,k}[rad/s]$	$\bar{m}_k[Kg]$	$k_{exp}[N/m]$	$k_{num}[N/m]$
Unsprung	89.6	1.1075	8891	8837
Sprung	50.33	1.74	4407	4450

Table 4.5: Estimated stiffness. Both experimental k_{exp} and numerical k_{num} are shown.

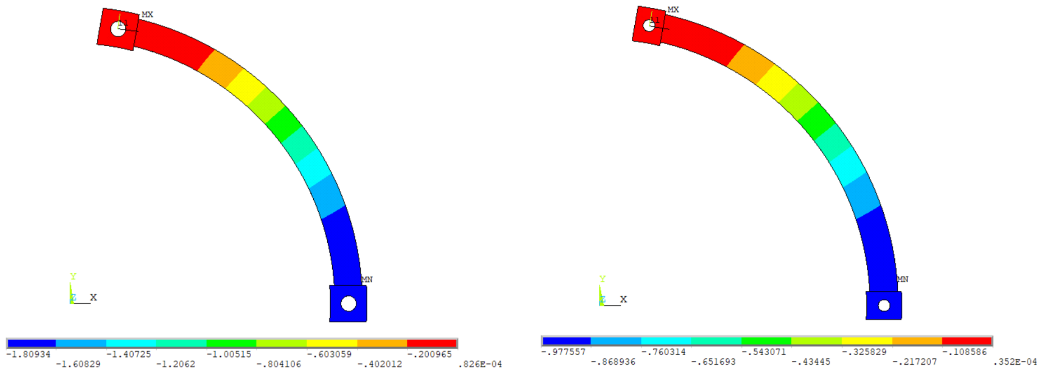

(a) **(b)**

Figure 4.8: Numerical structural simulation of spring elements. a) Sprung spring. b) Unsprung spring.

involved in the clamp all displacements except rotation about the vertical axis have been blocked; at the other one the same constraints have been applied but the vertical displacement of each node has been leaving free. It is worth to note that no constraints compliance have been introduced. So, the numerical stiffness should be expected to be greater than the experimental one.

Finally a vertical unit force has been applied at the proper end so that stiffness have been computed in both configuration as the inverse of the maximum vertical displacement. The related results are shown in figure 4.8 and collected in table 4.5. It is interesting to note that the experimental and numerical stiffnesses are quite similar. The latter are slightly larger than the former as expected.

The study of the unsprung and sprung springs is completed by the estimation of the structural damping. Since a frequency as well as a time response are both available, the half power and the logarithmic decrement method has been applied respectively [31]. The estimated parameters are collected in table 4.5.

4.1.2.4 Voice coil electromagnetic damping

The electromagnetic damping value of the voice coil is affected by some uncertainties due to neglecting the effects of temperature, offset and frequency and due to the linearization of the model. This is why the related estimation has been carried out by exciting the dynamic measuring device via sinusoidal signals in absence of levitation. Thus, a of single degree of freedom system in the mechanical domain has been obtained. In this context, the sprung body has played the role of the single lumped mass while the unsprung body has been considered as part of the ground.

For a given temperature and offset, the inertance and the phase of the response a SDOF mechanical system under mono-frequency input force can be easily computed as [31]

$$\ddot{X}_{sin} = -\bar{\omega}_{sin}^2 \frac{K_m \bar{I}_{vc,sin}}{\sqrt{(k_s - \omega_{sin}^2 m_s)^2 + (\omega_{sin} c_{vc})^2}} \tag{4.7a}$$

$$tan(\bar{\varphi}) = \frac{\bar{\omega}_{sin} c_{vc}}{k_s - \omega_{sin}^2 m_s} \tag{4.7b}$$

being $\ddot{X}_{sin}$ the amplitude of the acceleration sine signal at frequency $\bar{\omega}_{sin}$, $\bar{I}_{vc,sin}$ the amplitude of the sinusoidal measured current, k_s the sprung stiffness, m_s the sprung mass and $\bar{\varphi}$ the delay phase between acceleration and current.
By combining equation 4.7a and 4.7b, it is possible to obtain a relation of the damping coefficient as a function of only measured quantities

$$c_{vc} = \frac{K_m \bar{\omega}_{sin}}{\frac{\ddot{X}_{sin}}{\bar{I}_{vc,sin}}} \frac{tan(\bar{\varphi})}{\sqrt{1 + tan(\bar{\varphi})^2}} - 8 \times + c_{s,el} \tag{4.8}$$

where the second term is the structural damping of the sprung springs. This simple equation is able to estimate the parameter c_{vc} without considering any uncertainties deriving from the evaluation of stiffness and mass, except for the $c_{s,el}$ term. Furthermore, once the temperature and the offset have been fixed, this allows to explore the frequency dependency. On the other hand, it is necessary that the system under analysis has 1 degree of freedom only and that its general mechanical behavior is linear.

In order to properly manage equation 4.8, some considerations about the damping measuring and estimation procedure should be discussed, starting from the analysis of the voice coil acceleration shown in figure 4.9a, where the response to a sinusoidal voltage input at frequency of 10Hz is reported. It is worth to observe that this signal drops sharply immediately after reaching the maximum as well as the minimum amplitude, i.e. during the inversion of the motion. Consequently, a plateau of the correlated displacement signal should be expected following a double time-integration. This particular behaviour is due to the presence of dry friction between the mover and its housing, which can be also perceived aurally by moving the voice coil by hands. This intrinsic non-linearity affects the estimation of the damping since it is non predicted by equation 4.8.

Experimental activities have shown a reduction of this effect if the voice coil, rather than being taken alone, is mounted in the dynamic measuring device, so in a system with greater stiffness and mass. If then the electric motor is turned on and a relative velocity exist between the permanent magnet and the guideway, the acceleration drop due to dry friction can even disappear. This observation is not surprising if

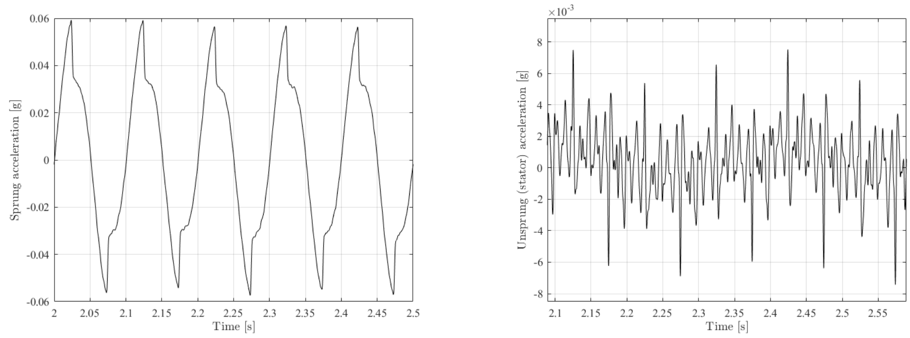

(a) **(b)**

Figure 4.9: Effect of the mover dry friction. a) Acceleration drop. b) Vibration of the stator.

one considers that the irregularities of the track create a cushion of not negligible vibrations above the fundamental excitation which prevent the mover from stopping during the inversion of the motion. However, the electrodynamical levitated system has not been considered for the damping estimation as the output acceleration signals are not sinusoidal due to the presence of such vibrations. Consequently, equation 4.8 is not valid and the frequency dependency of c_{vc} variable can not be easily detected.
The SDOF subsystem, in the sense described at the beginning of this section, has been preferred instead. Following the previous observations, one can think of introducing a numerical noise to avoid the abrupt stop due to dry friction. However, this strategy has not been followed as these background oscillations should be large enough to have effect on the massive suspended body, resulting in an output acceleration with lots of harmonics.
It is worth to note that another issue related to dry friction should be taken into account. As soon as the value of the static friction is reached during the motion reversal, the rapid variation of the acceleration of the suspended body results in a sort of impulsive force acting on the unsprung mass which, together with the stator, is excited and start to vibrate. The figure 4.9b show the acceleration of the unsprung mass under a sinusoidal excitation at frequency 10Hz. It comfirms what has been just said.

In this context, both assumptions required by the equation 4.8 are not satisfied. Nevertheless, an attempt has been made in order to estimate the damping coefficient, even if in a rough way. So, the SDOF system described at the beginning has been excited via sinusoidal signals at different frequencies and the impedance has been computed. Since the acceleration signals are not sinusoidal,the phase $\bar{\varphi}$ has been evaluated considering the time distance between the maximum input and output

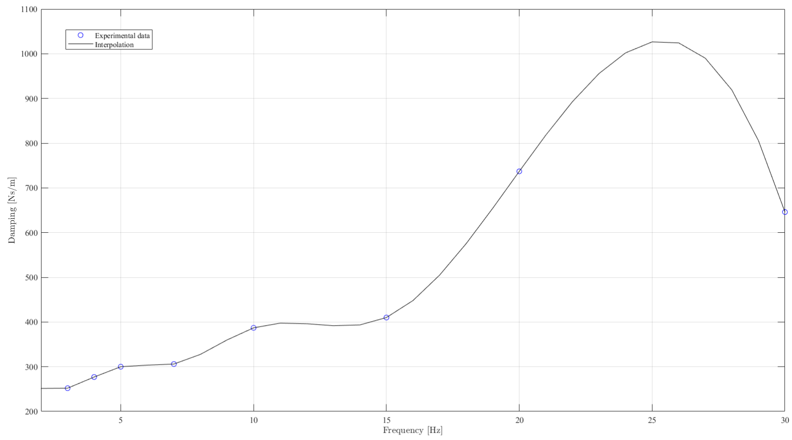

Figure 4.10: Estimated damping as a function of the frequency.

values

$$\bar{\varphi} = \bar{\omega}_{sin} \left[\bar{t}(\bar{I}_{0,max}) - \bar{t}(\ddot{\bar{X}}_{0,max}) \right] \tag{4.9}$$

This estimation has been improved by considering different time and amplitude values and extracting the square mean value.
The evaluated total damping c_s (electromagnetic + structural) as a function of the frequency is shown figure 4.10. This result refers to a load reliever equal to 10.5V, representing the working offset of the electrodynamical levitated electromechanical system. A mean value of Ns/m over the explored frequency range can be computed.

Finally, it must be stressed the fact that this estimation must be understood as qualitatively reference value. In fact, it should be remembered that the frequency variation could be affected by the vibration of the stator (which works as a dynamic damper), dry friction, temperature and other unknown effects which introduce further non-linearities.

4.1.2.5 Voice coil resistance

The voice coil resistance has been estimated by simply evaluating the ratio between the mean value of the applied voltage V_0 and that of the measured current $\bar{I}_0$, so that it results

$$R_{vc} = \frac{V_0}{\bar{I}_0} \tag{4.10}$$

To be more precise, the parameter so computed is the resistance of the entire supply circuit, from the launchpad up to the coil istelf.

Although the estimation of R_{vc} is very simple, actually also in this case there is a non-linearity. This due to the temperature which increases because of the Joule

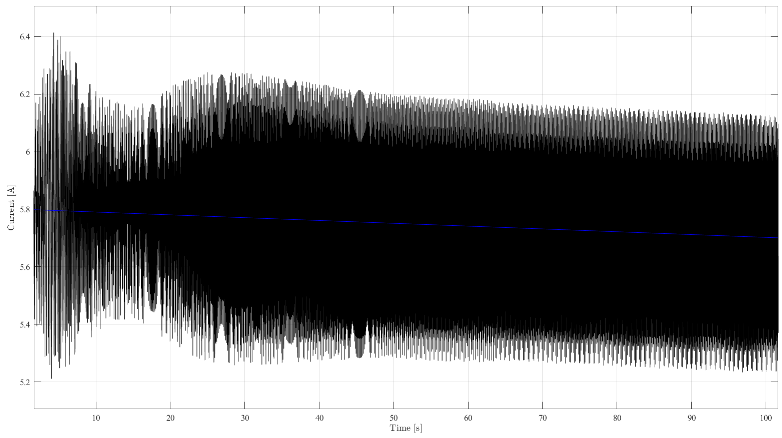

Figure 4.11: Decreasing trend of the current because of the increaing of temperature and resistance. The black line refers to the chirp signal; the blu line refers to the mean value of the current.

effect. As a results the resistance tends to increase too while the mean value of the current decreases, as shown in figure 4.11. This observation should not come as a surprise as it is already foreseen in the datasheet. Furthermore, one can note that he power involved is high since it is request to balance a great weight force linked to the sprung mass. Consequently, higher currents lead to higher energy losses and heating dissipation.
Since the average current changes continuously during the test for the same voltage, different resistance values can be computed. Experimental activities have proven to be convenient to choose a value of 1.77Ω. Anyway, it is should be remembered that the electric equation does not affect the final mechanical behavior of the electrodynamical levitated electromechanical system, so these uncertainties are not too worrying.

4.1.2.6 Voice coil inductance

The inductance value of the voice coil is affected by some uncertainties due to neglecting the effects of temperature, offset, frequency and the contribution of permanents magnet as well as other conductive parts above all. This is why the related estimation has been carried out by exciting the voice coil only. the power cables have been reversed so that the active force pushes down. In this way, if this mover motion is blocked, the BEMF voltage due to the relative velocity can be neglected. Thus, a single degree of freedom system in the electric domain has been obtained. Among the input, both step and sinusoidal signals have

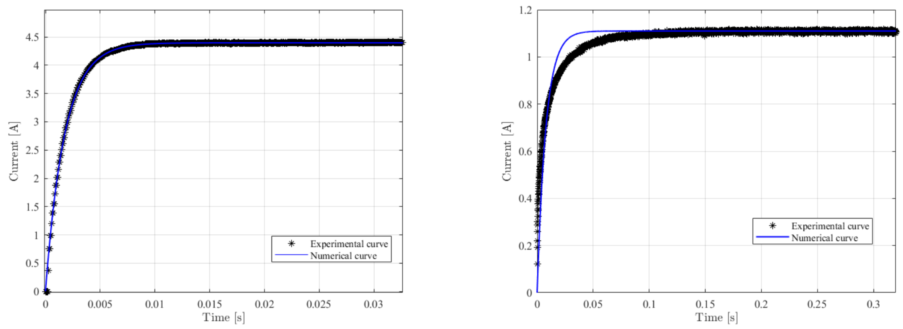

(a) **(b)**

Figure 4.12: Current transient under a step voltage input. a) Voice coil mover outside the magnetic case. b) Voice coil mover inside the magnetic case.

been preferred. These respectively allow to evaluate the static behaviour and the frequency dependency of the inductance.

For a given temperature and offset, the transient and dynamic responses under respectively step and mono-frequency input voltage response of an RL electric system can be easily computed as

$$\bar{i}_{vc}(t) = \frac{V_0}{R_{vc}}\left(1 - e^{-\frac{R_{vc}}{L_{vc,st}}(t-t_0)}\right) + \bar{i}_{vc,off} \tag{4.11a}$$

$$\bar{I}_{vc,sin} = \frac{V_{sin}}{\sqrt{R_{vc}^2 + (\bar{\omega}_{sin}\bar{L}_{vc,dyn})^2}} \tag{4.11b}$$

being V_{sin} the amplitude of the applied voltage at frequency ω_{sin}, $\bar{I}_{vc,sin}$ the amplitude of the sinusoidal measured current, $i_{vc,off}$ the offset current at initial time t_0 and voltage $V(t_0) = 0V$, $L_{vc,st}$ the static inductance and $L_{vc,dy}$ the dynamic counterpart. From a theoretical point of view, these are Expected to be equal. This is not the case for the voice coil under analysis

By resorting to a fitting procedure between numerical and experimental step RL transients, it is possible to estimate the static inductance; on the other hand, from equation 4.11a, it is possible to obtain a relation of the dynamic inductance coefficient as a function of only measured quantities

$$\bar{L}_{vc,dy} = \frac{1}{\omega_{sin}}\sqrt{\left(\frac{V_{sin}}{\bar{I}_{vc,sin}}\right)^2 - R_{vc}^2} \tag{4.12}$$

From a static point of view, a first estimation of the inductance has been made considering the mover out of its magnetic housing. A step voltage signal has

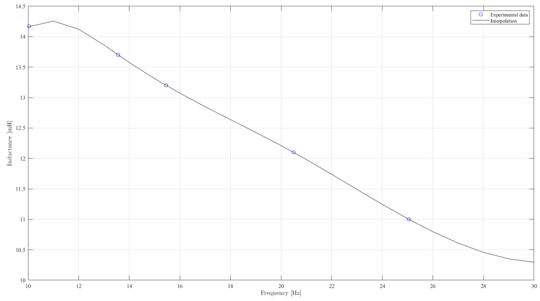

(a)

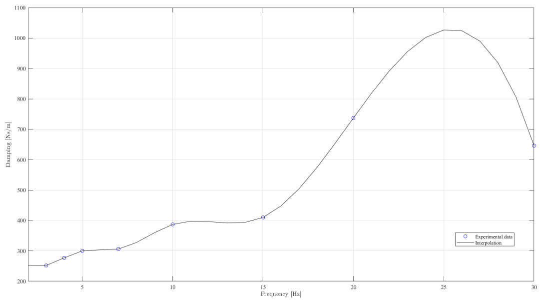

(b)

Figure 4.13: Estimated inductance. a) Offset dependency. b) Frequency dependency.

been applied and the current response has been detected. The fitting between experimental and numerical curves is shown in figure 4.12a. A good match has been obtained with the inductance value $L_{vc,st}$ reported in table 4.6.

In the figure on the right, it is possible to appreciate the pure transient electric response of the voice coil with the mover inside its magnetic case. In this case, a poor fitting between numerical and experimental curves has been revealed. This result is not surprising since the effect of magnets as well as that of the aluminum part have been neglected in equation 4.7a. In table 4.6 is collected the value of inductance $\bar{L}_{vc,st}$ that gives the less deviance between the curves shown in figure 4.12b with a null offset. Furthermore, the approximated $\bar{L}_{vc,st}$ has been studied at different mover position. The resulting function (figure 4.13a) is non-constant and presents a non-trivial dependency with the offset.

From a dynamic point of view, the equation 4.12 has been widely used to estimate the dynamic inductance $L_{vc,dy}$ at various frequencies of sinusoidal signals. Only the case in which the mover results in its magnetic envelope has been considered since the $L_{vc,st}$ does not vary with frequency. The results are shown in figure 4.13b,

Static		**Dynamic**	
In	**Out**	**In**	**Out**
L_{st}	L_{st}	L_{dy}	$\bar{L}_{vc}$
3	14.16	3	10.23

Table 4.6: Estimated inductance parameters. In and Out refers respectively to the condition in which the mover is inside and outside its magnetic case. All the values refer to mH engineering units.

while the related mean value $\bar{L}_{vc}$ is reported in table 4.6.
It must be stressed again the fact that this estimation must be understood as qualitatively reference value. In fact, it should be remembered that $L_{vc,dy}$ is not strictly speaking a pure coil inductance term since it inherently takes into account the voltage contribution induced by magnets and aluminum parts in a linear way. This is why, the mean value $\bar{L}_{vc}$ has been considered as more representative of the electric behaviour of the voice coil which can increase the efficiency of the linear model 3.34.

4.1.3 Experimental Frequency Response Functions

The dynamic behaviour of a system can be described by resorting to a Frequency Response Function which explores the ratio between output and input in the frequency domain. This physical instrument can be considered as the identity card of a system.

From a mathematical point of view, the *Fourier Transform* $\mathcal{F}[.]$ and the related properties have been widely exploited. In fact, the time-domain of the *convolution integral* $h(t)$ becomes the ratio between the *Fourier Transform* of the input $x(t)$ and output $y(t)$ in the frequency domain so that the FRF $H(\omega)$ can be written as [31]

$$H(\omega) = \mathcal{F}[h(t)] = \frac{\mathcal{F}[y(t)]}{\mathcal{F}[x(t)]} \tag{4.13}$$

The post-processed signals are clearly of digital type, so the *Fourier Transforms* appearing in the previous equation are the discrete ones. Thus, this continuous operator $\mathcal{F}[.]$ has been substituted by finite **F**ast **F**ourier **T**ransform (**FFT**) algorithm. Anyway, this function is already implemented in MatLab® with the name *fft(.)*.

Generally, in the computation of a system Frequency Response Function, it is common to use the estimator H_1 so that

$$H_1(\omega) = \frac{S_{xy}(\omega)}{S_{xx}(\omega)} \tag{4.14}$$

being $S_{xx}(\omega)$ the *auto-power spectral density* and $S_{xy}(\omega)$ the *cross-power spectral density.* These operators should be understood again in a discrete way and, so, are computed by means of the *Welch periodogram method* [31]
The function 4.14 increases the accuracy in estimating the FRF by working with the correlation of the input and output signals in order to reduce a poor estimation due to the presence of noise. It is worth to say that the estimator $H_1(\omega)$ coincides with the real Frequency Response Function $H(\omega)$ if the noise on the acquired signals is totally uncorrelated with the input noise. Furthermore, windowing and overlapping procedure can be implemented to prevent *leakage* effect. Anyway, also this function is provided in MatLab® with the name *tfestimate(.)*.

Finally, the time input and output signals acquired via *Scadas Mobile LMS acquisition system* have been post-processed in MatLab® to compute the Frequency Response Function of interest by resorting to both equations 4.13 and 4.14. The former has generally been preferred over the latter due to the lower computational cost.Moreover, in this contest, particular attention has been paid to the experimental definition of those constraints necessary to respect the hypotheses envisaged by the models discussed in *Chapter* 3.

Domain	**Parameter**	**Value**
Electromechanical	K_M	$25N/A$
Mechanical	m_{us}	$4.2Kg$
	m_s	$15.82Kg$
	k_{us}	$8891N/m$
	k_s	$4407N/m$
	c_{vc}	$400Ns/m$
Electric	R_{vc}	1.77Ω
	L_{vc}	$10.23mH$

Table 4.7: Summary of the characteristic model parameters obtained through the estimation procedure.

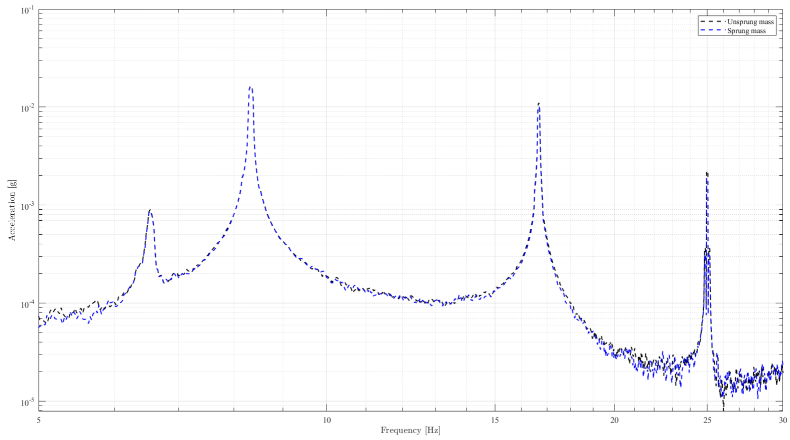

Figure 4.14: Experimental frequency transform of the sprung (blue) and unsprung (black) acceleration in a pure electrodynamic system. The velocity has been fixed at 500rpm.

4.1.3.1 Experimental electrodynamic suspension

The electrodynamic suspension has been replicated by turning on the electric motor which drives the guideway track and by imposing a null load reliever voltage. A levitated mass has thus been obtained. Actually, it has not been possible to eliminate the presence of unsprung springs. Therefore, the system under examination was rather a massive body connected to the ground by means of springs and excited by an electrodynamic lift force.

In order to identify the subsystem described above, the acceleration signals during the free vibrations of the block of the sprung-unsprung mass has been acquired. Since no input signals have been measured, it has been impossible to compute the Frequency Response Function in the sense introduced by equations 4.13 and 4.14.This is why, the Fast Fourier Transforms of the accelerations have been carried out for a rotor speed of 500rpm, as shown in figure 4.14.

It is interesting to note the presence of some peak values. These are consequences of the copper track irregularities which enter the system as a sum of sinusoidal excitations with frequencies multiple of the fundamental one (i.e. the angular velocity of the guideway). Furthermore, due to the mechanical behaviour, a resonance also appears around 6.5Hz.
Finally, it is worth to note that the FFT of the sprung and unsprung acceleration are superimposed. This is enough to confirm the validity of the test bench as it has been setup.

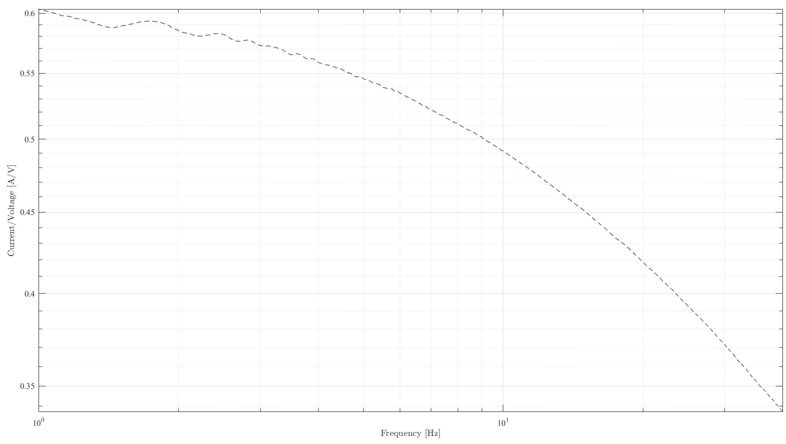

Figure 4.15: Experimental Frequency Response Function of the voice coil circuit as the ration between the output current and the input voltage.

4.1.3.2 Experimental voice coil circuit

The actuator circuit has been replicated by turning off the electric motor which drives the guideway track and reversing the supply coil cables. Consequently, the active force is directed downwards and the back-electromotive forces due to the relative speed can be neglected. In the case analyzed, the voice coil offset is about 2.5cm.

In order to identify the subsystem described above, the electric circuits has been excited by means of a chirp voltage signal with the characteristic parameters collected in table 4.1. The input voltage and the output current have been acquired and the Frequency Fourier Transform computed by resorting to the expression 4.13. The result of this identification is shown in figure 4.15.

It is interesting to note that the voice coil electrically behaves as a low-filter. This is not surprising since resistance and inductance properties characterize the coil circuit.

4.1.3.3 Experimental dynamic measuring device

In order to consider the dynamic measuring device alone the electrodynamic suspension has been removed by turning off the electric motor which drives the guideway track. However, because of the heavy mass of the dynamic stage, the unsprung mass is not able to balance the total weight force in the allowed deformation space. For this reason, the unsprung mass is in contact with the stator and only the suspended body can vibrate freely. The system thus defined behaves like a single

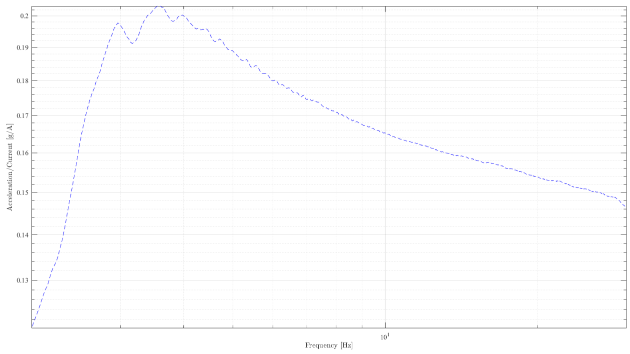

(a)

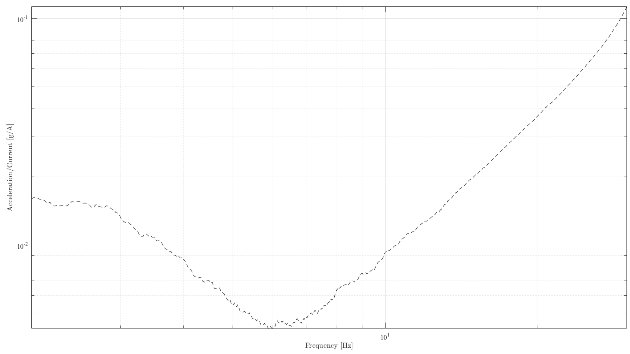

(b)

Figure 4.16: Experimental Frequency Response Function of the dynamic measuring device at 0rpm as the ration between the output acceleration and the input current. a) Sprung mass. b) Unsprung mass.

degree of freedom in a very approximate way. The word "approximate" is not casual since the vibration of the stator as well as the mover dry friction affect the behaviour of the system.

The identification of the dynamic measuring device in the condition described above has been carried out by applying a chirp voltage signal with the characteristic parameters collected in table 4.1. The input current and the output accelerations have been acquired and the Frequency Fourier Transform computed by resorting to the expression 4.13. The result of this identification is shown in figure 4.16.

It is interesting to note that the dynamic measuring device mechanically behaves as an high-pass filter toward accelerations and, so, a low-filter toward displacements. Furthermore, an unexpected antiresonance appear around 30Hz. This is a clear sign that something else is vibrating together with the system under consideration.

Probably, what has been considered as a stator actually is not.
Finally, it should be pointed out that the Frequency Response Function so obtained is not representative of the pure mechanical behaviour of the dynamic stage. This is because the harmonic contents at each frequency are affected those parts of the signal related to the dry friction and stator vibration effects that the Frequency Transform adds trying to replicate by means of a superimposition of trigonometric functions.

4.1.3.4 Experimental levitated electromechanical system

In order to study the Electrodynamical levitated electromechanical system the experimental test bench has been considered in its nominal design configuration. Thus, the guideway has been driven to a speed of 500rpm to simulate the electrodynamic suspension and the load reliever signal has been applied to balance the weight force and introduce electromagnetic viscous damping.
On the other hand, some practical expedients have been adopted to try to respect all the linearity hypotheses of the related numerical model. The measuring strategy adopted can be summarized as follows:

1. The dynamic stage is raised to its maximum possible height thanks to the micrometric screw;
2. The *Kollmorgen AKM74L* motor is driven up to the target speed by the *Kollmorgen AKD inverter*. Since the air gap has been maximize in the previous step, the energy losses and the increasing of temperature of the track due to the drag force can be limited;
3. The dynamic stage is lowered until the lift force is such as to impose the first non-negligible oscillations on the system;
4. The load reliever voltage signal is applied. Leaving this operation to the last but one step, the heating due to the Joule effect is minimized;
5. The dynamic stage is lowered until the unsprung spring reaches their undeformed configuration.

Although this is a very laborious process, experimental activities have confirmed the effectiveness of this strategy.

The identification of the Electrodynamical levitated electromechanical in the condition described above has been carried out by applying a chirp voltage signal with the characteristic parameters collected in table 4.1. The input current and the output accelerations have been acquired and the Frequency Fourier Transform both for the sprung and unsprung mass have been computed by resorting to the expression 4.14. The result of this identification is shown in figure 4.17.

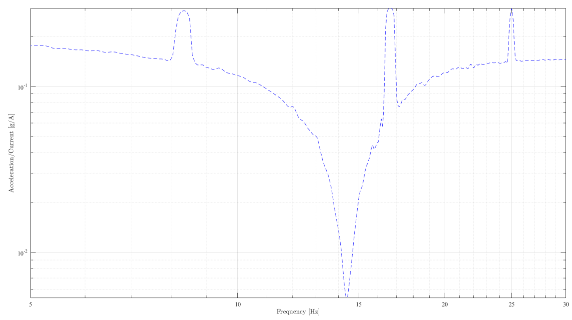

(a)

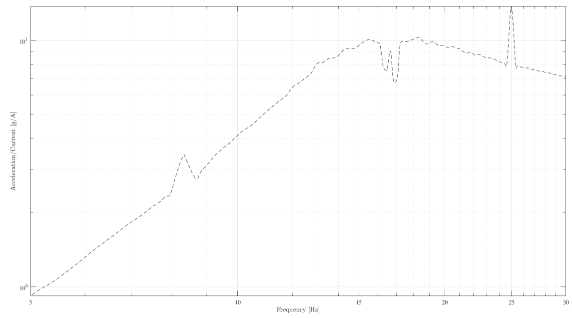

(b)

Figure 4.17: Experimental Frequency Response Function of the experimental test bench at 500rpm as the ration between the output acceleration and the input current. a) Sprung mass. b) Unsprung mass.

It is interesting to note the presence of peaks as well as an antiresonance around 14Hz in the sprung response. The former are a consequence of the copper track irregularities; the latter depends on the active force exerted by the voice coil. In fact, when a current different from zero is applied, the actuator generates a pair of forces directed in opposite directions on the two bodies. Thus, the FRF computed in figure 4.17a refers to a point to point inertance. It is well know from theory [31] that if the response (acceleration of the sprung mass) is measured at the same point where input (one of the strength of the voice coil) is applied, an antiresonance always appears between two successive resonances of the response. This also applies to the FRF of the unsprung mass, but evidently the presence of damping does not make the antiresonance visible.
Finally, it is worth to underline that no resonance peaks can be detected from figure 4.17a. This is because the damping ratio is obviously high.

4.2 Numerical simulations

In parallel with the experimental experiences, theoretical models described in *Chapter* 3 have been tested. First of all, an accurate revision of the physics involved has been performed so to delete computational issues, mathematical obstacles and absurd behaviors of the equations in the physical sense. Then, it has been wondered about the most convenient and reliable way to obtain numerical solutions. This is why multi-body analysis, matrix calculations and parametric studies have been carried out and compared in terms of efficiency, effort and quality of the results. In this context, MatLab® and Simulink® environment have been widely exploited.

Among all the computational instruments investigated, matrix calculations and dynamic time simulations both based on the state space representation have been preferred. This is due to the simplicity of implementation and the excellence of the solutions achieved. In the following section, the main numerical simulations of interest are described. The values of the parameters appearing in the equations are those previously estimated through experimental tests. These values are summarized in table 4.7.

4.2.1 Copper track irregularities

In *Chapter* 2 it has been mentioned the presence of geometric irregularities in the copper track. From the experimental point of view, these have been proved to excite the system which a characteristic frequency which is multiple of the peripheral speed of the guideway itself. Since their presence characterizes in some way the test bench under consideration and since the oscillations of the dynamic suspension with suspended mass are caused by these irregularities, it has been considered appropriate to introduce a strategy to simulate them numerically.

The general followed idea has been that of exploiting the periodicity of irregularity to recreate excitation as the sum of trigonometric functions of appropriate phase and amplitude (i.e. using the Fourier series). In fact, since the motion of the track is simulated by the test bench through the rotary movement of a copper circulating ring, every point of the guideway itself transits under the magnetic pad every intervals of time proportional to the inverse of the peripheral speed. Therefore, this is a matter of reproducing the spatial trend of the irregularities and make it move in time with a very precise speed, similar to what happens for the propagation of waves. This goal can be achieved either by considering the trend of irregularities as shown in the figure 2.8, or by reproducing it as a summatory of angular harmonics. The latter way has been followed since it is a more elegant modelling strategy and allows among other things to restrict the analysis only to the range of frequencies of interest.

The transform (or series) of Fourier applied to the distribution of the irregularities is shown in figure 4.18. Note that the harmonic content $\Delta Z_{irr,0}$, expressed in units of length, is zero at the origin (mean zero of the signal) and that the *x axes* reports the angular wavelengths $_{theta}$ and not the frequencies. It can be observed that these last ones are multiples integers of $1/2\pi$, so the signal of the irregularities $\Delta z_{irr}(\theta)$ can also be written as

$$\Delta z_{irr}(\theta) = \sum_{k=1}^{N} \Delta Z_{irr,k} sin\left(\lambda_{\theta,k}\theta + \phi_k\right) \tag{4.15}$$

being ϕ_k the angular phase of the k_{th} harmonic, N the total number of harmonics that make up the periodic signal and θ the angular coordinate that goes from 0 up to 2π radians.
From figures 4.14 and 4.17 it is evident that only the contribution of the first 5 harmonics. For this reason, the following approximation can be accepted for the case study

$$\Delta z_{irr}(\theta) \approx \sum_{k=1}^{5} \Delta z_{irr,k} sin\left(\lambda_{\theta,k}\theta + \phi_k\right) \tag{4.16}$$

The propagation of these angular waves in time and space can be achieved by first associating a k frequency $f_{irr,k}$ to each k angular wavelengths $\lambda_{\theta,k}$. By taking into account the appropriate engineering units, this is equal to

$$f_{irr,k} = 6 \times \omega_{rpm} \times \lambda_{\theta,k} \tag{4.17}$$

where ω_{rpm} is the angular speed of the copper ring. It is worth to observe that $f_{irr,k}$ changes with the rotor speed while $\lambda_{\theta,k}$ is constant as expected.
Through the equation 4.17, the angular distribution of irregularities Δz_{irr} can be turned into a time signal $z_{irr}(t)$ of the type

$$z_{irr}(t) \approx \sum_{k=1}^{5} \frac{\Delta z_{irr,k}}{1000} sin\left(2\pi f_{irr,k} + \phi_k\right) \tag{4.18}$$

where the number "1000" takes into account the fact that the angular harmonic content is expressed in millimeters while the models work with the international measurement system.
Finally it should be remembered that track irregularities enter the system in terms of speed (§3.1.3). Therefore, the real input signal to be inserted in the models is as follows

$$\dot{z}_{irr}(t) \approx \sum_{k=1}^{5} 2\pi f_{irr} \frac{\Delta z_{irr,k}}{1000} sin\left(2\pi f_{irr,k} + \phi_k\right) \tag{4.19}$$

This sum of sinusoidals has been implemented directly in the Simulink® environment and has proven effective to approximate the effect induced by irregularities, as will be highlighted in the following.

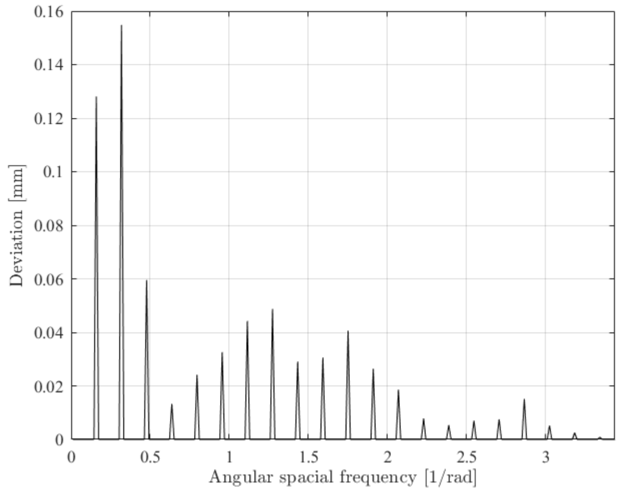

Figure 4.18: Fourier Transform applied to the copper track irregularities.

4.2.2 Numerical Frequency Response Functions

As with real physical systems, the dynamics of a set of theoretical linear equations numerical is also well captured by its Frequency Response Functions. For this reason, these latter have been carried out by means of simulations in order to have global descriptions of the behaviour of the numerical models.

The state space equations directly implemented in Simulink® environment give as solutions something that can be understood as time signals. In this sense, once imported into the MatLab® environment, the Fast Fourier Transform has been proven to be sufficient for the estimation of the related Frequency Response Function according to the relation 4.13. In fact, the estimator H_1 is a too refined mathematical tool for theoretical signals noise-free signals.

The state space equations directly implemented in MatLab® environment allow the estimation of the FRF via matrix calculation. In this context, it is necessary to carry out the system *Transfer Function matrix* $[H(s)]$ written in the *Laplace* domain, whose general expression is [29]

$$[H(s)] = \frac{Y(s)}{U(s)} = [C](s[I] - [A])^{-1}[B] + D \tag{4.20}$$

being $[I]$ the identify matrix, $Y(s)$ the Laplace transform of the output vector, $U(s)$ the Laplace transform of the input vector ans $s = i\omega$ the Laplace variable. Finally, the Frequency Response Function of the i_{th} output with respect of the j_{th} input can be obtained from the (i, j) element of the *Transfer Function matrix*

$$H(s)_{ij} = \{C\}_i(s[I] - [A])^{-1}\{B\}_j + d_{ij} \tag{4.21}$$

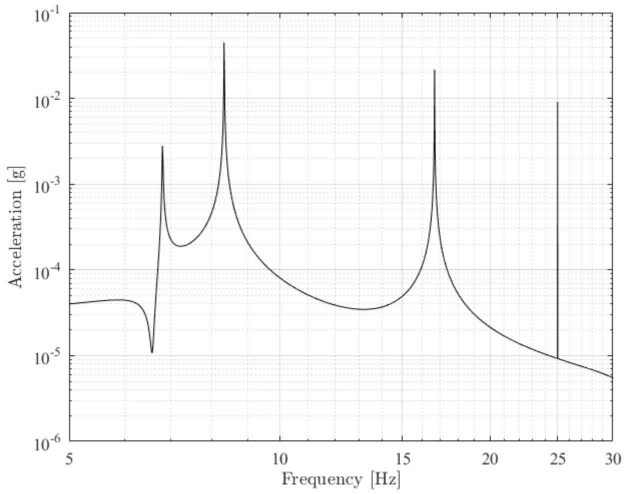

Figure 4.19: Numerical frequency transform of the sprung (blue) and unsprung (black) acceleration in a pure electrodynamic system. The velocity has been fixed at 500rpm..

where $\{B\}_j$ is the j_{th} column vector of the input gain matrix, $\{C\}_i$ is the i_{th} row vector of the output gain matrix and d_{IJ} is the element (i, j) of the direct link matrix. Anyway, this function is already implemented in MatLab® with the name *bode(.)*.

4.2.2.1 Numerical electrodynamic suspension

The numerical electrodynamic suspension dynamics behaviour has been simulated in Simulink® environment. A *State Space* block capable of simulating the dynamics induced by the state space matrices over time has been introduced for this purpose. Then, the inputs relating to the weight force and the irregularities of the copper track has been considered and the acceleration of the sprung mass has been evaluated. To be more precise, a spin speed of 500rpm has been considered and both the damping and stiffness contribution of the unsprung spring have been introduced in state space matrices (Appendix A) in order to deal with a model similar to real case.

A Frequency Response Function of physical interest can not be obtained from such a simulation since no relevant active input signal is present. As for the experimental counterpart, the Fast Fourier Transform of the acceleration signal has been computed according to the equation 4.13.
The result is shown in figure 4.19. It is interesting to note the presence of peaks due to copper track irregularities around frequencies which are multiple of the peripheral

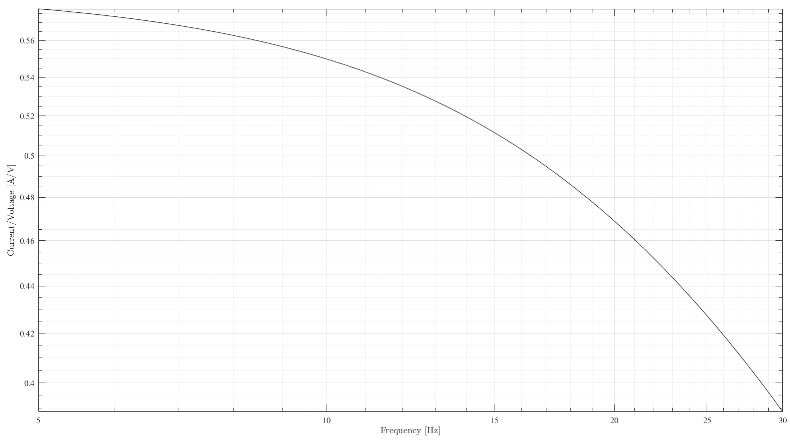

Figure 4.20: Numerical Frequency Response Function of the voice coil circuit as the ration between the output current and the input voltage.

velocity of the guideway itself as well as a resonance due to the mechanical system.

4.2.2.2 Numerical voice coil circuit

The voice coil circuit dynamics behaviour has been simulated in MatLab® environment. The state space matrices related to the actuator model has been modified by neglecting the BEMF term. A pure electric equation has been thus obtained.

The Frequency Response Function of interest should allow the current output to be estimated for a given applied voltage. In this contest, the following Transfer Function has been considered

$$H(s)_{vc} = [C]_{vc,E}(s[I] - [A]_{vc,E})^{-1}[B]_{vc,E} + D_{vc,E} \tag{4.22}$$

being $[A]_{vc,E}$ the dynamic matrix, $[B]_{vc,E}]$ the input gain matrix, $[C]_{vc,E}]$the output gain matrix and $[D]_{vc,E}$ the direct link matrix as summarized in appendix A. Note that these state operators define a ***S**ingle* ***I**nput* - ***S**ingle* ***O**uput* system (**MIMO**), so that the the computation of the transfer function is not particularly complex. The result is shown in figure 4.19. The numerical simulation proves that the voice coil electrically behaves has a low-pass filter.

4.2.2.3 Numerical dynamic measuring device

The dynamic measuring device frequency behaviour has been simulated in MatLab® environment. The state space matrices described in *Chapter* 3 (§3.2.4) have been modified by adding a stiffness term. In this way, a more suitable model has been

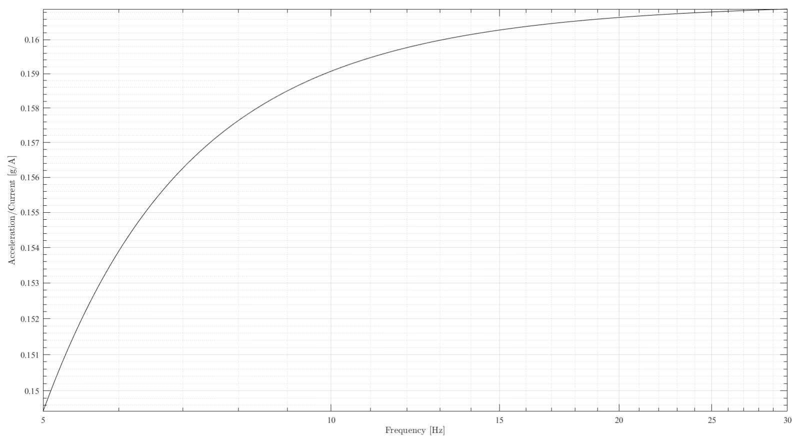

Figure 4.21: Numerical Frequency Response Function of the dynamic measuring device at 0rpm as the ration between the output acceleration and the input current.

obtained to describe what has seen experimentally in the previous section (§4.1.3.3).

In this contest, the following Transfer Function matrix has been considered

$$[H(s)]_{EM} = [C]_{vc,K}(s[I] - [A]_{vc,K})^{-1}[B]_{vc,K} + D_{vc,K} \tag{4.23}$$

being $[A]_{vc,K}$ the dynamic matrix, $[B]_{vc,K}]$ the input gain matrix, $[C]_{vc,K}]$the output gain matrix and $[D]_{vc,K}$ the direct link matrix as summarized in appendix A. Note that these state operators define a ***M****ultiple* ***I****nput* - ***M****ultiple* ***O****uput* system (**MIMO**). In particular, $[H(s)]_{EM}$ is a 2 by 2 matrix where the input can be identified in the force and the voltage while the output correspond in order to the acceleration and the current. Thus, considering the balance of an external constant force, two transfer functions that link the acceleration and the current to the voltage can be derived

$$H(s)_{EM,1,2} = \{C_{vc,K}\}_1(s[I] - [A]_{vc,K})^{-1}\{B_{vc,K}\}_2 + d_{vc,K1,2} \tag{4.24a}$$
$$H(s)_{EM,2,2} = \{C_{vc,K}\}_2(s[I] - [A]_{vc,K})^{-1}\{B_{vc,K}\}_2 + d_{vc,K2,2} \tag{4.24b}$$

where, according to what shown in appendix, the row subscript "1" refers to the output acceleration, the row subscript "2" refers to the output current and column subscript "2" refers to the input voltage.

Finally the Frequency Response Function of interest can be obtained from the following transfer function

$$H(s)_{EM} = \frac{H(s)_{EM,1,2}}{H(s)_{EM2,2}} \tag{4.25}$$

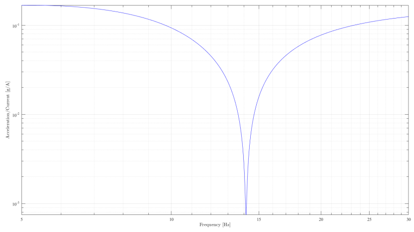

(a)

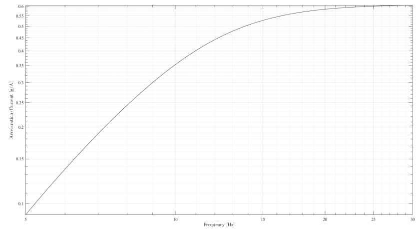

(b)

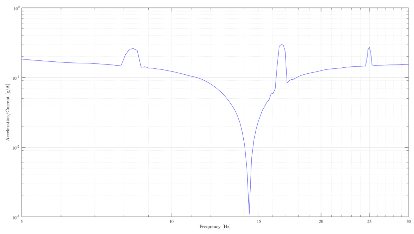

(c)

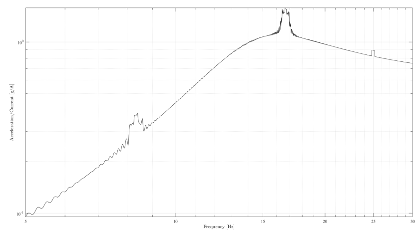

(d)

Figure 4.22: Numerical Frequency Response Function of the experimental test bench at 500rpm as the ration between the output acceleration and the input current. a) Sprung mass. b) Sprung mass without track irregularities effects. a) Unsprung mass without track irregularities effects. c) Sprung mass with track irregularities effects. d) Unsprung mass with track irregularities effects

The result is shown in figure 4.21. The numerical simulation proves that the dynamic device, approximated as a single degree of freedom system, behaves has an high-pass filter toward accelerations.

4.2.2.4 Numerical levitated electromechanical system

The behaviour in the frequency domain of the electrodynamical levitated electromechanical system has been simulated both in MatLab® and Simulink® environment. In the first case, the computation of Frequency Response Function is faster once the Transfer Function matrix has been identified. On the other hand, it not possible to take into account the effect of irregularities. This is why a time-simulation has been carried out via Simulink®. Here, a *State Space* block capable of simulating the dynamics induced by the state space matrices over time has been introduced as well as all the input and output wanted by the model. The results has been, then, imported in MatLab® environment and, finally, the FRF has been computed by resorting to equation 4.13.

It could be noteworthy to describe the derivation of the transfer function matrix. Note that in this case, this operator is a 3x4. The three output correspond in order to unsprung acceleration, sprung acceleration and voice coil current; the four input are related in order to unsprung force, sprung force, voltage and track irregularities. Thus, by neglecting for a while the excitation due to external forces and copper track irregularities, three transfer functions that link the accelerations and the current to the voltage can be derived

$$H(s)_{1,4} = \{C\}_1(s[I] - [A])^{-1}\{B\}_4 + d_{1,4} \tag{4.26a}$$
$$H(s)_{2,4} = \{C\}_2(s[I] - [A])^{-1}\{B\}_4 + d_{2,4} \tag{4.26b}$$
$$H(s)_{3,4} = \{C\}_3(s[I] - [A])^{-1}\{B\}_4 + d_{3,4} \tag{4.26c}$$

where, according to what shown in appendix, the row subscript "1" refers to the output unsprung acceleration, the row subscript "2" refers to the output sprung acceleration, the row subscript "3" refers to the output current and column subscript "4" refers to the input voltage.
Finally the Frequency Response Function of interest can be obtained from the following transfer function

$$H(s)_{us} = \frac{H(s)_{1,4}}{H(s)_{3,4}} \tag{4.27a}$$
$$H(s)_{s} = \frac{H(s)_{2,4}}{H(s)_{3,4}} \tag{4.27b}$$

Some results are shown in figure 4.22. It should be emphasised that numerical simulations carried out in the MatLab® environment don't allow to capture the effect of the track irregularities as expected. On the other hand, regardless of the computational strategy used, the theoretical model demonstrates the presence of the antiresonance.

4.3 Systems identification

So far, experimental measurements and numerical simulations have been carried out in parallel but always separately way. Some characteristics are well understood from both sides, such as the effect of the irregularities, the presence of an antiresonance and the behavior as a low-pass and high-pass filter respectively in the electrical and mechanical domains. Despite this, if the results do not coincide, the numerical models remain the object of a purely theoretical speculation while the test bench does not have its own engineering characterization. For this reason, this third and final section of the chapter attempts to match numerical simulations with experimental measurements in terms of Frequency Response Functions. Errors in parameter and model estimates are highlighted and appropriate corrections are then suggested.

Due to the complexity of the system under analysis and the great uncertainty in most of the model parameters, the fitting between experimental and numerical curves has been carried out iteratively. Different combination of parameters values has been tried starting from the estimated ones and finally the final match has been obtained thanks to the the experience acquired in managing the equations under analysis and improved through practice during laboratory activities.

It is worth saying from the outset that the fit has not been satisfied for all systems, especially those where limitations in the linearization assumptions and complex unintended physical effects are strongly manifested.

4.3.1 Electrodynamic suspension curve fitting

In figure 4.23a the sprung acceleration in the frequency domain of the experimental electrodynamic suspension is compared with the numerical one obtained using the parameters estimated in the first section of this *Chapter*. It is worth to observe that, meanwhile the effects of the copper track irregularities are well captured by the numerical model, the experimental resonance is characterized by an higher frequency. This is due to an error in the unsprung stiffness value which is lower than it should be. Probably the configuration exploited in the impact test have led to a less rigid constraints configuration.

In order to match the two curves, the stiffness has been increased to obtain a resonance frequency equal to the experimental one. In particular, a value of 9700 N/m leads to a suitable curve fitting, as shown in figure 4.23b. It it worth to note that also the unsprung damping has been varied so to improve the fitting. A value of 3Ns/m has been used. Despite this, it should be noted that the fitting between the curves is not very accurate. On the other hand, it should also be remembered that this is not an FRF but a Frequency Transform of a signal over time. So, the uncertainties in this case have more weight and, furthermore, even numerical value in the computation of the Fourier Transform can appear in the plot. It is sufficient to think that the experimental resonance peak value is too small for a damping which is not so high and that leakage effect can introduce other error. Nothe that, since an input is not present, the estimator H_1 in equation 4.14 can't be used together with the usefull overlapping and windowing procedures.
Anyway, no further effort has been spent to improve the fitting of the electrodynamic suspension acceleration signal since the main goal of the thesis is focused in the integrated model. Moreover, it is more interesting to try to math FRFs curves that in this case are non present.

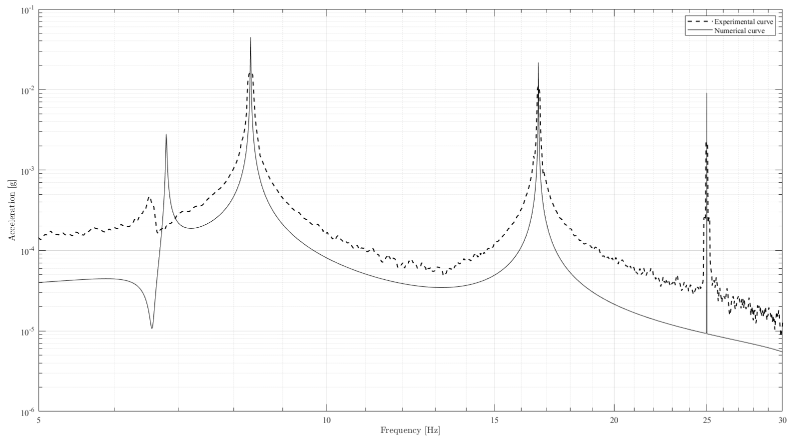

(a)

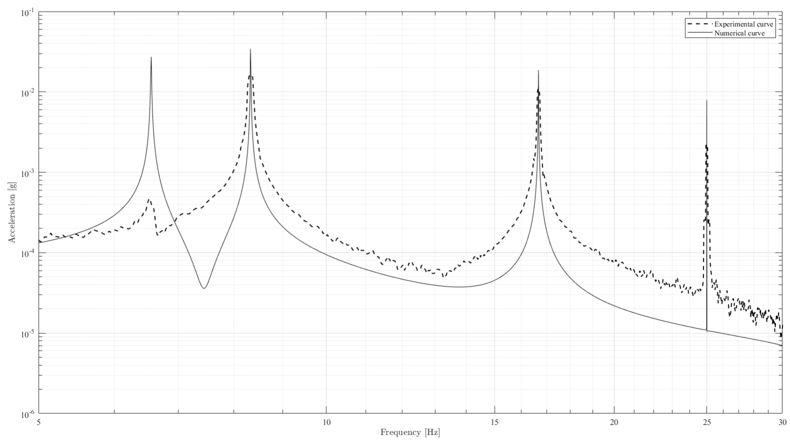

(b)

Figure 4.23: Electroynamic suspension curve fitting. a) Numerical FRF computed with estimated parameters. b) Numerical FRF computed with tuned parameters.

4.3.2 Voice coil circuit curve fitting

In figure 4.24 the Frequency Response Function of the voice coil electric circuit is compared with the numerical one obtained using the parameters estimated in the first section of this *Chapter*. As it is possible to see, the curves don't match at all. This is due not only to an error on the estimation of the inductance but also to a basic wrong numerical modelling approach. In fact, this figure confirms what has been repeated since the beginning: the voice coil does not behave electrically as an

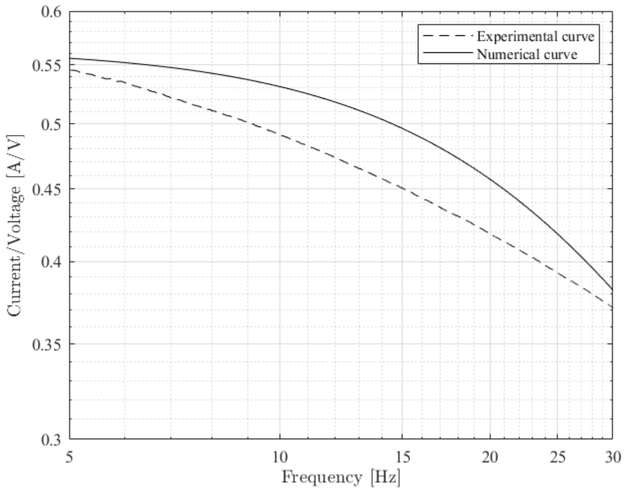

(a)

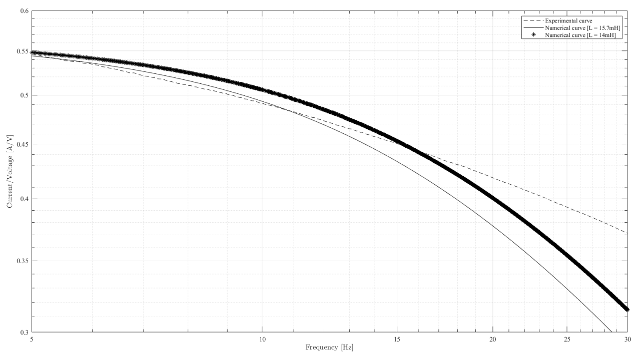

(b)

Figure 4.24: Voice coil curve fitting. a) Numerical FRF computed with estimated parameters. b) Numerical FRF computed with tuned parameters.

RL circuit. In particular, it is evident that the theoretical equation overestimates the Frequency Response Function. On the other hand, it should be remembered that an accurate representation of the electric actuator does not fall within the final objectives of the thesis.

In order to minimize the deviation between the two curves, an inductance value of 14mH (from table 4.6) has been carried out (dashed line). Since the trend of experimental curve are very different, it has been also found a value of 15.7mH that matches of the model at low frequency with acceptable approximation (dots lines).

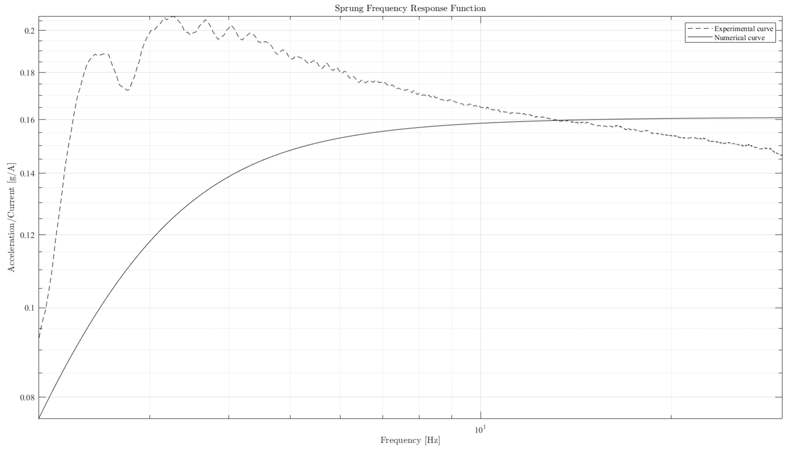

(a)

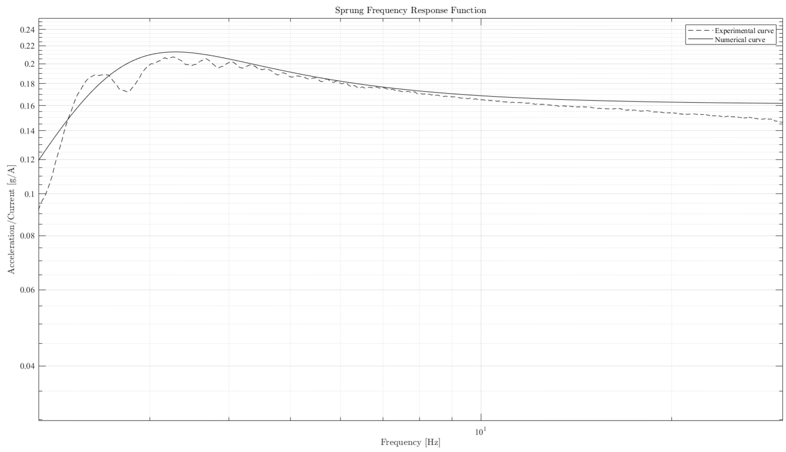

(b)

Figure 4.25: Dynamic measuring device at 0rpm curve fitting. a) Numerical FRF computed with estimated parameters. b) Numerical FRF computed with tuned parameters.

4.3.3 Dynamic measuring device curve fitting

In figure 4.25 the Frequency Response Function of the dynamic measuring device which behaves as an SDOF system is compared with the numerical counterpart obtained using the parameters estimated in the first section of this *Chapter*. It is interesting to note that the resonance frequencies do not coincide. As pointed out in the previous fitting procedure, also in this case the (sprung) stiffness is underestimate. Furthermore the general trend of the curves is quite different. This is because of a bad damping estimation instead.

In order to match the Frequency Response Functions, the equivalent undamped numerical system has been investigated, the stiffness has been increased in this context to obtain equal resonance frequencies and the damping has then been tuned to get the experimental trend. In particular, values of $K_s = 4422N/m$ and $c_s = 220Ns/m$ lead to a suitable curve fitting, as shown in figure 4.25b.
It should be pointed out that the frequency responses drift starting from a frequency around 10Hz up to the appearing of an experimental antiresonance which is not captured by the numerical model. This is probably due to the vibration of the stator as confirmed by its FRF shown in figure 4.26a. It is worth to note that vibrations of what has been wrongly considered as a ground increase with frequency and reach values of the order of the sprung acceleration starting from 10Hz.

If an absolute match between curves is required, one possible solution can be that of adding the presence of other degrees of freedom in the theoretical equations that simulates the stator. This idea has been tested by resorting to the state space representation of the complete dynamic measuring device (Appendix). Obviously, the state matrices are the same from a mathematical point of view but different from the conceptual one. In fact, in order to study the case under analysis (related to the oscillations of a SDOF system with compliance ground), it is necessary to replace the parameters of the sprung and unsprung mass with those of the sprung and ground respectively. In particular, the stiffness of the ground has been chosen in order to match the antiresonance frequency.
The result carried out thanks to the last correction is shown in figure 4.26b. It is noteworthy that the numerical Frequency Response Function so obtained not only reveals the presence of the antiresonance but also seems to better follow the experimental trend. It is clear that the fit can be improved if the stator, which is a complex structure, is modeled with more degrees of freedom and if structural damping is also included. Anyway, a precise representation of the subsystem considered does not fall within the final objectives of the thesis. So, the previous 2DOF mechanical model has not been further investigated since it's introduction has been necessary only to give a numerical explanation to the antiresonance appearing in the experimental curve.

Finally, note that a perfect match between the FRFs can also be satisfied by considering a frequency-dependent damping which, starting from a constant value of 220Ns/m, increases with the frequency itself. This last observation is sufficient to understand why the diagram shown in figure 4.10 has been obtained during parameter estimation: since the stator oscillations has not been implemented in the equation 4.8, the viscous coefficient has inherited also its damping effect.

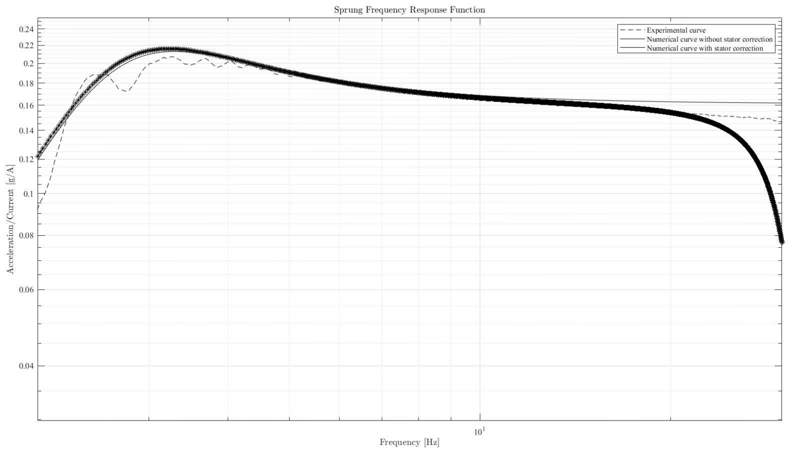

(a)

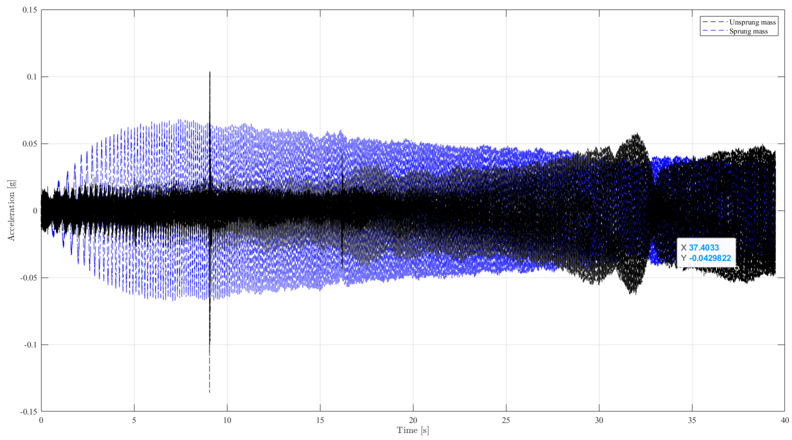

(b)

Figure 4.26: Dynamic measuring device at 0rpm curve fitting. a) Numerical FRF computed with the correction of the stator. b) Acceleration signals.

4.3.4 Levitatated electromechanical system curve fitting

It should be noted that the numerical models analyzed until now have revealed errors that have been prevent their perfect match with the physical results. On the other hand, this behavior had already been predicted, as stated several times, and moreover it should be remembered that the main objective of the thesis is always to provide an integrated numerical model which, taking into account both the electromechanical and electrodynamic behavior, allows to study and predict

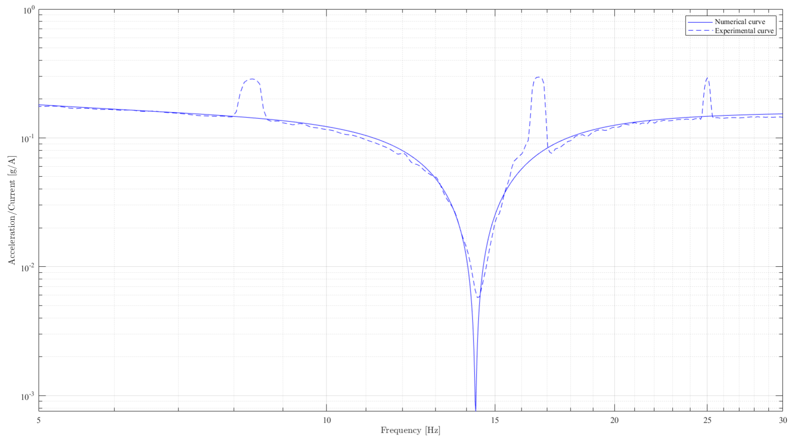

(a)

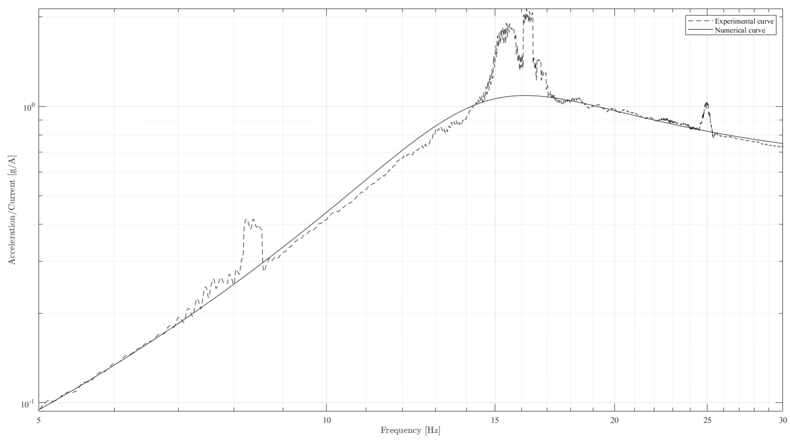

(b)

Figure 4.27: Integrated experimental test bench curve fitting at 500rpm without track irregularities in the numerical model. a) Sprung mass. b) Unsprung mass.

the dynamic instabilities. Finally, it should be emphasized that the previous fitting studies have somewhat improved the estimation of the identified parameters.

Considering that, the numerical and experimental Frequency Response Functions has been together reported in figure 4.27. The parameters involved during numerical simulations are the ones just tuned. It is worth to point out that the theoretical equations described in 3 match the experimental results with a great precision in the frequency range of interest (from 0 up to 30Hz). This conclusion is valid both for the sprung and unsprung mass curves. Also the strategy adopted to model

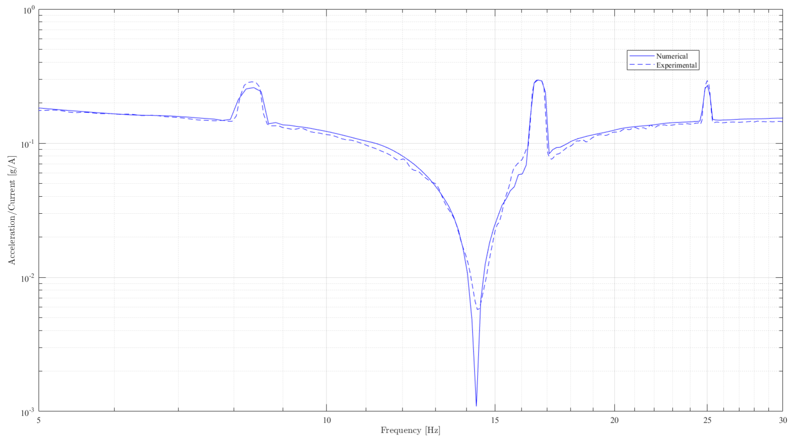

(a)

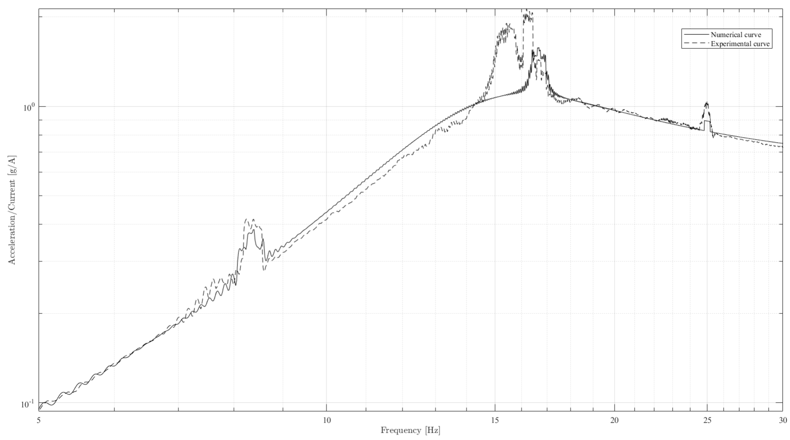

(b)

Figure 4.28: Integrated experimental test bench curve fitting at 500rpm with track irregularities in the numerical model. a) Sprung mass. b) Unsprung mass.

copper track irregularities proves to be effective. However, only the frequency curves without peaks can be considered as representative of the response of the system since only the acceleration signals due to the current are involved (figure 4.28).

Finally, it should be pointed out that the FRFs tends to drift out the frequency range of interest. Anyway, this condition has not been investigated either numerically or experimentally. The heating of the copper track as well as of the coil during the test, the possible variation of the offset, the vibration of the stator

Domain	Parameter	Value
Electromechanical	K_M	$25N/A$
Mechanical	m_{us}	$4.2Kg$
	m_s	$15.82Kg$
	k_{us}	$9700N/m$
	k_s	$4422N/m$
	c_{vc}	$220Ns/m$
Electric	R_{vc}	1.77Ω
	L_{vc}	$15.17mH$

Table 4.8: Tuned parameters.

and other unknown high frequency phenomena can lead the physical system to behave in a way not predicted by the numerical model, which is based on rigid assumptions instead.

Despite these observations, the integrated numerical model predicted by *Galluzzi et al.* [17] seems to have had experimental confirmation. Perhaps, the most important conclusion is to be found in the possibility of an electrodynamic levitation-based system to work in a linear manner.

All the tuned parameters to make the integrate model behave as the experimental test bench are collected in table 4.8.

4.3.4.1 Velocity effect

The integrated numerical model has been tested under different track velocity condition. First of all, note that the minimum speed required to lift the dynamic measuring device and the maximum one allowed by the test bench design are around 300 and 750 rpm. Thus, the investigation should be focused only into this rage. Actually, this analysis window should be restricted even more. In fact, due to the too small air gap values and the consequent excessive heating of the guide, the lower limit has been raised up to 450rpm; for safety reasons the upper limit has been set to 550rpm instead.

Figure 4.29 shows the variation of sprung and unsprung Frequency Response Function as speed increases. It is worth noting that, in the range considered, the effect of speed is negligible, contrary to what happens in the case of variations in the air gap instead.

The same results have been obtained experimentally. In figure 4.30 the Frequency Response Functions reveal the same trend with increasing velocity and only the motion of the peaks frequency due to copper track irregularities can be appreciated, as expected.

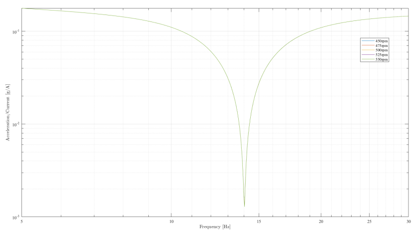

(a)

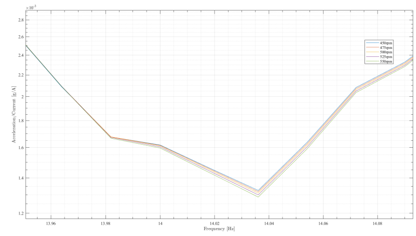

(b)

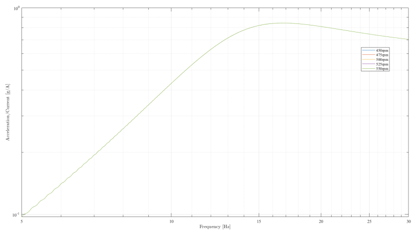

(c)

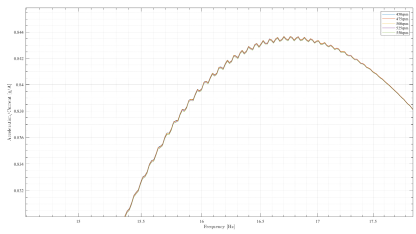

(d)

Figure 4.29: Numerical Frequency Response Function of the experimental test bench at different speed track. a) Sprung mass. b) Zoom in of the sprung antiresonance. c) Unsprung mass. d) Zoom in of the unsprung resonance

In this context, some words must be spent for the calculation of the FRF. The presence of peaks can shift the antiresonance frequency. This is due to a leakage effect, i.e. to a pure mathematical error. In fact, the copper track irregularities superimpose on the acceleration response of the system with respect of the current some harmonics with precise amplitude, frequency and phase. If the characteristic period used to compute the Fourier Transform does not match the characteristic period of the processed signal, a leakage effect occurs. Consequentially, the Frequency Response Function carried out could be affected by errors and show the antiresonance shifting depicted in figure 4.31.
As is well known from theory, this problem can be solved by adopting windowing and overlapping procedure. Thus, for the case study, the effect of velocity has been investigated by resorting to the operator H_1 as described in equation 4.14 as well as to an Hann type window and an overlap equal to one sixth of the total signal acquisition time.

Finally, the matching at different speed track velocity has been reported in figures at the end of the chapter.

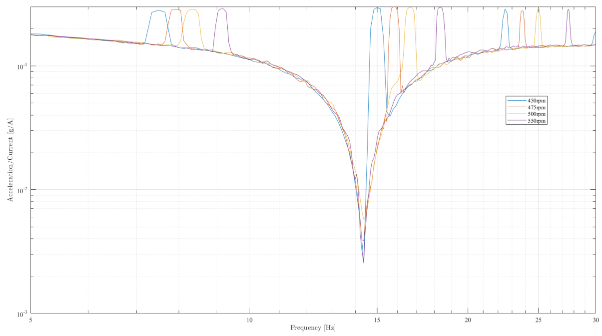

(a)

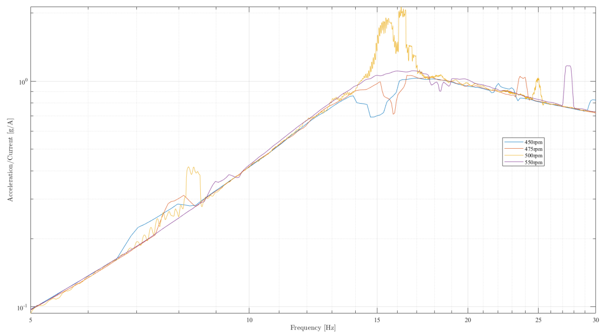

(b)

Figure 4.30: Experimental Frequency Response Function of the experimental test bench at different speed track. a) Sprung mass. b) Unsprung mass.

4.3.4.2 Root locus

The dynamic stability of the levitation electromechanical system can be studied by resorting to a root locus analysis both of the guideway track velocity and the electromagnetic damping. In particular, only mechanical poles are considered since these are mainly involved in this type of analysis.

The root locus of the system for the given damping at different speed spin is shown in figure 4.31a. It is interesting to note that the system tends to be unstable for velocity greater than rpm (m/s).

The effect of the damping on the amplitude of the real part of the pole is reported in figure 4.31b instead at the velocity of 500rpm. It is worth to say that an optimal damping of 156Ns/m can be computed. Moreover, it is possible to point out the value of naturals frequencies, equal to Hz.

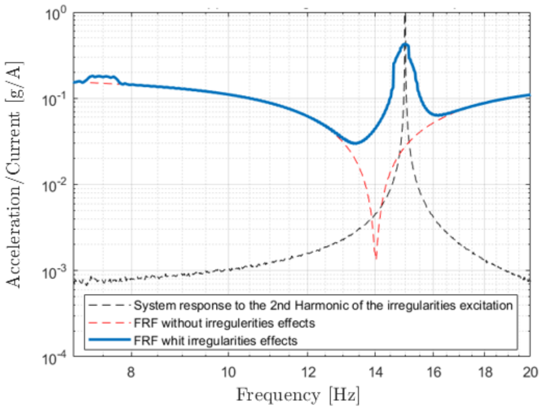

Figure 4.31: Leakage effect on the antiresonance.

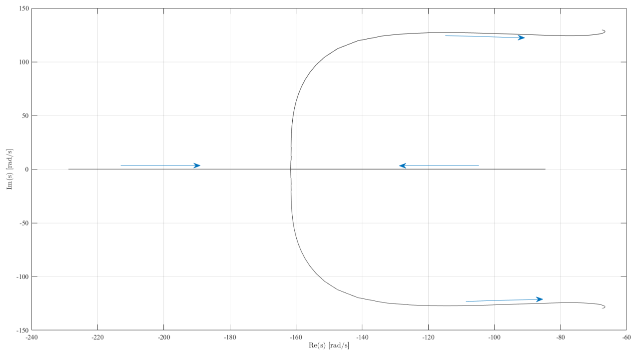

(a)

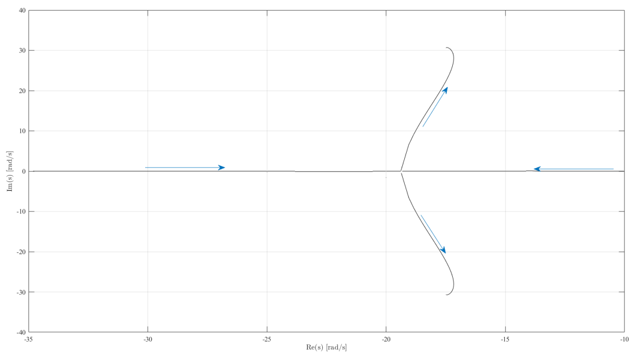

(b)

Figure 4.32: Root locus. a) Sprung mass mechanical pole. b) Unsprung mass mechanical pole.

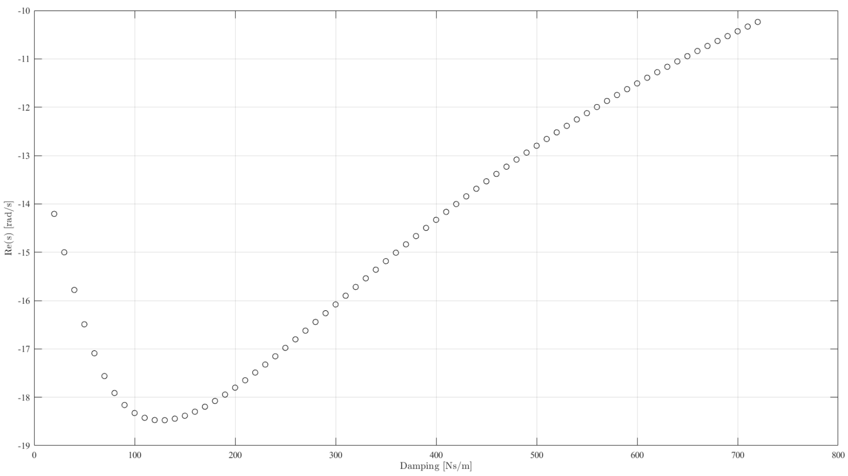

(a)

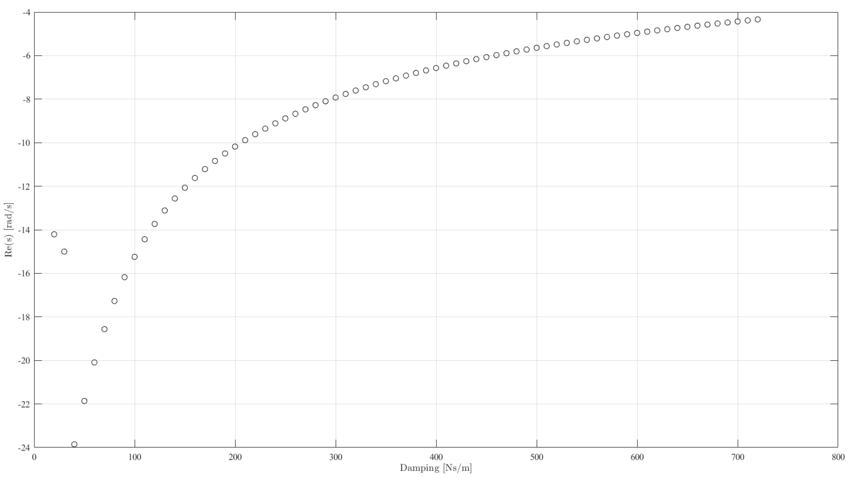

(b)

Figure 4.33: Effect of the damping on the real part of the poles. a) Sprung mass mechanical pole. b) Unsprung mass mechanical pole.

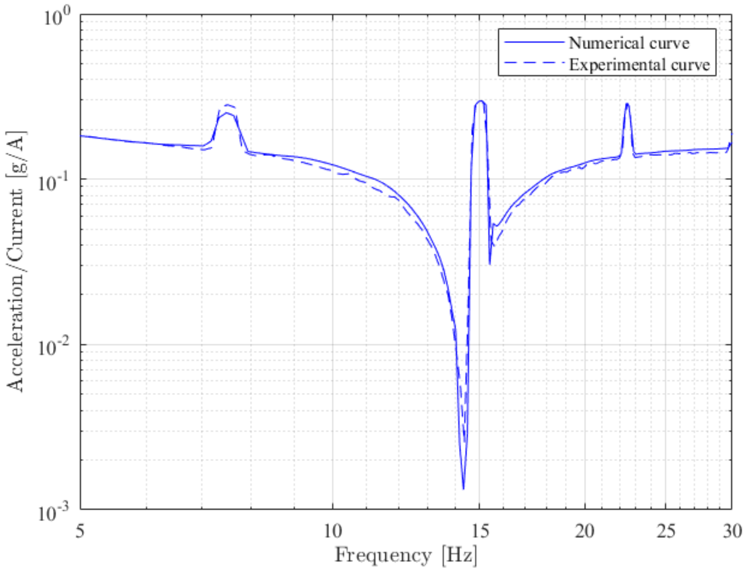

(a)

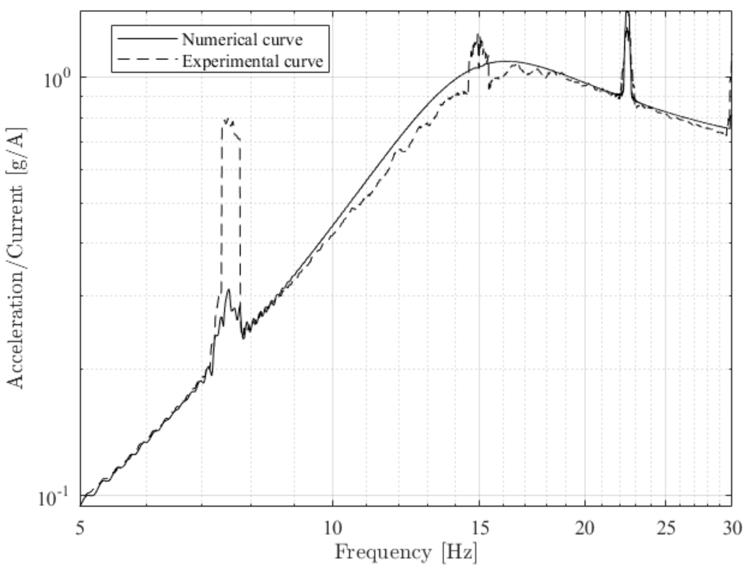

(b)

Figure 4.34: Integrated experimental test bench curve fitting at 450rpm with track irregularities in the numerical model. a) Sprung mass. b) Unsprung mass.

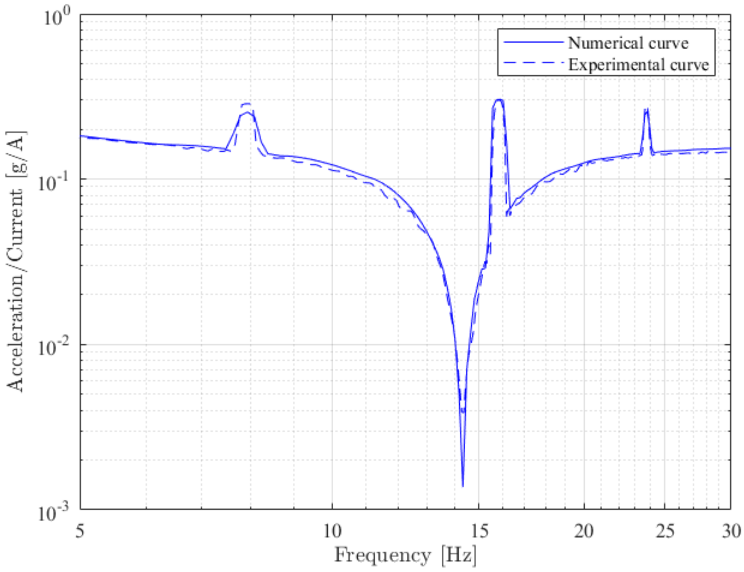

(a)

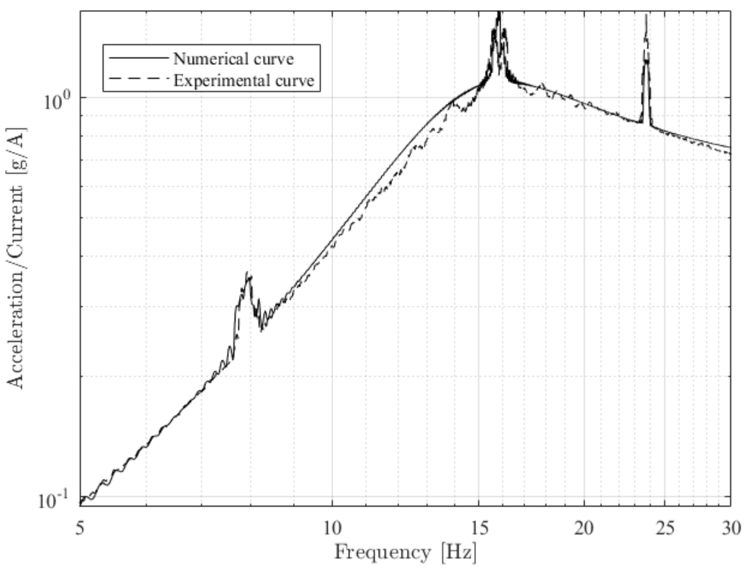

(b)

Figure 4.35: Integrated experimental test bench curve fitting at 475rpm with track irregularities in the numerical model. a) Sprung mass. b) Unsprung mass.

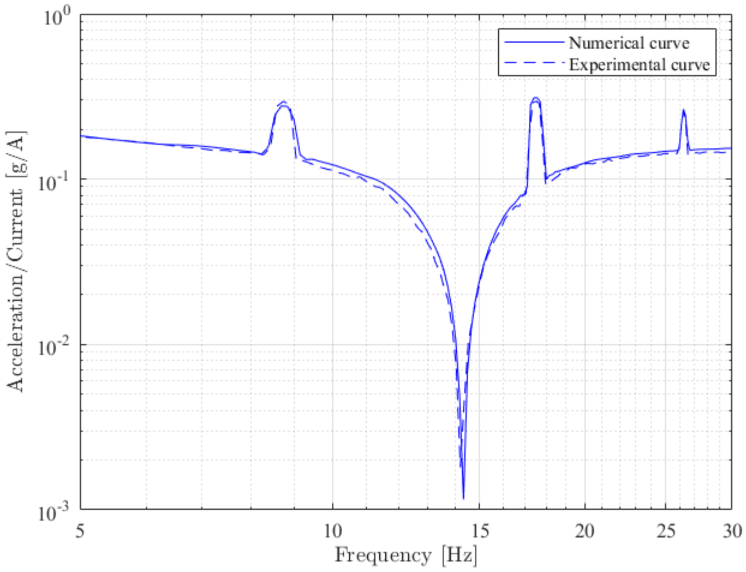

(a)

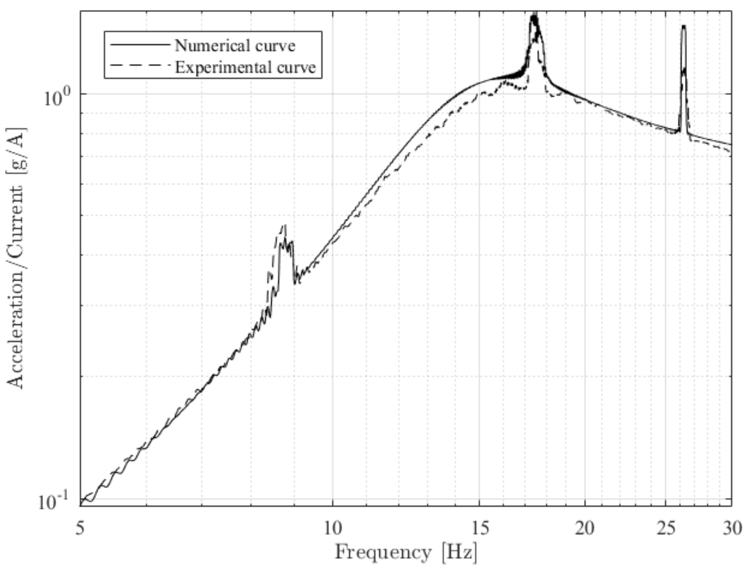

(b)

Figure 4.36: Integrated experimental test bench curve fitting at 525rpm with track irregularities in the numerical model. a) Sprung mass. b) Unsprung mass.

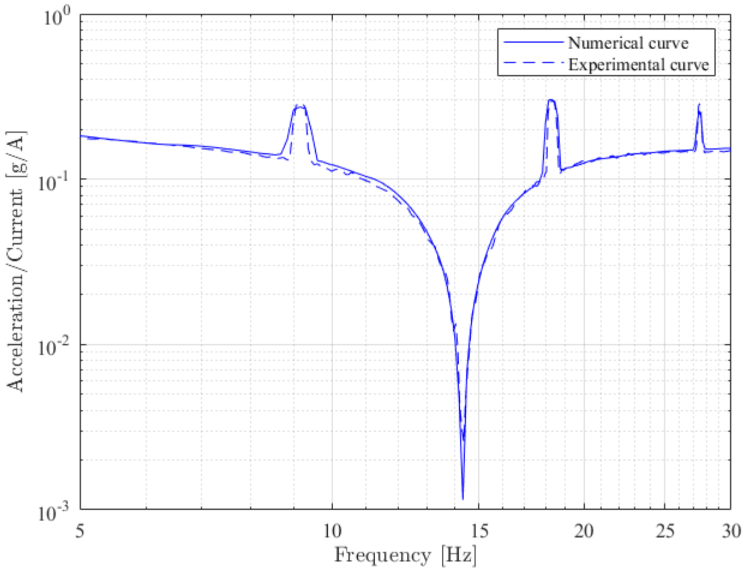

(a)

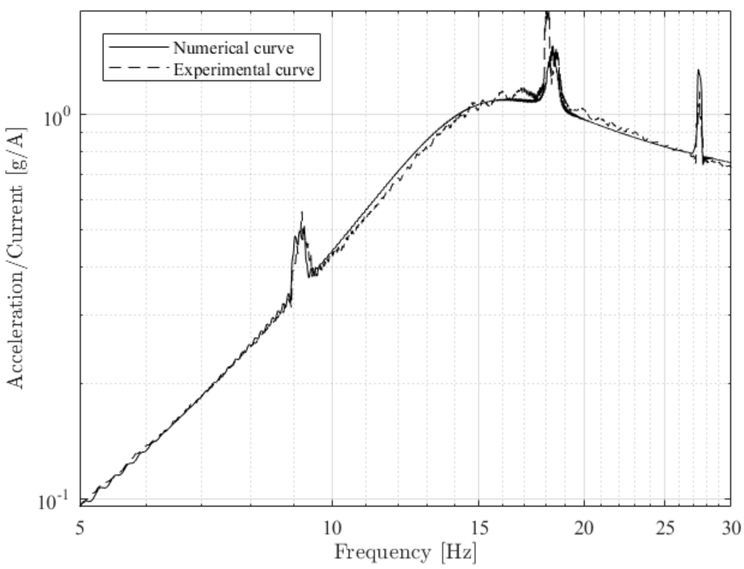

(b)

Figure 4.37: Integrated experimental test bench curve fitting at 550rpm with track irregularities in the numerical model. a) Sprung mass. b) Unsprung mass.

Chapter 5

Velocity estimation and control

At this point it is clear that the integrated model described in *Chapter* 3 has found its experimental correspondence in the measurement tests discussed and reported in *Chapter* 4. It is therefore possible to conclude that the behavior of the test bench is linear, when obviously all the described hypotheses concerning the temperature, the issue of the offset, the vibration of the stator, the effect of the dry friction and neglected magnets of the voice coil and so on are respected. Linearity is certainly a very important property that allows to exploit not only the principle of superimposition of effects and proportionality but also to implement simple linear controls.

On the other hand it is true that, although the responses in the frequency domain are superimposable, driving the system to follow a certain trend requires a lot of precision in knowing the signals over time that the system itself communicates. For this reason, the knowledge alone of the Frequency Response Functions does not allow a priori to be able to control the system without distinction without certain critical issues arising. When it comes to control, it would be preferable to be able to take advantage of a model that is based on the theoretical results obtained and which ensures real-time information about the state of the plant. This aim can be fulfilled, for example, by implementing an observer, like the ones introduced in *Chapter* 3 .

The following paragraphs are dedicated to the validation of an observer that is based on the theoretical model identified in *Chapter* 4 and that manages to work in parallel with the dynamic measurement instrument providing an accurate estimate of the current and the relative velocity between the two body. The former are very important so it allow to enter the logic of a current closed loop control; the second, on the other hand, could be useful for implementing a first control which, based on the knowledge of the relative speed itself, may or may not provide that amount of suitable damping which ensures greater stability and better passenger comfort. Regardless of the objective to be chosen, it is clear how fundamental the identification of an observer is.

5.1 Equipment setup

The need to validate an observer requires that it can be simulated in real time. Furthermore, this must be able to receive data, both analog and digital, to be processed in order to provide an estimate of the state of the system through the reference model of the observer itself. It is clear that the previously introduced equipment for signal acquisition turns out to be inadequate for the present case because it appears to be too static. Moreover, open loop control doesn't allow for feedback that corrects itself based on what is happening in the system.

In order to achieve the objectives stated at the beginning of the chapter, it has been advisable to replace the *Scadas Mobile LMS acquisition system* with the *dSpace MicroLabBox*, i.e. a microprocessor able to receive and send signals, as well as processing a basic program and communicating with other processors. The introduction of the *dSpace* has led to quite a few problems as it was necessary to solve the communication problems with the Launchpad which, in the meantime, continued to manage the control of the voice coil. One can thick that *MicrolabBox* could replace it as they are both microprocessors. In practice it was decided to keep both in the test bench. In fact, the LaunchPad has the advantage of easily integrating a *BOOSTXL-DRV8323Rx* for actuator power control; on the other hand, however, the *MicrolabBox* is a much more performing microprocessor, with more accessible graphics and which better manages the acquisition of signals. Therefore, the problem of communication between the two arose.

Finally, it should be noted that both work in the *C language* but fortunately they have extensions that allow the program to be written in advance using Simulink®.

5.1.1 Closed loop current control

From the voltage control that characterized the experimental identification phases, it is necessary to move on to a current control. In fact, it is a much faster type of control that is well suited to the system in question which can be implemented in

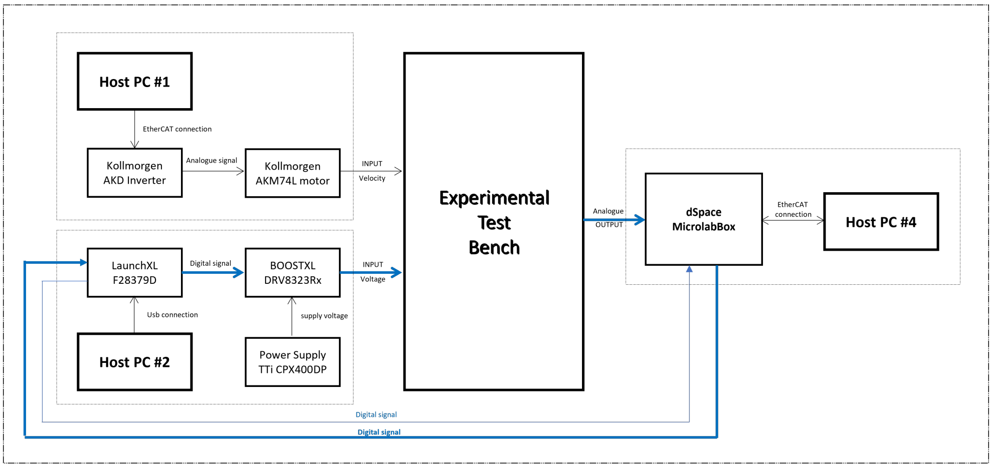

Figure 5.1: Sketch of the equipment used to validate the observer and control actively the voice coil.

current through a voice coil whose characteristic parameter (K_m), which allows the passage from the domain electrical to mechanical, is known with precision. Refer to figure 5.1 to better understand the closed circuit created (blu one).

As always, there is a *Host PC n. 1* which, through the *Kollmorgen Workbench software*, drive the inverter of the electric motor rigidly connected to the copper track.

Host PC n. 2 creates the program and manages the inputs of the LaunchPad. Essentially, the functions performed are the same as those of the open loop control, with the difference that in this case the reference signal is given in terms of current. Obviously the ultimate goal is always to estimate the CMP, i.e. the input that allows the *BOOSTXL-DRV8323Rx* to modulate the power supply voltage to the value that then guarantees the desired current. This passage is made possible by a *PI control*, whose constants have been tuned for $K_p = 3.77mH$ and $K_I = 222.42\Omega$. This is essentially an inverse RL circuit simulated by a controller, i.e. the PI.

The *Host PC n. 4* is connected by etherCat communication with the dSpace Microlabbox. It has the task of deploying the script program in the microprocessor containing the model of the observer being able, at the same time, to acquire the signals and display them thanks to the *ControlDesk software*. The acquired inputs are then processed as indicated by the script.
The roles of Host PCs have been separated to better explain the equipment setup: actually LaunchPad and MicrolabBox have been controlled by the same computer.

In this case, it is not necessary to focus excessively on the type of input and output. It is essentially a question of communicating a current value to the voice coil via the LaunchPad. This value is the sum of two contributions (figure 5.2):

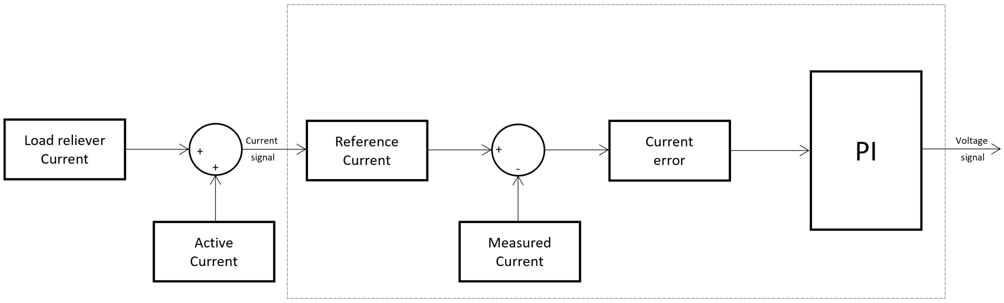

Figure 5.2: PI action.

1. Load reliever to balance the weight;
2. A reference value to implement the desired current control.

The outputs, as seen, are directly managed by the MicroLabBox, which processes them to estimate the states of interest (which could be precisely the relative speed) and provide the mentioned reference to the launchpad. It is precisely this feedback which defines a loop closed on itself.

5.1.2 Communication issues and solution

Most of the time spent to achieve the objectives set at the beginning of the chapter has been dedicated to identifying an effective communication protocol between the microprocessors. But proceed in order.

Based on what has been seen in the observer theory, whether it is an RL or a Kalman Filter, the signals to be acquired are those of:

1. Voltage;
2. Accelerations;
3. Current.

The simplest idea, which was the one initially followed, is to connect the accelerometers directly to the dSpace, but not before having conditioned them since this microprocessor does not know the *PCB communication protocol*; in the same way, the current measured by the clamp was sent directly to the input modules of the MicrolabBox together with the voltage signal extracted from a suitable DAC of the launchpad. This type of communication proved to be completely ineffective due to an inevitable background noise. This is related to the switching of the BOOST H-bridge. The resulting magnetic disturbance influences the analogue signals leading to the appearance of peaks at intervals of 20kHz (operating frequency of the

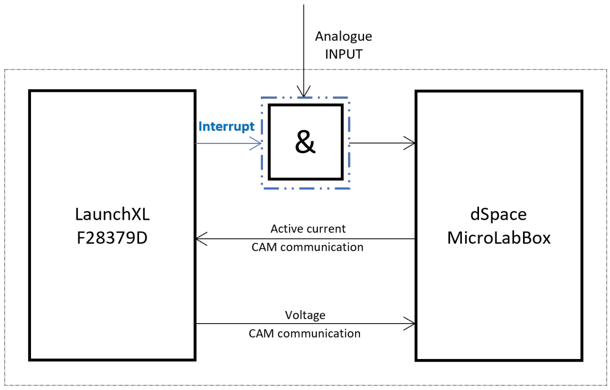

Figure 5.3: Communication between LaunchPad and MicroLabBox

launchpad). These peaks make the signal unusable in any way.

The communication has been resolved by providing a **CAN** (**C**ontroller **A**rea **N**etwork) communication protocol together with an *Interrupt signal*. The first is the channel through which it has been decided to exchange the voltage signals from launchpad to dSpace and the current reference in the opposite direction. The CAM communication has required the definition of a suitable *.dbc file* for the digital coding and decoding of the exchanged signals. Therefore, it is a question of defining the number of bytes containing the information, mapping the signal and becoming familiar with the operating blocks that allow CAN communication both on the LaunchPad and on the MicroLabBox side. The advantage of the CAN connection is that, since this exchange of messages is purely digital, it is not affected by the switching of the Boost. Furthermore, it is a very robust communication line if it is considered the simplicity of the studied system.
This protocol can solve the problems in the current and voltage acquisition of the dSpace which, being both managed by the outgoing LaunchPad, can be easily digitized. The same cannot be said for accelerations which arise as pure digital signals and for which CAN communication offers no solution.

The use of an *interrupt* has been certainly the intuition that made it possible to obtain optimal data acquisition. It is essentially a digital signal that can trigger a downstream operator. The idea then has been to generate a continuous interrupt signal in correspondence with the closing period of the H-bridge switches in the launchpad to enable the reading of analog signals in dSpace. Consequently, whenever the switches open or close, the acceleration signal is not read and the magnetic noise is not detected. One may think that in this case the acquired signal is discontinuous, however, it should be also remember the high frequencies at which the launchpad works.
Speaking of frequencies, the generated interrupt has a frequency that is half that of the launchpad, which is why a 10kHz working frequency has been assigned to the

dSpace. In addition, the 12V constant power signal of the power supply has been increased up to 16V. This is because the voltages involved in the system are close to the maximum permitted. Now bear in mind that the load reliever alone leads to a voltage of 10.5V. It follows that the period of the counter to have a signal almost equal to the maximum is very short and consequently the switching can be so rapid as to generate an interrupt signal which does not work correctly.

In figure 5.3 the communication between the two microprocessors is clarified in a schematic way.

5.2 Observer efficiency

Once the hardware part in which to implement the observers is clear, it is advisable to have confirmation of the effectiveness of the models behind them. Note how, unlike what happened for the identification of the mechanical system in which the post-processing phase was massive, in this case the validation must take place in real time. Despite this, in order to have a minimum prediction, it has been decided to carry out numerical simulations in Simulink® environment.

5.2.1 Numerical simulation

In order to simulate the effectiveness of the observers, it has been decided to replicate the real plant in a Simulink® environment. It has been essentially a question of defining a circuit of blocks which implemented the equations of the integrated model with the possibility of managing non-linearities. In particular, it has been decided to introduce:

1. A resistance that increases over time with temperature;
2. A completely different inductance between the plant model and that of the observer.

In fact, these are two phenomena that surely would have met during the experimentation phase. It is clear that not introducing imperfections would have made no sense since it would have led to an observer with a practically exact model. Therefore, the outputs of the simulated plant constitute the inputs of the observers for the estimation of relative velocity and current.

The figures that follows show some simulation results for the RL observer, the standard and the extended Kalman Filter. The parameters of the models implemented in the observatories are those collected in table 4.8, while those of the plant simulator have been chosen completely randomly. Finally, to study the models, it has been decided to excite the simulated plant with a chirp signal in addition to the irregularities of the copper track and some impulses in force. In general, all

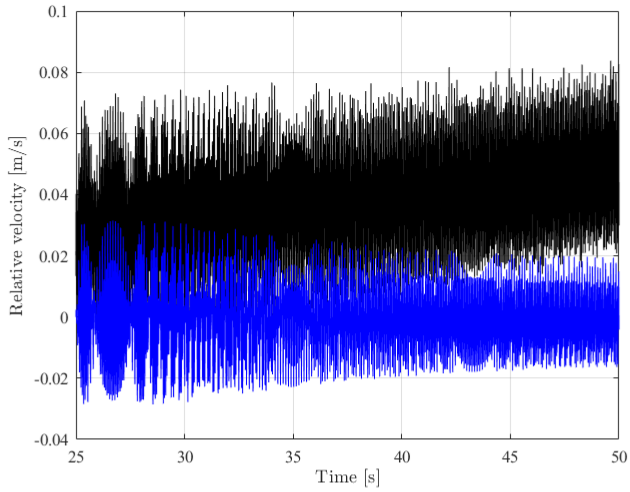

Figure 5.4: Numerical simulation results in term of relative velocity for the RL observer. The blue line refers to the observer state variable; the black one to the plant simulator.

models seem to react to the presence of an impulse, more or less quickly.
Note from figure how the RL observer fails to follow the system. This result should not surprise as the effectiveness of such an observer depends only on two parameters, resistance and inductance. Quests, however, are different and vary over time, so the calculation scheme has no possibility to follow the plant. Furthermore, several simulations have identified the increase in temperature as more problematic. In fact, this alone can lead to a completely wrong estimate of the relative speed, which obviously increases to recover the current mismatch between the observer and the system. As if this were not enough, the increase in resistance leads to a phase shift of the signals.

Even the standard Kalman Filter seems to show weaknesses when the parameters are completely changed. However, unlike the RL observer, it is possible to predict uncertainties or noises in the model to bring the estimate closer to the real one. For example, it can follow the decreasing of the mean value of the current very well. However, not much time has been spent on this solution, as the standard Kalman Filter has been defined as requiring all the inputs that characterize the real system. It is clear that until now a direct measurement of the lift force, which is one of those that excites the system, has not been introduced. The presence of a fast and rapid electrical equation in the model would allow the standard Kalman filter to predict the effect of this lift force, but equally it has been decided to abandon this model in favor of the extended Kalman filter which, without any tuning of the particular parameters, manages to follow the numerical imperfections introduced. This is thanks to the augmented variable that takes on the responsibility of managing these shortcomings. Finally, it should be pointed out that for the estimation of the Kalman gain the minimization of a particular cost function has been used which, starting from the one defined in chapter 3, adds a term J_{add} capable of minimizing the noise, such that

$$J_{add} = \rho[B]_d[B]_d \tag{5.1}$$

where ρ is a parameter which, if it increases, makes the system more stable (fundamental in a close loop logic) but with less noise rejection. In any case, the theoretical details of this addition have been glossed over by adopting a pure user approach.

5.2.2 Real time validation

If the reference toward which validating an observer from a numerical point of view is clear, the same cannot be said from an experimental point of view. Here it is necessary to rely on the measures and not only. In fact, the current is acquired as such by the current clamp and can be directly compared with the estimated analogue; the same cannot be said for the relative speed because there is no direct measurement. Thus, integration is necessary and this, as is known, brings with it numerous problems, first of all drifting. In fact, the acquired signals never have zero mean, so the constant integration leads to an increasing (or decreasing) trend of the result. This problem has been solved by introducing a bandpass filter with cut-off frequencies at 0.1Hz and 1000Hz to eliminate constant or weakly time-varying terms without introducing excessive phase delay.

Once the reference signal has been defined, it has been possible to proceed to build the scripts in the MicroLaBox and start a simulation in real time.

Although the ineffectiveness of the RL observer had already been demonstrated at a theoretical level, this solution has been tested the same for the possibilities of being able to implement a *sensorless* control (the RL does not need acceleration signals). Furthermore, the theoretical analysis has made it possible to improve the observer's effectiveness by predicting a resistance value that is updated following the average of the acquired signal. In fact, dealing with periodic signals it has been not difficult to introduce a simple moving average to achieve this purpose. This arrangement is absolutely not suitable for transients. However the solution has been tested out of curiosity.

Figure 5.6 shows some images of these tests. In particular, figure 5.6a refers to the case in which the voice coil was energized with a constant frequency of 10Hz at a speed of 0rpm (no levitation). Therefore, the conditions of an electromechanical system with only one mechanical degree of freedom have been replicated. It should be observed how in this case the observer RL is able to follow the system very

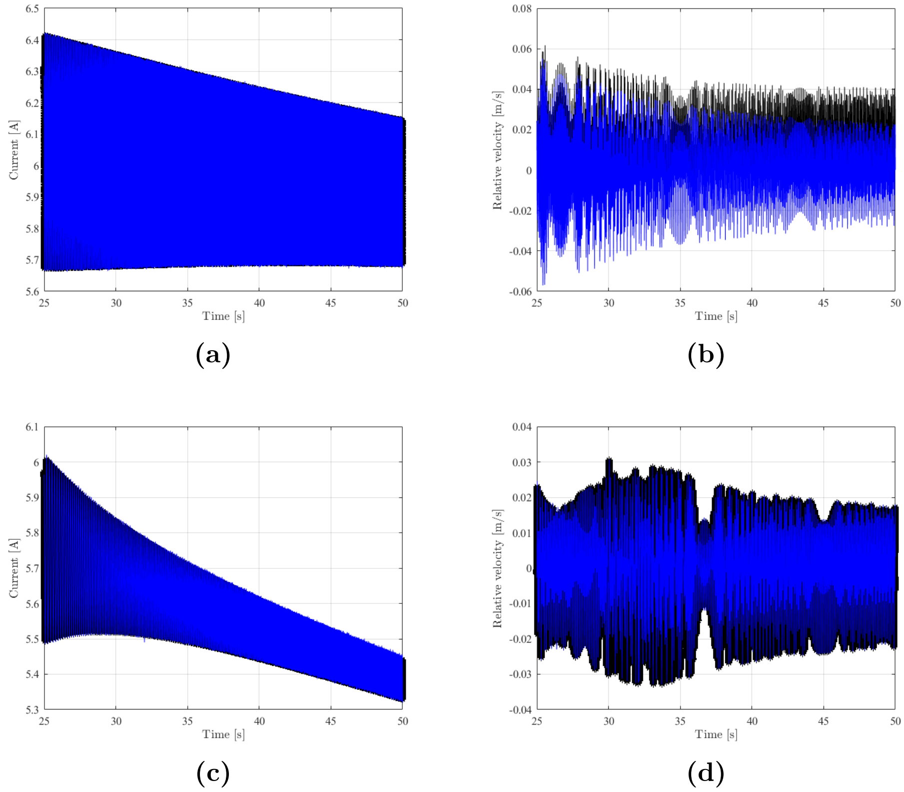

Figure 5.5: Numerical simulation result for the Kalman filter observes. a) Estimated and simulated current of the standard Kalman filter. b)Estimated and simulated velocity of the standard Kalman filter. c) Estimated and simulated current of the extended Kalman filter. d)Estimated and simulated velocity of the extended Kalman filter. The blue line refers to the observer state variable; the black one to the plant simulator.

well. This result shouldn't come as a surprise as the resistance is corrected in real time while the inductance used is precisely the one that in figure 4.24b ensures the coincidence between the experimental and numerical Frequency Response Function. In fact, by changing the frequency value or even providing for a different excitation, the observer's estimate RL fails, as shown in figure 5.4b which refers to the levitating system subjected purely to the excitation of the irregularities at 500rpm. In any case, all this should make us reflect on the power of sensorless observatories.
There is not much to comment on the effectiveness of the extended Kalman Filter which, as mentioned several times, manages to take into account all the imperfections by playing on the noise and above all on the augmented variable, as evident in figure 5.11.

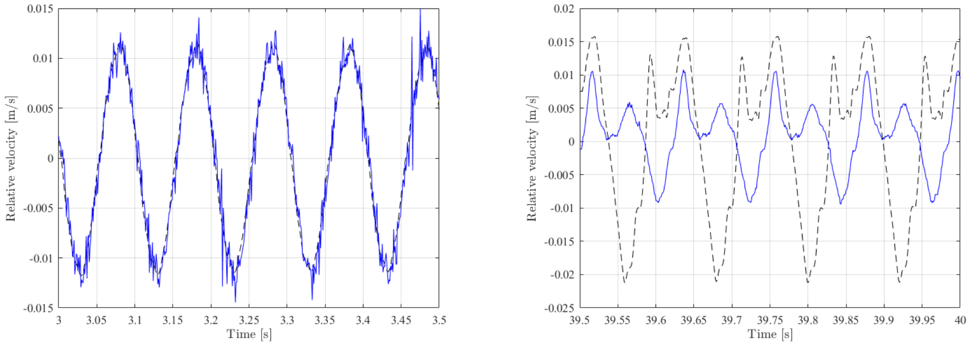

(a) **(b)**

Figure 5.6: Real time validation of the RL observer. a) SDOF mechanical system under a sinusoidal excitation at 10Hz. b) Levitated 2DOF mechanical system at 500rpm. he blue line refers to the observer state variable; the black one to the plant simulator.

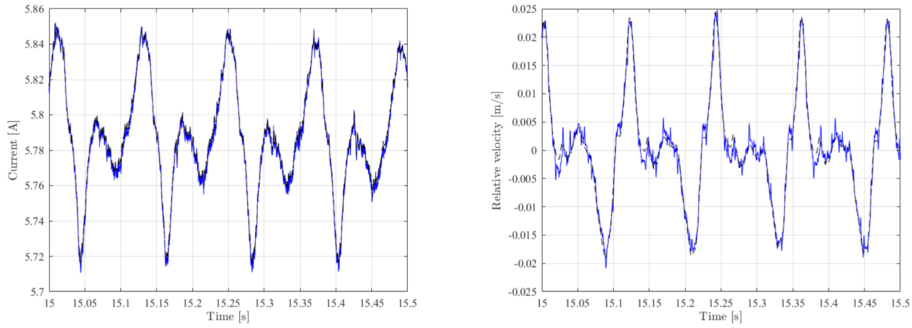

(a) **(b)**

Figure 5.7: Real time validation of the extended Kalman filter observer for the levitated system at 500rpm. a) Current. b) Relative velocity. The blue line refers to the observer state variable; the black one to the plant simulator.

Table 5.1 shows some of the parameters tuned to improve the efficiency of the observer. It should be noted that, due to the many uncertainties, the noises on the variables have been increased with respect to those of the measurements to push the filter to trust more the physical signal rather than the model, which, as we know, is valid under strict hypotheses. Also, the noise value on the augmented variable has been raised to make the system more responsive; the ρ parameter was set at the value shown in the table on the basis of work on previous topics.

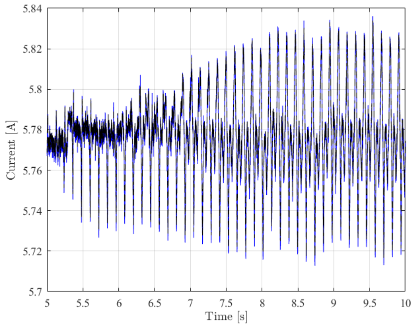

(a)

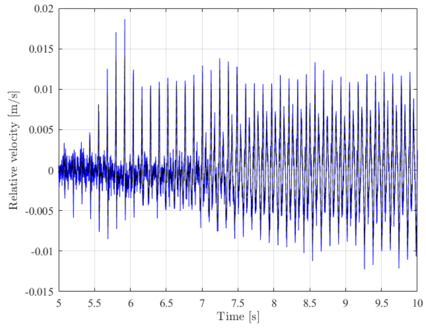

(b)

Figure 5.8: Real time validation of the extended Kalman filter observer for the levitated system when approaching the copper track at 500rpm. a) Current. b) Relative velocity. The blue line refers to the observer state variable; the black one to the plant simulator.

Figures 5.8, 5.9, 5.10 and 5.11 also show a succession of transients and disturbances that the extended Kalman is able to follow very well.

	States			Measurements	
Variable	**Noise**	**Value**	**Variable**	**Noise**	**Value**
z_{us}	$w_{z_{us}}$	0.0001			
z_{us}	$w_{z_{us}}$	0.0001	z_{us}	$v_{z_{us}}$	0.00001
z_s	w_{z_s}	0.0001			
z_s	w_{z_s}	0.0001	z_s	v_{z_s}	0.00001
i_{vc}	$w_{i_{vc}}$	0.00001			
i_{aug}	$w_{i_{aug}}$	0.1	i_{vc}	$v_{i_{vc}}$	0.00001
-	ρ	0.05			

Table 5.1: Extended Kalman filter tuned parameters.

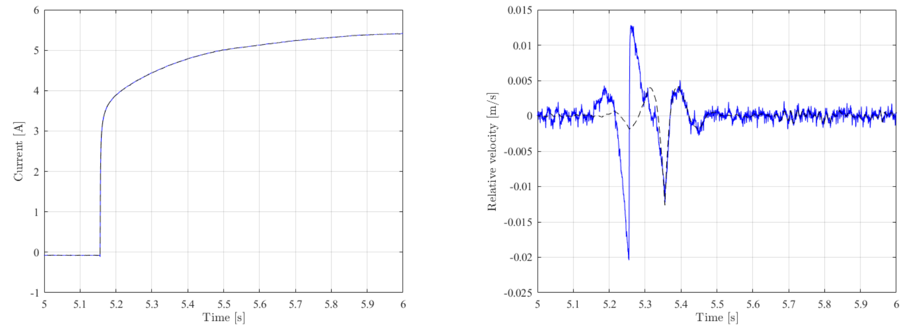

(a) **(b)**

Figure 5.9: Real time validation of the extended Kalman filter observer for the levitated system when the load reliever is applied. a) Current. b) Relative velocity. The blue line refers to the observer state variable; the black one to the plant simulator.

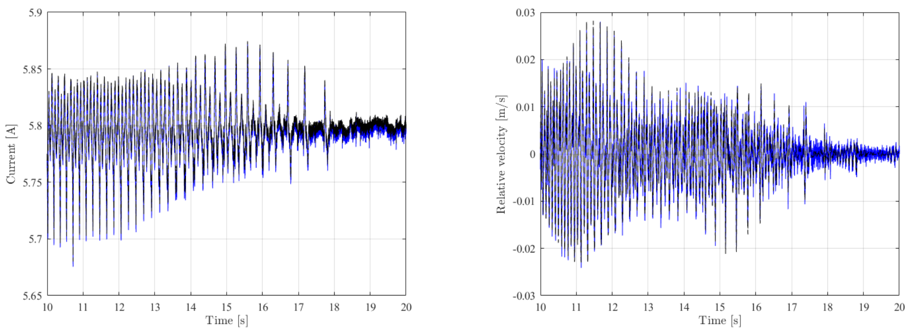

(a) **(b)**

Figure 5.10: Real time validation of the extended Kalman filter observer for the levitated system when the track stops. a) Current. b) Relative velocity. The blue line refers to the observer state variable; the black one to the plant simulator.

5.3 Brief discussion on the active control implementation

In this last paragraph it is briefly mentioned the active control that since the design of the test bench has been placed among the first to want to implement. In particular, the goal is to bring the system to work in the minimum oscillation condition, which is the one in which the damping is minimal or optimal. In fact, it is possible to actively impose damping because in the control under consideration

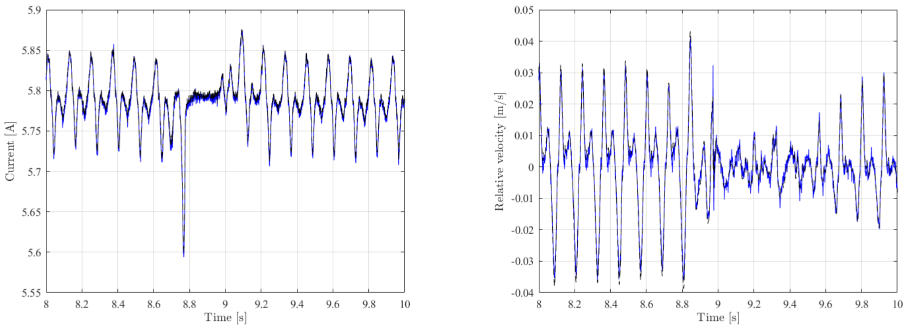

(a) **(b)**

Figure 5.11: Real time validation of the extended Kalman filter observer for the levitated system when a generic force is applied to the sprung mass. a) Current. b) Relative velocity. The blue line refers to the observer state variable; the black one to the plant simulator.

the current enters the mechanical domain directly as a force. Therefore, if this current is made proportional to the relative speed, the system can be excited with a damping force. Hence the reason linked to the estimate of the relative speed so much sought after in the observatories should be clear. Knowing the relative speed and knowing the optimal damping from the studies of the root locus, it is necessary to enter the system by supplying just the amount of damping force that is missing to reach the optimum condition. Therefore, the formula 3.72 holds.

In this active control a closed circuit is more necessary than ever and that the poles, especially those of the observer, have a negative real part. While this was not a difficult condition to implement, implementing this control proved unsuccessful. This is because the amount of damping to be added leads to a current value which is in the order of magnitude of the ripple of the current signal itself. For which in fact, experimentally, it has not been possible to see a variation of the oscillations of the accelerations. A variation was recorded by imposing optimal dampings in the order of thousands, but obtaining the opposite effect of increasing the oscillations.

Therefore, this active control implemented would require reviewing the setup of the equipment used, from the methods of acquiring the signals to those of processing. This could be a good starting point for future work. At the level of this thesis, we stopped at the identification of the system and the observer.

Chapter 6

Conclusions and further studies

The problem of the dynamic stability of electrodynamic suspensions has been revised through a review of the past literature and by the need of the current mobility problems. The *Hyperloop Transportation Technology* face this problem since is it still unresolved both from a theoretical and pragmatical point of view. In the first case, models developed in the past have proved the dynamic instability at higher velocity and the propensity of the EDS at reducing its intrinsic damping, but no match with experimental data at different scale has been obtained; on the other hand, different scale experimental test bench have shown directly the dynamic instability driving the scientists at finding the possible causes, but no theoretical proof is still available and, furthermore, it is not clear why large scale electrodynamic levitation-based prototype are not affected by instability.

In this thesis work an experimental test bench for the study of electrodynamic levitation phenomena has been introduced and described in parallel with a customized integrated numerical model. Aware of the difficulties encountered by research in the past and of what has been explained in the introduction, having succeeded in validating the theoretical model experimentally in such a way that it behaves similarly to the physical system, can open the doors to theoretical predictions that have a greater probability of success thanks to the experimental validations itself. On the other hand, as explained during the discussion, this matching is based on rigid hypotheses and the range of validity is very narrow. In fact, different non linearities are present in the test bench, not only because of the active actuator, vibration of stator, dry friction and increasing of temperature, but also because of the EDS system itself. It should be remembered that it behaves in a non-linear way and that the model used in the numerical simulation is a linearization around an equilibrium air gap.

The results obtain don't want to be definitive. Great approximation in the measuring strategy as well as in the extraction parameters method have led to an estimation that is poor in the most of case. Since non-linear effects and complex physics (as for example the effect of the magnet in the electric domain of the voice coil actuator) have been neglected, the unknown parameters have brought with their estimation all these uncertainties. Despite this, it should be emphasized that the study of the parameters in an approximate way has in any case allowed us to have starting points for the matching between the experimental and numerical curves of the model proposed by *Galluzzi et al.* [17]. In many cases the trend of the error and the behavior of the variables was clear, which allowed us to act in a targeted manner, understand the mechanism and provide the most appropriate corrections. This is the case of the inductance and the damping. In particular, the first variable is clear the critical parameter of the model since it affects the value of the optimal damping and should alone takes into account the effect of voice coil magnet in the electric circuit. However, two values have been proposed depending on whether one wishes to work precisely at low frequency or to have a rough estimate throughout the frequency range. These are two better situations than if using the static value that the actuator presents in the absence of magnets. On the other hand, the mechanical parameters (except for the damping) can be considered with great reliability since no rough approximation have been made during modelling and measuring activity.

Experimental analysis and theoretical modelling have met finally in the last chapter where the fitting between Frequency Response Functions has been obtained successfully. This is a great conclusion since confirm the linearity that is the base of the model studied. Moreover, since the instability can't be appreciated experimentally because of the constant presence of damping in the springs as well as in the EDS system, it can be predicted by the model itself. This prediction can be considered quite accurate since it is based on experimental validation, as long as the conditions are met.

This thesis is not intended to be self-contained, but is part of a larger project between *Politecnico di Torino* and *HTT* and started from theoretical assumption and the design of the test bench. Here the dynamics has been tested, discussed and analyzed. The comparison with the previous works from which this thesis took its cue has been fundamental, from the setup of the measuring equipment up to the main issues in dealing with the real counterpart of theoretical model. As has been done, the following work could also be the starting point for future developments aimed at grasping more complex dynamics or even at improving the accuracy of the results reached up to now. It is in this context that becomes interesting to speculate about the future.

From a purely theoretical point of view, a test bench for electrodynamic suspensions that is well represented, in compliance with its hypotheses, by a model that is able to work in parallel with the bench itself and estimate the quantities of interest is now available. The way in which the physical system reacts to current stresses is well described by the identified FRFs. Therefore, one can think both of improving the accuracy of the results but also of implementing current controls. The presence of an active electric actuator allows, in fact, to have full leeway. Certainly, a study aimed at the project as a whole is also the analysis of passenger comfort, which can be both studied, predicted and controlled. What can be done with controls is only limited by the imagination.

From a more practical point of view, this is an interesting result for companies operating in the rail transport industry. This is not due to the result achieved in an absolute sense, but above all because perhaps a way has been found to be able to study the problems of magnetic instability, both from a theoretical and an experimental point of view. It is clear that before seeing a vehicle similar to the hyperloop concept on the market, it will take some time. There are still many aspects to analyze: the effect of speed, what happens in the case of large-scale models, better understanding the intrinsic damping of the electrodynamic suspension, dealing with non-linearities and, in general, all those problems that will crop up in the tackle such a complex and still not well known problem. What is certain is that the advantages linked to discoveries in this field can lead to the implementation of advantageous transport systems. This is precisely the case with the Hyperloop.

This thesis work that we want to conclude now leaves room for further studies and reflections, from the critical and more technical discussion of the results obtained up to a provocation with a broader perspective: in the modern context, where the search for innovative and sustainable solutions in the field of mobility and transport has become one of the main character, in which interesting and emerging solution able to deliver speed and sustainability to transport people and cargo alike are followed and where engineering should face and support technical issues, is the Hyperloop the answer? It was only a theoretical speculation and year after year the discoveries in the scientific field are increasingly making this technology tangible. Here, no answer is given, preferring to motivate continuous researches, to which this thesis hopes to have given even a very small contribution.

Appendix A

State space matrices

In these sections the state space matrices used to represent physical systems analysis and to run numerical simulation are summarized.

A.1 Electrodynamic suspension

The state variables are so arranged

$$\{Z\}_{EDS} = \{i_{1,d}, i_{1,q}, i_{2,d}, i_{2,q}, z_{in}, \dot{z}_{PM}, z_{PM}\}^T \tag{A.1}$$

while the input of the system can be written

$$\{U\}_{EDS} = \{\dot{z}_{PM,in}, f_{PM}\}^T \tag{A.2}$$

and the output as

$$\{Y\}_{EDS} = \{\ddot{z}_{PM}\}^T \tag{A.3}$$

Under this assumption, the dynamic matrix $[A]_{EDS}$ can be written as

$$\begin{bmatrix} -\omega_{1,p} & \omega & 0 & 0 & 0 & \frac{\Lambda_0}{\gamma L_1} e^{-\frac{z_{PM,0}}{\gamma}} & 0 \\ -\omega & -\omega_{1,p} & 0 & 0 & -\frac{\Lambda_0}{\gamma L_1} e^{-\frac{z_{PM,0}}{\gamma}} & 0 & \frac{\omega\Lambda_0}{\gamma L_1} e^{-\frac{z_{PM,0}}{\gamma}} \\ 0 & 0 & -\omega_{2,p} & \omega & 0 & \frac{\Lambda_0}{\gamma L_2} e^{-\frac{z_{PM,0}}{\gamma}} & 0 \\ 0 & 0 & -\omega & -\omega_{2,p} & -\frac{\Lambda_0}{\gamma L_2} e^{-\frac{z_{PM,0}}{\gamma}} & 0 & \frac{\omega\Lambda_0}{\gamma L_2} e^{-\frac{z_{PM,0}}{\gamma}} \\ 0 & 0 & 0 & 0 & 0 & 0 & 0 \\ -\frac{2\Lambda_0}{\gamma m_0} e^{-\frac{z_{PM,0}}{\gamma}} & 0 & -\frac{2\Lambda_0}{\gamma m_0} e^{-\frac{z_{PM,0}}{\gamma}} & 0 & 0 & 0 & 0 \\ 0 & 0 & 0 & 0 & 0 & 1 & 0 \end{bmatrix} \tag{A.4}$$

The input gain matrix $[B]_{EDS}$ is thus

$$\begin{bmatrix} -\frac{\Lambda_0}{\gamma L_1} e^{-\frac{z_{PM,0}}{\gamma}} & 0 \\ 0 & 0 \\ -\frac{\Lambda_0}{\gamma L_2} e^{-\frac{z_{PM,0}}{\gamma}} & 0 \\ 0 & 0 \\ 1 & 0 \\ 0 & \frac{1}{m_0} \\ 0 & 0 \end{bmatrix} \tag{A.5}$$

Considering the output vector, the output gain matrix $[C]_{EDS}$ is

$$\begin{bmatrix} -\frac{2\Lambda_0}{\gamma m_0} e^{-\frac{z_{PM,0}}{\gamma}} & 0 & -\frac{2\Lambda_0}{\gamma m_0} e^{-\frac{z_{PM,0}}{\gamma}} & 0 & 0 & 0 & 0 \end{bmatrix} \tag{A.6}$$

and the direct link matrix $[D]_{EDS}$ results

$$\begin{bmatrix} 0 & \frac{1}{m_0} \end{bmatrix} \tag{A.7}$$

The previous matrices can also re-written considering a stiffness k_{us} as well as a damping term c_{us}. Under this assumption, the dynamic matrix $[A]_{EDS,kc}$ can be written as

$$\begin{bmatrix} -\omega_{1,p} & \omega & 0 & 0 & 0 & \frac{\Lambda_0}{\gamma L_1} e^{-\frac{z_{PM,0}}{\gamma}} & 0 \\ -\omega & -\omega_{1,p} & 0 & 0 & -\frac{\Lambda_0}{\gamma L_1} e^{-\frac{z_{PM,0}}{\gamma}} & 0 & \frac{\omega\Lambda_0}{\gamma L_1} e^{-\frac{z_{PM,0}}{\gamma}} \\ 0 & 0 & -\omega_{1,p} & \omega & 0 & \frac{\Lambda_0}{\gamma L_1} e^{-\frac{z_{PM,0}}{\gamma}} & 0 \\ 0 & 0 & -\omega & -\omega_{1,p} & -\frac{\Lambda_0}{\gamma L_1} e^{-\frac{z_{PM,0}}{\gamma}} & 0 & \frac{\omega\Lambda_0}{\gamma L_1} e^{-\frac{z_{PM,0}}{\gamma}} \\ 0 & 0 & 0 & 0 & 0 & 0 & 0 \\ -\frac{2\Lambda_0}{\gamma m_0} e^{-\frac{z_{PM,0}}{\gamma}} & 0 & -\frac{2\Lambda_0}{\gamma m_0} e^{-\frac{z_{PM,0}}{\gamma}} & 0 & -\frac{2\Lambda_0}{\gamma m_0} e^{-\frac{z_{PM,0}}{\gamma}} & -\frac{c_{us}}{m_0} & -\frac{k_{us}}{m_0} \\ 0 & 0 & 0 & 0 & 0 & 1 & 0 \end{bmatrix} \tag{A.8}$$

The input gain matrix $[B]_{EDS,kc}$ is thus

$$\begin{bmatrix} -\frac{\Lambda_0}{\gamma L_1} e^{-\frac{z_{PM,0}}{\gamma}} & 0 \\ 0 & 0 \\ -\frac{\Lambda_0}{\gamma L_2} e^{-\frac{z_{PM,0}}{\gamma}} & 0 \\ 0 & 0 \\ 1 & 0 \\ 0 & \frac{1}{m_0} \\ 0 & 0 \end{bmatrix} \tag{A.9}$$

Considering the output vector, the output gain matrix $[C]_{EDS,kc}$ is

$$\begin{bmatrix} -\frac{2\Lambda_0}{\gamma m_0}e^{-\frac{z_{PM,0}}{\gamma}} & 0 & -\frac{2\Lambda_0}{\gamma m_0}e^{-\frac{z_{PM,0}}{\gamma}} & 0 & -\frac{2\Lambda_0}{\gamma m_0}e^{-\frac{z_{PM,0}}{\gamma}} & -\frac{c_{us}}{m_0} & -\frac{k_{us}}{m_0} \end{bmatrix} \tag{A.10}$$

and the direct link matrix $[D]_{EDS,kc}$ results

$$\begin{bmatrix} 0 & \frac{1}{m_0} \end{bmatrix} \tag{A.11}$$

A.2 Voice coil actuator

The state variables are so arranged

$$\{Z\}_{vc} = \{v_{vc}, z_{vc}, i_{vc}\}^T \tag{A.12}$$

while the input of the system can be written

$$\{U\}_{vc} = \left\{f_{vc}, \frac{1}{R}\right\}^T \tag{A.13}$$

and the output as

$$\{Y\}_{vc} = \{\ddot{z}_{vc}\}^T \tag{A.14}$$

Under this assumption, the dynamic matrix $[A]_{vc}$ can be written as

$$\begin{bmatrix} -\frac{c_{vc}}{m_0} & 0 & \frac{K_m}{m_0} \\ 1 & 0 & 0 \\ -\frac{K_m}{L_{vc}} & 0 & -\frac{R_{vc}}{L_{vc}} \end{bmatrix} \tag{A.15}$$

The input gain matrix $[B]_{vc}$ is thus

$$\begin{bmatrix} \frac{1}{m_0} & 0 \\ 0 & \frac{1}{L_{vc}} \end{bmatrix} \tag{A.16}$$

Considering the output vector, the output gain matrix $[C]_{vc}$ is

$$\begin{bmatrix} \frac{-c_{vc}}{m_0} & 0 & \frac{K_m}{m_0} \end{bmatrix} \tag{A.17}$$

and the direct link matrix $[D]_{vc}$ results

$$\begin{bmatrix} \frac{1}{m_0} & 0 \end{bmatrix} \tag{A.18}$$

The previous matrices can also re-written considering a stiffness k_s. Under this assumption, the dynamic matrix $[A]_{vc,K}$ can be written as

$$\begin{bmatrix} -\frac{c_{vc}}{m_0} & -\frac{k_s}{m_0} & \frac{K_m}{m_0} \\ 1 & 0 & 0 \\ -\frac{K_m}{L_{vc}} & 0 & -\frac{R_{vc}}{L_{vc}} \end{bmatrix} \tag{A.19}$$

The input gain matrix $[B]_{vc,K}$ is thus

$$\begin{bmatrix} \frac{1}{m_0} & 0 \\ 0 & \frac{1}{L_{vc}} \end{bmatrix} \tag{A.20}$$

Considering the output vector, the output gain matrix $[C]_{vc,K}$ is

$$\begin{bmatrix} \frac{-c_{vc}}{m_0} & -\frac{k_s}{m_0} & \frac{K_m}{m_0} \end{bmatrix} \tag{A.21}$$

and the direct link matrix $[D]_{vc,K}$ results

$$\begin{bmatrix} \frac{1}{m_0} & 0 \end{bmatrix} \tag{A.22}$$

The previous matrices can also re-written considering only electric domain (null relative velocity). Under this assumption, the dynamic matrix $[A]_{vc,K}$ can be written as

$$\begin{bmatrix} \frac{R_{vc}}{L_{vc}} \end{bmatrix} \tag{A.23}$$

The input gain matrix $[B]_{vc,K}$ is thus

$$\begin{bmatrix} \frac{1}{L_{vc}} \end{bmatrix} \tag{A.24}$$

Considering as output vector the current state variable, the output gain matrix $[C]_{vc,K}$ is

$$\begin{bmatrix} 1 \end{bmatrix} \tag{A.25}$$

and the direct link matrix $[D]_{vc,K}$ results

$$\begin{bmatrix} 0 \end{bmatrix} \tag{A.26}$$

A.3 Dynamic measuring device

The state variables are so arranged

$$\{Z\}_{EM} = \{\dot{z}_{us}, z_{us}, \dot{z}_s, z_s, i_{vc}\}^T \tag{A.27}$$

while the input of the system can be written

$$\{U\}_{EM} = \{f_{us}, f_s, V\}^T \tag{A.28}$$

and the output as

$$\{Y\}_{EM} = \{\ddot{z}_{us}\ddot{z}_s\}^T \tag{A.29}$$

Under this assumption, the dynamic matrix $[A]_{EM}$ can be written as

$$\begin{bmatrix} -\frac{c_{vc}+c_{us}}{m_{us}} & -\frac{k_{us}+k_s}{m_{us}} & \frac{c_{vc}}{m_{us}} & \frac{k_s}{m_{us}} & -\frac{K_m}{m_{us}} \\ 1 & 0 & 0 & 0 & 0 \\ \frac{c_{vc}}{m_s} & \frac{k_s}{m_s} & -\frac{c_{vc}}{m_s} & -\frac{k_s}{m_s} & \frac{K_m}{m_{us}} \\ 0 & 0 & 1 & 0 & 0 \\ \frac{K_m}{L_{vc}} & 0 & -\frac{K_m}{L_{vc}} & 0 - \frac{R_{vc}}{L_{vc}} & \end{bmatrix} \tag{A.30}$$

The input gain matrix $[B]_{EM}$ is thus

$$\begin{bmatrix} \frac{1}{m_{us}} & 0 & 0 \\ 0 & 0 & 0 \\ 0 & \frac{1}{m_s} & 0 \\ 0 & 0 & 0 \\ 0 & 0 & \frac{1}{L_{vc}} \end{bmatrix} \tag{A.31}$$

Considering as output vector the current state variable, the output gain matrix $[C]_{EM}$ is

$$\begin{bmatrix} -\frac{c_{vc}+c_{us}}{m_{us}} & -\frac{k_{us}+k_s}{m_{us}} & \frac{c_{vc}}{m_{us}} & \frac{k_s}{m_{us}} & -\frac{K_m}{m_{us}} \\ \frac{c_{vc}}{m_s} & \frac{k_s}{m_s} & -\frac{c_{vc}}{m_s} & -\frac{k_s}{m_s} & \frac{K_m}{m_{us}} \end{bmatrix} \tag{A.32}$$

and the direct link matrix $[D]_{EM}$ results

$$\begin{bmatrix} \frac{1}{m_{us}} & 0 & 0 \\ 0 & \frac{1}{m_s} & 0 \end{bmatrix} \tag{A.33}$$

The previous matrices can also re-written in the configuration space. Defining a configuration vector written as

$$\{q\} = \{z_{us}, z_s\}^T \tag{A.34}$$

the mass matrix [M] can be written as

$$\begin{bmatrix} m_{us} & 0 \\ 0 & m_s \end{bmatrix} \tag{A.35}$$

the damping matrix $[C]$ is thus

$$\begin{bmatrix} c_{vc} + c_{us} & -c_{vc} \\ -c_{vc} & c_{vc} \end{bmatrix} \tag{A.36}$$

and the stiffness matrix [K] results

$$\begin{bmatrix} k_s + c_{us} & -k_s \\ -k_s & k_s \end{bmatrix} \tag{A.37}$$

The vector of the external forces include the current state

$$\{f\} = \{f_{us}, f_s\}^T + \{-K_m i, K_m i\}^T \tag{A.38}$$

A.4 Electrodynamicl levitated electromechanical system

The state variables are so arranged

$$\{Z\} = \{i_{1,d}, i_{1,q}, i_{2,d}, i_{2,q}, z_{in}, \dot{z}_{us}, z_{us}, \dot{z}_s, z_s, i_{vc}\}^T \tag{A.39}$$

while the input of the system can be written

$$\{U\} = \{\dot{z}_{in}, f_{us}, f_s, V\}^T \tag{A.40}$$

and the output as

$$\{Y\} = \{\ddot{z}_{us}\ddot{z}_s i_{vc}\}^T \tag{A.41}$$

Under this assumption, the dynamic matrix $[A]$ can be written as

$$\begin{bmatrix}
\text{-}\omega_{1,p} & \omega & 0 & 0 & 0 & \frac{\Lambda_0}{\gamma L_1} e^{-\frac{z_{PM,0}}{\gamma}} & 0 & 0 & 0 & 0 \\
-\omega & -\omega_{1,p} & 0 & 0 & -\frac{\Lambda_0}{\gamma L_1} e^{-\frac{z_{PM,0}}{\gamma}} & 0 & \frac{\omega\Lambda_0}{\gamma L_1} e^{-\frac{z_{PM,0}}{\gamma}} & 0 & 0 & 0 \\
0 & 0 & -\omega_{1,p} & \omega & 0 & \frac{\Lambda_0}{\gamma L_1} e^{-\frac{z_{PM,0}}{\gamma}} & 0 & 0 & 0 & 0 \\
0 & 0 & -\omega & -\omega_{1,p} & -\frac{\Lambda_0}{\gamma L_1} e^{-\frac{z_{PM,0}}{\gamma}} & 0 & \frac{\omega\Lambda_0}{\gamma L_1} e^{-\frac{z_{PM,0}}{\gamma}} & 0 & 0 & 0 \\
0 & 0 & 0 & 0 & 0 & 0 & 0 & 0 & 0 & 0 \\
-\frac{2\Lambda_0}{\gamma m_{us}} e^{-\frac{z_{us,0}}{\gamma}} & 0 & -\frac{2\Lambda_0}{\gamma m_{us}} e^{-\frac{z_{us,0}}{\gamma}} & 0 & 0 & -\frac{c_{vc}+c_{us}}{m_{us}} & -\frac{k_{us}+k_s}{m_{us}} & \frac{c_{vc}}{m_{us}} & \frac{k_s}{m_{us}} & -\frac{K_m}{m_{us}} \\
0 & 0 & 0 & 0 & 0 & 1 & 0 & 0 & 0 & 0 \\
0 & 0 & 0 & 0 & 0 & \frac{c_{vc}}{m_s} & \frac{k_s}{m_s} & -\frac{c_{vc}}{m_s} & -\frac{k_s}{m_s} & \frac{K_m}{m_{us}} \\
0 & 0 & 0 & 0 & 0 & 0 & 0 & 1 & 0 & 0 \\
0 & 0 & 0 & 0 & 0 & \frac{K_m}{L_{vc}} & 0 & -\frac{K_m}{L_{vc}} & 0 -\frac{R_{vc}}{L_{vc}} &
\end{bmatrix} \tag{A.42}$$

The input gain matrix $[B]$ is thus

$$\begin{bmatrix}
-\frac{\Lambda_0}{\gamma L_1} e^{-\frac{z_{PM,0}}{\gamma}} & 0 & 0 & 0 \\
0 & 0 & 0 & 0 \\
-\frac{\Lambda_0}{\gamma L_2} e^{-\frac{z_{PM,0}}{\gamma}} & 0 & 0 & 0 \\
0 & 0 & 0 & 0 \\
1 & 0 & 0 & 0 \\
0 & \frac{1}{m_{us}} & 0 & 0 \\
0 & 0 & 0 & 0 \\
0 & 0 & \frac{1}{m_s} & 0 \\
0 & 0 & 0 & 0 \\
0 & 0 & 0 & \frac{1}{L_{vc}}
\end{bmatrix} \tag{A.43}$$

Considering as output vector the current state variable, the output gain matrix

$[C]$ is

$$\begin{bmatrix} -\frac{2\Lambda_0}{\gamma m_{us}}e^{-\frac{z_{us,0}}{\gamma}} & 0 & -\frac{2\Lambda_0}{\gamma m_{us}}e^{-\frac{z_{us,0}}{\gamma}} & 0 & 0 & -\frac{c_{vc}+c_{us}}{m_{us}} & -\frac{k_{us}+k_s}{m_{us}} & \frac{c_{vc}}{m_{us}} & \frac{k_s}{m_{us}} & -\frac{K_m}{m_{us}} \\ 0 & 0 & 0 & 0 & 0 & \frac{c_{vc}}{m_s} & \frac{k_s}{m_s} & -\frac{c_{vc}}{m_s} & -\frac{k_s}{m_s} & \frac{K_m}{m_{us}} \\ 0 & 0 & 0 & 0 & 0 & 0 & 0 & 0 & 0 & 1 \end{bmatrix} \tag{A.44}$$

and the direct link matrix $[D]$ results

$$\begin{bmatrix} 0 & \frac{1}{m_{us}} & 0 & 0 \\ 0 & 0 & \frac{1}{m_s} & 0 \\ 0 & 0 & 0 & 0 \end{bmatrix} \tag{A.45}$$

Bibliography

[1] A. Tonoli, N. Amati, F. Impinna, and J. G. Detoni. «A Solution for the Stabilization of Electrodynamic Bearings: Modeling and Experimental Validation». In: *Journal of vibration and acoustics* 133 (Mar. 2011) (cit. on p. 2).

[2] L. Marelli, A. Tsakalidis, K. Gkoumas, A. Haq, M. Grosso, and F. Pekar. «Strategic Transport Research and Innovation Agenda (STRIA) Roadmap Factsheets». In: (2017). URL: `https://ec.europa.eu/jrc/en/publication/strategic-transportresearch-%20and-innovation-agenda-stria-roadmap-factsheets` (cit. on p. 2).

[3] F.C. Moon. «Superconducting Levitation». In: *New York: Wiley* (1994) (cit. on p. 2).

[4] D.M. Rote and Y. Cai. «Review of dynamic stability of repulsive-force maglev suspension systems». In: *Magnetics, IEEE Transactions on* 38 (Apr. 2002), pp. 1383–1390. DOI: `10.1109/20.996030` (cit. on pp. 2, 8).

[5] H. Yoshioka, E. Suzuki, H. Seino, M. Azakami, H. Oshima, and T. Nakanishi. «Results of running tests and characteristics of the MLX01 Yamanashi test vehicles». In: *in Proc. Maglev'98 Conf. Yamanashi, Japan* 38 (Apr. 1998), pp. 225–230 (cit. on p. 3).

[6] H. Fink and C. Hobrecht. «Instability of Vehicles Levitated by Eddy Current Repulsion-Case of an Infinitely Long Current Loop». In: *Journal of Applied Physics* 42 (Sept. 1971), pp. 3446–3450. DOI: `10.1063/1.1660751` (cit. on p. 3).

[7] T. Yamada, M. Iwamoto, and T. Ito. «Magnetic damping force in inductive magnetic levitation system for high-speed trains». In: *Electrical Engineering in Japan* 94 (Jan. 1974), pp. 80–84. DOI: `10.1002/eej.4390940112` (cit. on p. 3).

[8] S.S. Chen, S Zhu, Y. Cai, and D.M. Rote. «Magnetic Damping For Maglev». In: vol. 5. Dec. 1994. DOI: `10.1155/1998/480273` (cit. on p. 3).

[9] S. Fujiwara. «Damping characteristics of the repulsive magnetic levitation vehicle». In: 21 (Mar. 1980), pp. 49–52 (cit. on p. 3).

[10] F.C. Moon. «Laboratory studies of magnetic levitation in the thin track limit». In: *Magnetics, IEEE Transactions on* 10 (Oct. 1974), pp. 439–442. DOI: 10.1109/TMAG.1974.1058454 (cit. on p. 3).

[11] R.F. Post and D. Ryutov. «The Inductrack concept: A new approach to magnetic levitation». In: (May 1996). DOI: 10.2172/237425 (cit. on p. 3).

[12] R. Post and D. Ryutov. «The Inductrack: A simpler approach to magnetic levitation». In: *Applied Superconductivity, IEEE Transactions on* 10 (Apr. 2000), pp. 901–904. DOI: 10.1109/77.828377 (cit. on pp. 3, 12).

[13] S. Gurol and B. Baldi. «Overview of the General Atomics Urban Maglev Technology Development Program». In: May 2004, pp. 187–191. ISBN: 0-7918-4163-4. DOI: 10.1109/RRCON.2004.1300918 (cit. on p. 3).

[14] O.F. Storset and Bradley Paden. «Infinite dimensional models for perforated track electrodynamic magnetic levitation». In: vol. 1. Jan. 2003, 842–847 vol.1. DOI: 10.1109/CDC.2002.1184610 (cit. on pp. 4, 22).

[15] SpaceX. «Hyperloop Alpha». In: (2013). URL: https://www.spacex.com/sites/spacex/files/%20hyperloop_alpha-20130812.pdf (cit. on pp. 4, 12).

[16] R. Pradhan and A. Katyayan. «Vehicle Dynamics of Permanent-Magnet Levitation Based Hyperloop Capsules». In: Sept. 2018, V002T22A004. DOI: 10.1115/DSCC2018-9130 (cit. on p. 4).

[17] R. Galluzzi, S. Circosta, N. Amati, A. Tonoli, A. Bonfitto, T. Lembke, and M. Kertész. «A Multi-Domain Approach to the Stabilization of Electrodynamic Levitation Systems». In: *Journal of Vibration and Acoustics* 142 (Apr. 2020), pp. 1–30. DOI: 10.1115/1.4046952 (cit. on pp. 4, 5, 13, 23, 24, 101, 124).

[18] Federica Fanigliulo. «Design and control of an experimental test system for a linear electrodynamic levitation device». In: *Politecnico di Torino* Master's thesis (2021) (cit. on pp. 5, 8, 15, 59, 65).

[19] Andrea Bo. «Modeling, control and characterization of an electrodynamic levitation test bench». In: *Politecnico di Torino* Master's thesis (July 2022) (cit. on pp. 5, 14, 15, 17, 37, 43, 46, 59, 65).

[20] Arianna Conchin Gubernati. «Experimental test bench for electrodynamic levitation system characterization». In: *Politecnico di Torino* Master's thesis (July 2022) (cit. on pp. 5, 17, 37, 43, 46, 59, 65).

[21] Marius Pakštys. «A Study and Implementation of Stability in Electrodynamic Levitation Systems». In: *Politecnico di Torino* Master's thesis (Oct. 2022) (cit. on pp. 6, 27, 64).

[22] Eric Chaidez, Shankar Bhattacharyya, and Adonios Karpetis. «Levitation Methods for Use in the Hyperloop High-Speed Transportation System». In: *Energies* 12 (Nov. 2019). DOI: 10.3390/en12214190 (cit. on p. 9).

[23] R. M. Salter. «The Very High Speed Transit Systems». In: *Rand Corporation* (Aug. 1972), p. 4874 (cit. on p. 9).

[24] Hyung-Woo Lee, ki-chan Kim, and ju Lee. «Review of Maglev train technologies». In: *Magnetics, IEEE Transactions on* 42 (Aug. 2006), pp. 1917–1925. DOI: 10.1109/TMAG.2006.875842 (cit. on p. 10).

[25] N. Bilton. «Questioning the Feasibility of Hyperloop». In: *New York Times* (Aug. 2013) (cit. on p. 12).

[26] Synchronous Servomotors ALM. «Edition 03». In: (2004). URL: https://www.kollmorgen.com/it-it/products/motors/servo/akm-series/akm-series-ac-synchronous-motors/servomotori-sincroni-akm/ (cit. on p. 15).

[27] AKD quick start. «Revition F,» in: (Dec. 2015). URL: https://www.kollmorgen.com/sites/default/files/public_downloads/AKD%5C%20Quick%5C%20Start%5C%20EN%5C%20%5C%28REV%5C%20E%5C%29.pdf (cit. on p. 15).

[28] Geeplus electromechanical actuators catalogue 2019. «datasheet». In: vm108 - 2p30 (). URL: https://www.geeplus.com/wp-content/uploads/2019/08/Voice_Coil_motor_VM108-2P30.pdf (cit. on pp. 18, 32, 33, 65).

[29] G. Genta. *Vibration Dynamics and Control*. Mechanical Engineering Series. Springer US. ISBN: 9780387795799 (cit. on pp. 47, 48, 87).

[30] R. Kalman. «A New Approach To Linear Filtering and Prediction Problems». In: *Journal of Basic Engineering (ASME)* 82D (Mar. 1960), pp. 35–45. DOI: 10.1115/1.3662552 (cit. on p. 51).

[31] A. Fasana and S. Marchesiello. *Meccanica delle Vibrazioni*. CLUT - Torino, 2006 (cit. on pp. 71, 72, 78, 79, 84).